

**The close environment of AFGL 490 in
radio-interferometric observations**

**(Die nahe Umgebung von AFGL 490 in
radiointerferometrischen Beobachtungen)**

Dissertation
zur Erlangung des akademischen Grades
doctor rerum naturalium (Dr. rer. nat.)

**vorgelegt dem Rat der Physikalisch-Astronomischen Fakultät
der Friedrich-Schiller-Universität Jena**

von Dipl.-Phys. Claudia Marka
geboren am 17.10.1984 in Karl-Marx-Stadt

Gutachter:

1. PD Dr. Katharina Schreyer (Jena)
2. Prof. Dr. Peter Schilke (Köln)
3. Prof. Dr. Peter Hofner (Socorro)

Tag der Disputation: 29.1.2015

Contents

1	Introduction	7
1.1	Motivation – star formation and discs	7
1.2	Previous studies of AFGL 490	9
2	Overview of the observational data	13
2.1	Individual data sets	13
2.1.1	Plateau de Bure Interferometer (PdBI)	13
2.1.2	Very Large Array (VLA)	14
2.1.3	Very Large Array Archive Data	14
2.2	Summary	15
3	Emission of the innermost region – the disc	17
3.1	Observations	17
3.1.1	Continuum emission	17
3.1.2	Spectral line emission	20
3.2	Description of the radiative transfer modelling programs	34
3.2.1	Protoplanetary disc model - general approach	34
3.2.2	Opacities	36
3.2.3	Refined model with puffed-up inner rim and disc shadowing	38
3.2.4	Synthetic spectra - radiative transfer with URANIA	45
3.2.5	Discs with inner holes	47
3.3	Parameter space for the modelling runs	49
3.4	Results of the disc modelling	51
3.4.1	$C^{17}O(2-1)$	51
3.4.2	Modifications of the disc modelling	57
3.4.3	$C^{34}S(2-1)$	61
3.4.4	$CS(1-0)$	64
3.4.5	$CH_3OH(2_0-1_0 E)$, $(2_0-1_0 A^+)$ and $(2_{-1}-1_{-1} E)$	66
3.5	Summary and discussion	69
4	Emission of the wider environment – the outflow	73
4.1	Observations and analysis	73
4.1.1	$CH_3OH(2_0-1_0 E)$, $(2_0-1_0 A^+)$, and $(2_{-1}-1_{-1} E)$	73
4.1.2	$C^{34}S(2-1)$	75
4.1.3	VLA $CS(1-0)$	79
4.2	Modelling of the outflow emission	87

4.3 Summary and discussion	93
5 Summary and outlook	95
References	101
A Appendix	107
A.1 Radial structure of the model disks	107
A.2 Fits of the lines in outflow clumps spectra	108
A.3 Results of the radiative transfer modelling	114

List of Figures

3.1	Continuum emission of AFGL 490	18
3.2	Contour maps and spectra of the central red- and blueshifted emission in $C^{17}O$ and $C^{34}S$	21
3.3	Contour maps and spectra of the central red- and blueshifted emission in $CH_3OH(2_0-1_0 A^+)$ and $(2_{-1}-1_{-1} E)$	22
3.4	Contour maps and spectra of the central red- and blueshifted emission in $CH_3OH(2_1-1_1 E)$	23
3.5	Contour maps and spectra of the central red- and blueshifted emission in CS	24
3.6	Integrated intensity contour plots for $C^{17}O$, $C^{34}S$, CH_3OH and CS	27
3.7	Position-velocity diagrams (a)	29
3.8	Position-velocity diagrams (b)	30
3.9	Position-velocity diagrams with best-fit velocity profiles	32
3.10	Sketch of the disc model	38
3.11	Vertical temperature structure of a disc model in comparison with literature	42
3.12	Disc height and temperature profiles for a disc model in comparison with the literature	44
3.13	χ_w^2 maps for $C^{17}O$ and different surface density profiles	53
3.14	Spectra map of $C^{17}O$ in comparison with synthetic spectra from a disc model	54
3.15	χ_w^2 maps for $C^{17}O$ and disc models with different outer radii	55
3.16	χ_w^2 for $C^{17}O$ and disc models with different velocity profiles	60
3.17	Comparison of $C^{17}O$ spectra and disc models with different velocity profiles	60
3.18	χ_w^2 maps for $C^{34}S$ and disc models with different surface density profiles . .	61
3.19	Comparison of $C^{34}S$ spectra and synthetic spectra from disc model	62
3.20	χ_w^2 for $C^{17}O$ and $C^{34}S$ for disc models with different outer disc radii and surface density profiles	63
3.21	χ_w^2 for CS and disc models with different surface density profiles	65
3.22	Comparison of CS spectra and synthetic spectra from disc model	65
3.23	χ_w^2 for CS and disc models with different outer radii	66
4.1	Contour map of integrated CH_3OH emission and spectra in the wide environment of AFGL 490	74
4.2	Contour map of integrated $C^{34}S$ emission and spectra in the wide environment of AFGL 490	76
4.3	Integrated intensity maps of $C^{34}S$ around two positions in the outflow region	77
4.4	Spectra maps of $C^{34}S$ around two positions in the outflow region	78

4.5	Contour maps of integrated CS emission and spectra in the wide environment of AFGL 490	80
4.6	Channel maps of CS in the wide environment of AFGL 490	81
4.7	Contour maps of $C^{34}S$, CH_3OH and CS with fitted parabolic curves	82
4.8	Outflow region of AFGL 490 at different wavelengths	84
4.9	Sketch of the outflow model	87
4.10	Comparison of observed emission with integrated intensity plots of outflow models with different inclinations	89
4.11	Comparison of observed spectra and model spectra for two inclinations at selected positions in the outflow	90
4.12	Peculiar line profiles in CH_3OH and CS in the central emission region of AFGL 490	92
4.13	Peculiar line profiles in CH_3OH in the outflow region of AFGL 490	92
4.14	Peculiar line profiles in CS in the outflow region of AFGL 490	92
A.1	Radial structure of the model discs	107
A.2	Line fits of CH_3OH in the outflow region	109
A.3	Line fits of $C^{34}S$ in the outflow region	110
A.4	Line fits of CS(1-0) in the outflow region	111

List of Tables

2.1	Overview of the observational data set	13
2.2	Characteristics of the observed transitions	15
3.1	Properties of the continuum sources	17
3.2	Geometry parameters of the red- and blueshifted emission around AFGL 490	23
3.3	Parameters of a two-Gaussian approximation to the integrated spectra . . .	27
3.4	Parameters of velocity profile fits to the position-velocity diagrams	31
3.5	Input parameters for the disc model	51
3.6	Parameters of the disc models	52
4.1	Properties of emission clumps in C ³⁴ S, CS and CH ₃ OH in the wide environ- ment of AFGL 490	85

Symbols and constants

Symbol	Unit	Explanation
κ	cm^2/g	Opacity
Σ	g/cm^2	Surface density
ρ	g/cm^3	Density
n	cm^{-3}	Number density
τ		Optical depth
T	K	Temperature
A_{ul}	s^{-1}	Spontaneous emission coefficient

Constant	Value	Explanation
c	$2.9979 \times 10^8 \text{ m/s}$	Speed of light
σ	$5.67 \times 10^{-8} \text{ W/m}^2/\text{K}^4$	Stefan-Boltzmann constant
k	$1.38 \times 10^{-23} \text{ J/K}$	Boltzmann constant
G	$6.672 \times 10^{-11} \text{ m}^3/\text{kg}/\text{s}^2$	Gravitational constant
h	$6.626 \times 10^{-34} \text{ Js}$	Planck constant
m_{H}	$1.66 \times 10^{-26} \text{ kg}$	Proton mass
μ	2.3	Mean molecular weight
M_{\odot}	$2 \times 10^{30} \text{ kg}$	Solar mass
L_{\odot}	$3.84 \times 10^{26} \text{ W}$	Solar luminosity
R_{\odot}	$7 \times 10^8 \text{ m}$	Solar radius
au	$1.496 \times 10^{11} \text{ m}$	Astronomical unit
pc	$3.0857 \times 10^{16} \text{ m}$	Parsec
J_{ν}	$1 \times 10^{-26} \text{ W/m}^2/\text{Hz}$	Flux density

1 Introduction

1.1. Motivation – star formation and discs

As the predominant sources of visible light in the universe, stars have served as a source of inspiration and curiosity throughout the history of culture and science. Stars are the building blocks of the visible universe and the most efficient processors and redistributors of material. Despite one common characteristic of all stars – fusion of hydrogen over some part of their life cycle – they exhibit a large diversity in their physical properties and stages of evolution. The foundations of these differences, in particular the mass of the star, are laid during the star formation process. Moreover, this is the environment in which planet formation, and therefore the basis of life as we know it, takes place.

The observational investigation of the earliest phases of star formation, where the young stellar objects are still embedded in their parental clouds and dim in the visual range, required an extension of observational techniques beyond the optical toward longer wavelengths.

Since the availability of infrared, sub-millimetre and millimetre telescopes both on ground and in space (e.g. IRAS, IRAM, SEST commissioned during the 1980s), the knowledge about the formation of stars has grown substantially and continues to grow with each generation of more sensitive observing facilities (e.g. recently Herschel, ALMA). While the formation of low-mass stars ($\leq 2 M_{\odot}$) from collapsing molecular cloud cores, over protostars surrounded by infalling envelopes and accreting material via a circumstellar disc, to main-sequence stars with active hydrogen fusion is thought to be well understood, many questions remain regarding the formation of intermediate (ca. $2\text{--}8 M_{\odot}$) and massive ($\geq 8\text{--}10 M_{\odot}$) stars (see e.g. reviews of Zinnecker & Yorke 2007; McKee & Ostriker 2007; Stahler & Palla 2005). A long-lasting debate regarding the formation of especially very massive stars was, how they could keep accreting material despite the presence of exceedingly large radiation pressure exerted by the young stellar object. Meanwhile there is agreement that the anisotropy of the radiation field (e.g. Krumholz 2006), where radiation escapes predominantly along the low-density areas of outflow lobes and is blocked in the plane of a circumstellar disc, overcomes this problem and accretion could proceed along the plane of the disc. However, as a main point of discussion remains, whether the formation of massive stars indeed takes place via accretion through scaled-up versions of the circumstellar discs found around young low-mass stars. For Herbig Ae/Be stars as the precursors of intermediate-mass stars, observational evidence for discs exists, where discs around Herbig Ae stars were found to be explainable by a standard flared disc model as for their low-mass counterparts, but there are few hints on discs around the more massive Herbig Be stars (Testi 2004). Observational evidence for discs around even more massive

B and O type stars is scarce (e.g. Zhang et al. 1998, Beuther et al. 2004, Cesaroni et al. 2005, Wang et al. 2012, or review by Cesaroni et al. 2007) and consequently also the knowledge about the structure of such discs – where non-axisymmetry due to effects of self-gravitation in massive discs (e.g. Rice & Armitage 2009) is only one aspect of the possible structural differences to low-mass discs. Besides the location of massive stars, and hence disc candidates around them, often deeply embedded in the complex environment of clusters, the observation of massive discs may be further hampered by the short lifetime expected for them ($<10^6$ yr Kennedy & Kenyon 2009; Zinnecker & Yorke 2007) – disc dispersal mechanisms like photoevaporation through the central or nearby stars' UV radiation or removal of outer disc material by close encounters with cluster members are expected to efficiently disperse especially the outer disc regions, in contrast to low-mass stars where the inside-out dispersal by viscous accretion dominates (C. M. Koepferl et al. 2012; Hollenbach et al. 2000) and discs exist for a couple of million years.

However, especially these very early phases of massive star formation are particularly challenging for observation: massive stars are (i) rare, therefore on average located at large distance from earth, resulting in poor spatial resolution of observations, (ii) have a short lifetime, i.e. quick evolution, and hence only few objects are observable in the pre-main sequence phase at a time, (iii) typically reach the main sequence while still accreting material, i.e. are deeply embedded in their parental cloud for practically the whole course of their pre-main-sequence evolution, and (iv) are often members of stellar clusters, posing the problem of confusion and complex environment.

To study massive stars in the process of formation and details of their immediate environment, radio interferometry at millimetre wavelengths is the method of choice: it provides sub-arcsecond spatial resolution and enables the investigation of regions with a wide range of different physical properties (density, temperature, chemical composition, velocity structure) by observation of selected molecular transitions or continuum wavelengths, including regions embedded within gas and dust which are hidden from the view at shorter wavelengths.

The work presented here focuses on AFGL 490, one of the very few examples of a young, deeply embedded, potentially massive star at moderate distance, around which previous interferometric observations revealed signatures of a massive rotating gas disc. Interferometric observations of additional molecular transitions are analysed with the aim to verify the signs of a massive circumstellar disc, yield tighter constraints on the physical and chemical disc properties from the multi-molecule observations, and to study in general the close environment of AFGL 490 at high spatial resolution regarding e.g. signs of ongoing accretion and possible jets.

In the following section, a short summary of the state of knowledge about AFGL 490 from

previous studies is given, before the observational data sets and their analysis is presented in the following chapters.

1.2. Previous studies of AFGL 490

AFGL 490 (also referred to as IRAS 03236+5836, G 142.00+1.83, AFCRL/GL/CRL 490, UOA 1 in the literature) was discovered as a bright mid-infrared (MIR) source in the AFCRL sky survey (Walker & Price 1975) and identified as a faint ($V \approx 21^m$) red star in the optical (Cohen 1975; Cohen & Kuhi 1977). Subsequently, AFGL 490 was target of numerous studies spanning the spectral range from optical to radio wavelengths.

Available photometry covers optical (Campbell et al. 1986), near-infrared (NIR; Jones et al. 1990), mid-infrared (MIR; Low et al. 1976; Joyce et al. 1977), far-infrared (FIR; Harvey et al. 1979; Schreyer et al. 2002), (sub-)millimetre (Chini et al. 1991; Sandell 1994; Schreyer et al. 2002, 2006), and centimetre (Simon et al. 1983; Campbell et al. 1986) wavelengths and composes the steep spectral energy distribution (SED) of a deeply embedded ($A_V = 10\text{--}25^m$; Harvey et al. 1979; Simon et al. 1983; McGregor et al. 1984) young stellar object (YSO), whose luminosity ($L_{\text{bol}} = 1.4\text{--}2.6 \times 10^3 L_{\odot}$; e.g., Harvey et al. 1979; Henning et al. 1990) corresponds to a zero-age main sequence (ZAMS) star of spectral typ B2–B3 (Panagia 1973).

Indications for variability stem from infrared photometry (Jones et al. 1990) and changing appearance on infrared and radio maps (Hoare et al. 1996; Alvarez et al. 2004).

Spectra at visual and infrared wavelengths are dominated by strong emission lines of the Balmer-, Paschen-, Brackett- and Pfund series of hydrogen, which partially display broad linewings (Cohen & Kuhi 1977; Simon et al. 1979, 1983; Campbell et al. 1986; Gibb et al. 2004); weaker lines of Ca II, O II and Fe II (McGregor et al. 1984); absorption bands from silicate and ice around 3 and 10 μm , where the main ice constituents are H₂O, CO₂ and CO (Merrill & Stein 1976; Holloway et al. 2002; Gibb et al. 2004); absorption lines assigned to H₃⁺ (McCall et al. 1999); infrared CO absorption lines indicating the presence of a cooler (ca. 20 K) and a warmer (ca. 100 K) gas component (Mitchell et al. 1995) and showing P Cygni profiles assigned to outflowing gas (Mitchell et al. 1991).

A multitude of species and isotopes has been detected in centimetre and millimetre line observations, pointing to a relatively cool molecular envelope: HCN, CS (Morris et al. 1974); CO, ¹³CO (Lada & Harvey 1981); NH₃ (Takano 1986); HCO⁺ (Kawabe et al. 1987); C₃H₂ (Madden et al. 1989); CH (Magnani et al. 1992); H¹³CO⁺ (Hasegawa & Mitchell 1995); C³⁴S (Zinchenko et al. 1998); N₂H⁺ (Williams & Myers 1999); C¹⁷O, H₂CO (van der Tak et al. 2000b); CH₃OH (van der Tak et al. 2000a); C¹⁸O, NO, SO, SO₂, SiO, HC₃N, C₂H, HC¹⁵N, H¹³CN, DCN, possibly D₂CO (Schreyer et al. 2002).

AFGL 490 hosts an H₂O maser (Rodriguez & Canto 1983; Henkel et al. 1986) which exhibits variability on time scales of one year (Rodriguez & Canto 1983, and references

therein), but no SiO, CH₃OH, or OH masers have been detected towards the source (Zapata et al. 2009; Haschick et al. 1990; Szymczak et al. 2000). Distance estimates for the source vary between 900 pc and 1.2 kpc (Harvey et al. 1979; Straizys & Laugalys 2007; Snell et al. 1984; Wouterloot et al. 1993, mainly kinematic distances).

On large scales, molecular lines maps reveal the presence of a CO outflow with dynamical timescale of about 10⁴ yr (Lada & Harvey 1981; Snell et al. 1984; Mitchell et al. 1995), which was also detected in HCO⁺ (Kawabe et al. 1987) and as high-velocity wings in CS and SO (Kawabe et al. 1984; Schreyer et al. 2002). Shell-like structures outlining the cavity walls of the outflow were seen in HCO⁺ and HCN (Kawabe et al. 1987). A structure with size of few 10 000 au, elongated perpendicular to the outflow direction, was detected in single-dish and interferometric maps of CS and C¹³O (Kawabe et al. 1984; Mundy & Adelman 1988; Nakamura et al. 1991). Inside this flattened inner envelope and elongated in the same direction, interferometric CS and C¹⁷O observations show a dense gas disc or torus with radius of about 1 600 au; the C¹⁷O emission could be modelled with a flared disc in Keplerian rotation around a 8–10 M_⊙ star (Schreyer et al. 2002, 2006). Indications for an even smaller (≤500 au) structure, possibly the real accretion disc, arise from a compact millimetre continuum source (Schreyer et al. 2002), and indirectly from a high hydrogen B_γ flux possibly pointing to ionizing excess UV flux (Thompson & Tokunaga 1979) and polarization across the Pa_β line (Oudmaijer et al. 2005).

In general, less resolved millimetre and submillimetre continuum emission was found to be compact, originating from a few 1 000 au large structure (Mundy & Adelman 1988; Chini et al. 1991; Zapata et al. 2009).

Interferometric observations of the centimetre continuum emission show a core and weak extended emission, elongated neither perpendicular nor parallel to the outflow axis, at 2 and 6 cm (Campbell et al. 1986), while an unresolved source was detected at 1.3 cm (Simon et al. 1983). The spectral index in this wavelength range was explained with an ionized, small, dense core from which hydrogen recombination lines and the majority of the ≤2 cm free-free radio continuum originate, while most of the 6 cm emission is produced in a partially ionized tenuous halo (Alonso-Costa & Kwan 1989). Ionized flows of material from the star or off from the disc were also discussed as causes of centimetre continuum emission (Simon et al. 1983; Campbell et al. 1986).

NIR images show an unresolved core surrounded by a halo, whose amount and pattern of polarization agrees with a model in which light from the central source is scattered off the walls of an outflow cavity (Hodapp 1984; Haas et al. 1992; Leinert et al. 2001). An elongated area of low polarization perpendicular to the outflow axis, outlining the disc or toroid, is observed in NIR (Minchin et al. 1991). Optical, NIR, and H₂ narrow band images show diffuse nebulosities around AFGL 490 associated with the outflow cavities, mainly tracing the blue-shifted southwestern lobe (Campbell et al. 1986; Hodapp 1990; Davis et al. 1998).

Dark areas in the optical range correspond to CS emission peaks (Campbell et al. 1986). Even speckle interferometry does not resolve the core at NIR wavelengths (Howell et al. 1981; Haas et al. 1992; Alvarez et al. 2004). Sparse aperture interferometry constrains the size in MIR to 0.1'' (Monnier et al. 2009).

From additional outflow systems (Purton et al. 1995; Schreyer et al. 2002), jets (Davis et al. 1998), and possible YSOs identified on optical and NIR images (Campbell et al. 1986; Hodapp 1990; Straizys & Laugalys 2008; Gutermuth et al. 2009) it seems that AFGL 490 is surrounded by a considerable number of low-mass objects. Although common for early-type stars, there are no indications for multiplicity of AFGL 490 itself on scales down to 0.1'' (e.g., Haas et al. 1992; Leinert et al. 1997).

2 Overview of the observational data

A short summary of the observational data sets representing the primary basis for this work and the process of data reduction used is given in the following chapter. Technical and observational parameters of the data sets are collected in Tab. 2.1, an overview of physical parameters of the observed transitions is given in Tab. 2.2. In the following, usually only the according molecule name will be used to refer to a certain observed transition.

Table 2.1: Overview of the observational data sets: molecule, transition, rest frequency of transition, telescope and its array configuration, synthesized beamsize (major and minor axes) and position angle of the beam, noise of the dataset, and the resolution in velocity. A multiplicative factor in front of the velocity resolution indicates the smoothing factor applied to the original, unbinned channel width. The values refer to naturally weighted image cubes, if not stated otherwise.

Transition	ν [GHz]	Telescope (Config.)	$\theta_1 \times \theta_2$ ["]	PA [°]	σ . [mJy/beam]	$\Delta\nu$ [km/s]
$C^{17}O(2-1)^1$	224.714	PdBI (B)	0.88×0.78	72.7	26.9	2×0.052
$C^{34}S(2_0-1_0)$	96.4129	PdBI (BC)	2.15×1.95	68.9	16.4	0.121
CH ₃ OH(2 ₋₁₋₁ -1 ₋₁ E)	96.7394					
CH ₃ OH(2 ₀₋₁ ₀ A ⁺)	96.7414	PdBI (BC)	2.15×1.94	62.9	9.5	2×0.121
CH ₃ OH(2 ₀₋₁ ₀ E)	96.7445					
CH ₃ OH(2 ₁₋₁ ₁ E)	96.7555	PdBI (BC)	2.15×1.94	62.0	9.8	0.121
CS(1-0)	48.991	VLA (C)	0.71×0.59	-4.7	10.6	0.298
CS(1-0)	48.991	VLA (D)	1.68×1.60	117.6	7.8	0.597
Continuum ² (3.6 cm)	8.4601	VLA (B)	0.89×0.71	164	0.012	1770 ⁴
Continuum ³ (3.6 cm)	8.4601	VLA (A)	0.26×0.19	140	0.009	1770 ⁴

(1) Observations published already by Schreyer et al. (2006), re-reduced measurements are included here for comparison.

(2) Project AH0597 publicly available archive data.

(3) Project AH5970 publicly available archive data.

(4) Corresponding to a bandwidth of 50 MHz.

2.1. Individual data sets

2.1.1 Plateau de Bure Interferometer (PdBI)

The observations of C³⁴S, CH₃OH (PdBI C and B array) and C¹⁷O (PdBI B) were taken in projects N01E (C array) and N034 (B array) in November and December 2003. All line data sets were available already calibrated in phase, amplitude, flux and bandpass (Schreyer, priv. comm.) at the beginning of this work. A re-reduction of the observations was attempted, but

did not improve the quality of the data sets, therefore the originally calibrated data were used for analysis. The imaging process and analysis was carried out using the GILDAS¹ software package in a similar fashion for all transitions. For each line data set, a continuum uv data set was constructed by averaging the velocity channels free of line emission, which were determined from a first imaging process from the uv visibilities without continuum subtraction. This continuum was subtracted from the original uv data to produce a data set containing only the line emission. The uv visibilities were then Fourier transformed to "dirty" maps with a pixel size $\leq \frac{1}{4}$ of the beam size of the according data set (typically one cube with 0.1" and one with 0.4–0.5"), and subsequently create a "clean" image with a Hogbom algorithm. The primary beam size of the PdBI and, hence, the field of view, equals 52.2" at 96 GHz and 22.4" at 224 GHz. Different mapping (natural and robust weighting) and cleaning parameters (number of cleaning components, stopping criterion) were explored, but the resulting images did not differ significantly in the emission pattern for different weighting parameters. Therefore, the discussions and analysis in the following chapters refer to naturally weighted (giving the lowest noise σ) image cubes, if not stated otherwise.

2.1.2 Very Large Array (VLA)

Observations of the CS(1–0) transition at 48.99 GHz were obtained by the VLA C-array in project AS793 in April and May 2004, and in the more compact D configuration in December 2005 under project AS850. The data reduction was carried out by E. D. Araya (Schreyer, priv. comm.). For the VLA-C data set, an image cube with $1024 \times 0.042''$ and robust weighting (with parameter 5), corresponding to a synthesized beam size of $\sim 0.65''$, is available. However, both in the image plane as in the spectral channels residual structure in the form of ripples remain, possibly from phase instabilities during the observations. The data set is therefore mostly not used in the following discussion.

From the calibrated uv data of the VLA-D observations, image cubes with pixel size 0.1" were obtained for both the unchanged uv data, and a uv data set from which the continuum – estimated from the outer half of the spectral channels – was subtracted. Since no significant difference in the emission pattern is found for the different weighting schemes, the following discussion refer to an image cube with natural weighting, yielding a beam size of $\sim 1.6''$ and noise of 8 mJy/beam. The primary beam size of the VLA is about 55" at the corresponding frequency.

2.1.3 Very Large Array Archive Data

In addition to the spectral line data, the VLA archive was searched for continuum observations of AFGL 490 of high spatial resolution, in order to possibly obtain more constraints on the structure of the innermost dust emission or hints on a possible multiplicity of the

¹ *Grenoble Image and Line Analysis Software*, see <http://www.iram.fr/IRAMFR/GILDAS> .

central source. Publicly available high-resolution, high-sensitivity continuum observations of AFGL 490 were found for the X-band (3.6 cm) in VLA-B (project AH0597) and A configuration (project AH5970, both 1997). For both data sets, standard calibration (amplitude, phase, flux calibration) was performed with the AIPS² software package, using 0134+329 as flux and 0302+625 as phase calibrator. Clean images were produced from the calibrated uv data sets using robust weighting (for a smaller synthesized beam size compared to natural weighting) and pixel sizes of 0.2'' (AH0597, clean beam size $\sim 0.8''$) and 0.04'' (AH5970, clean beam size $\sim 0.2''$), resulting in an rms of 0.012 mJy/beam and 0.009 mJy/beam, respectively.

Table 2.2: Some characteristics of the observed transitions: frequency, spontaneous emission coefficient, energy of the upper level of the transition expressed as the equivalent temperature, critical density (above which collisions become an efficient excitation mechanism), and fractional molecular abundance (relative to H₂) assumed in the later chapters.

Transition	ν [GHz]	A_{ul} ¹ [s ⁻¹]	E_u ¹ [K]	ρ_{crit} ² [cm ⁻³]	X_{mol}
C ¹⁷ O(2-1)	224.714	6.4×10^{-7}	16	6×10^3	4×10^{-8}
C ³⁴ S(2 ₀ -1 ₀)	96.4129	1.6×10^{-5}	7	2×10^5	5×10^{-10}
CH ₃ OH(2 ₋₁ -1 ₋₁ E)	96.7394	2.6×10^{-6}	12	3×10^4	
CH ₃ OH(2 ₀ -1 ₀ A ⁺)	96.7414	3.4×10^{-6}	7	3×10^4	
CH ₃ OH(2 ₀ -1 ₀ E)	96.7445	3.4×10^{-6}	20	3×10^4	
CH ₃ OH(2 ₁ -1 ₁ E)	96.7555	2.6×10^{-6}	28	3×10^4	
CS(1-0)	48.991	1.7×10^{-6}	2	2×10^4	1×10^{-8}

(¹) Spectroscopic data adopted from Leiden Atomic and Molecular Database (Schöier et al. 2005).

(²) With critical density $\rho_{crit} = A_{ul}/(\sigma_{cs} \bar{v})$, where the collisional cross section is estimated as 10^{-15} cm² and the average velocity is taken that of H₂ molecules at 100 K, $\bar{v} = 10^2$ m/s.

2.2. Summary

Continuum emission at the position of AFGL 490 is detected in all data sets considered in this work. For the lines of C³⁴S, CS and CH₃OH, the emission features detected in the environment of AFGL 490 can be roughly divided into two regions: an inner region within 2'' (i.e. about 2000 au at a distance of 1 kpc) of AFGL 490; and a more extended emission region at a distance of 5–30'' (i.e. up to the primary beam size) from the central source. Interestingly, none of the transitions shows emission between these two regions. In the following, these emission regions will be treated in two separate parts, where a description

²*Astronomical Image Processing System, produced and maintained by the National Radio Astronomy Observatory, a facility of the National Science Foundation operated under cooperative agreement by Associated Universities, Inc. See <http://www.aips.nrao.edu>.*

of the observational characteristics at the beginning of each chapter is followed by the analysis, description of modelling process, and results.

3 Emission of the innermost region – the disc

In the following chapter, first a phenomenological description of the observational results for the emission up to 2'' (corresponding to 2000 au for a source distance of 1 kpc) from AFGL 490 is given, before the physical model of the disc used for the radiative transfer calculations is introduced. Finally, the modelling runs with different parameters and their results are discussed.

3.1. Observations

3.1.1 Continuum emission

AFGL 490 is readily detected as continuum source at 1 mm, 3 mm, 6 mm and 3.6 cm. The position, peak intensity and total flux (flux integrated inside of the 3σ contours) of the sources are collected in Tab. 3.1. For the 3.6 cm observations, the peak and integrated flux values are the average of the values obtained for the two image frequencies (8.48 and 8.43 GHz, respectively). The flux uncertainties include only the uncertainty resulting from the image noise σ , but not the absolute calibration error.

Table 3.1: Properties of the continuum sources: position, peak flux and total integrated flux (uncertainty corresponds to 1σ). The uncertainties are given in brackets in units of the last value digit. All sources are unresolved (i.e. extent \leq beamsize). See text for more explanations.

λ	Telescope (Config.)	#	RA (2000) (h m s)	Dec (2000) (° ' ")	Peak flux [mJy/beam]	Integrated flux [mJy]
1 mm ¹	PdBI	1	03:27:38.798 (2)	58:47:00.25 (2)	680 (80)	1440 (60)
3 mm	PdBI	1	03:27:38.814 (5)	58:47:00.25 (4)	160 (30)	250 (20)
6 mm	VLA(D)	1	03:27:38.799 (7)	58:47:00.22 (5)	12.5 (8)	15 (2)
6 mm	VLA(C)	1	03:27:38.796 (1)	58:47:00.22 (2)	13.2 (4)	32 (2)
3.6 cm	VLA(B)	1	03:27:38.800 (4)	58:47:00.25 (3)	0.58 (5)	0.90 (10)
		2	03:27:37.073 (7)	58:46:59.54 (7)	0.21 (3)	0.24 (5)
		3	03:27:39.136 (4)	58:47:10.7 (2)	0.14 (4)	0.13(5)
3.6 cm	VLA(A)	1	03:27:38.799 (1)	58:47:00.25 (1)	0.38 (3)	0.42 (2)
		2	03:27:37.074 (3)	58:46:59.54 (1)	0.17 (4)	0.18 (2)

⁽¹⁾ Observations published already by Schreyer et al. (2006), re-reduced measurements are included here for comparison.

Both in the PdBI 3 mm continuum observations (taken together with the C³⁴S and CH₃OH spectral line data), and the 6 mm continuum emission from the VLA-D array observations, AFGL 490 appears as an approximately beam-like shaped and unresolved source at the same

position as the 1 mm continuum (Schreyer et al. 2006). Contour plots of the continuum emission are shown in Fig. 3.1. The lowest contour shown (5σ) deviates somewhat from the beam shape in all cases, but since the distortion appears in different directions especially for the millimetre observations, they are not considered to be a hint for an underlying source shape.

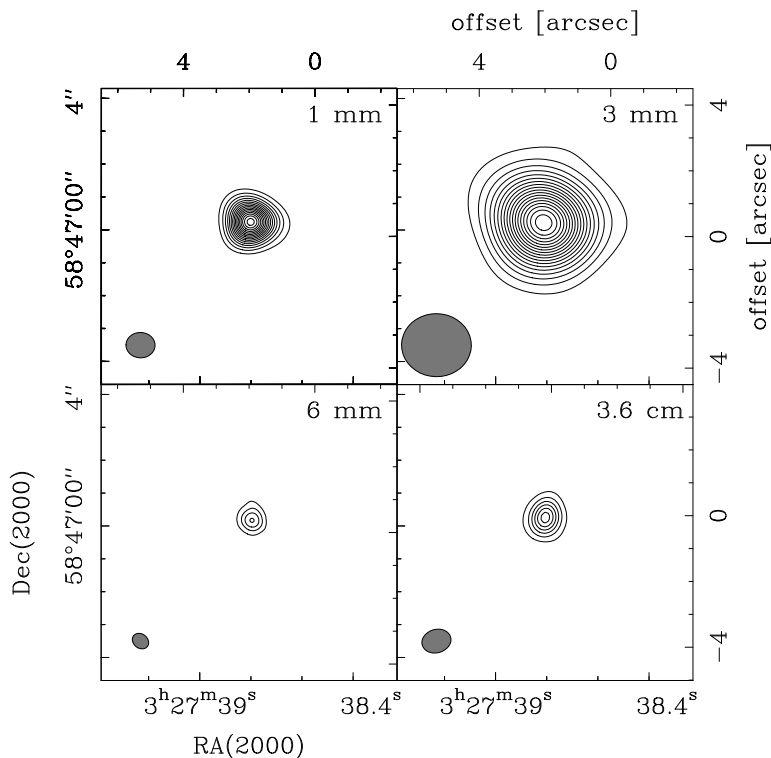


Figure 3.1: Continuum emission of AFGL 490 at various wavelengths. The contours start at 8σ and are spaced by the same value, with $\sigma = 5.2$ mJy/beam at 1 mm, 1.1 mJy/beam at 3 mm, 0.40 mJy/beam at 6 mm, and 0.011 mJy/beam at 3.6 cm. The synthesized beam sizes are indicated at the left bottom of each panel.

In the 3.6 cm continuum observations from the archival VLA-B array observations, three sources are detected at a significance level of $>5\sigma$. A modelling of the sources with an elliptical Gaussian using standard AIPS tasks results in source extents similar to the synthesized beam, i.e. all sources are unresolved. The brightest source coincides with the 1 mm and 3 mm continuum positions of AFGL 490. The second source, located $13''$ west of the brightest source, is located $0.1''$ from, and hence practically coincident with, the infrared source 2MASS 03273709+5846595. The third source detected in B configuration ($11''$ north of AFGL 490) does not seem to coincide with any of the infrared objects surrounding AFGL 490 nor any of the gas clumps detected in the spectral line observations analysed in this work. In the 3.6 cm observations in VLA(A) configuration, only the two brightest of the aforementioned sources are detected, but remain unresolved even with the $\sim 0.2''$ beam.

With maximum deviations of $0.1''$ (which may be the intrinsic uncertainty of radio-interferometric position measurements due to phase errors), the continuum source positions at all wavelengths are in good agreement and consistent with earlier radio position determinations (e.g. Campbell et al. 1986) of AFGL 490.

Campbell et al. (1986) noted significant diffuse extensions around the point-like main source

at 6 cm and 2 cm at up to about 80% of the peak brightness. Interestingly, these are not detected in the 3.6 cm observations considered here: slight deviations from an elliptic Gaussian are visible only around the 1σ level, and occur in different directions for both image frequencies. In the 3.6 cm VLA-A observations this could be due to filtering out of extended emission by the small interferometer beam, but this should not be the case for the 3.6 cm VLA-B observations, since they were obtained with a comparable VLA configuration as the 2 cm observations of Campbell et al. (1986). This points at a variability of the extended centimetre emission on a timescale of a decade. A short side note of this vanishing of the extended emission (probably from the same data set) was already mentioned by Alvarez et al. (2004), but the detailed discussion delayed to a later publication.

However, the integrated 3.6 cm continuum flux of AFGL 490 is in very well agreement with the power-law spectral distribution at centimetre wavelength, $S_\nu \propto \nu^\gamma$ with $\gamma = 1.23 \pm 0.2$, found by Campbell et al. (1986). Including the 3.6 cm continuum flux, a slope of 1.24 ± 0.2 is obtained, which is – as already discussed by Campbell et al. (1986) – lower than the slope of $\gamma = 2$ expected for an optically thick compact source but higher than the $\gamma = 0.6$ slope predicted for a constant velocity ionized wind.

Extrapolating this spectral behaviour to millimetre wavelengths yields a contribution of the free-free emission of $56 \pm_{22}^{36}$ mJy to the continuum flux at 1 mm, $19 \pm_6^8$ mJy at 3 mm, and 9 ± 2 mJy at 6 mm. These values represent only an upper limit, since at some wavelength shortward of 1.3 cm (see Campbell et al. 1986) a turnover in the free-free radiation spectrum is expected at the transition between optically thick and optically thin regime, where the power-law index decreases to -0.1 (e.g. Rohlfs & Wilson 1996), and hence the flux does not increase any further. Therefore, the contribution of free-free radiation at the millimetre wavelengths should be between the aforementioned upper limits and the highest value measured at centimetre wavelengths, i.e. 3.2 mJy (Campbell et al. 1986, and references therein).

The 3 and 6 mm integrated fluxes can be used to compare with the disc mass estimate obtained from the 1 mm continuum flux by Schreyer et al. (2006). Assuming optically thin thermal dust emission, the disc mass is estimated from:

$$M_{\text{disc}} = \frac{S_\nu d^2}{\kappa_d(\nu) B_\nu(T_d)} \frac{M_{\text{gas}}}{M_{\text{dust}}}, \quad (3.1)$$

(see, e.g. Henning et al. 2000) with S_ν denoting the continuum flux (with contribution of free-free radiation subtracted), d the source distance (1 kpc), $B_\nu(T_d)$ the Planck function for the dust temperature T_d (assumed as 100 K as a typical value) at the observing frequency ν , $M_{\text{gas}}/M_{\text{dust}}$ the gas-to-dust ratio (assumed to be 100 here), and $\kappa_d(\nu)$ the dust opacity at the observing frequency. For the dust opacities, the values for protostellar cores by Ossenkopf & Henning (1994) for grains without ice mantles at gas densities of 10^6 – 10^8 cm $^{-3}$ are extrapolated to wavelengths of 3 and 6 mm, yielding 0.6–2.0 and 0.2–0.8 cm 2 /g, re-

spectively, to allow for comparison with Schreyer et al. (2006). Taking into account the spread of dust opacities, uncertainty of the integrated flux value and the uncertainty of the free-free radiation contribution, rather broad ranges of disc masses of $2.0\text{--}6.9 M_{\odot}$ for 3 mm and $0.5\text{--}3.9 M_{\odot}$ for 6 mm result. In any case, all three estimates from 1, 3 and 6 mm have the values of $M_{\text{disc}} \approx 2.0\text{--}2.3 M_{\odot}$ in common.

3.1.2 Spectral line emission

In the interferometric $\text{C}^{17}\text{O}(2\text{--}1)$ data published by Schreyer et al. (2006), the most prominent emission feature was a 700×2000 au bar-like structure around the 1 mm continuum peak with a position angle of 26° , the south-eastern part of which shows emission between -15.0 and -13.0 km/s, i.e. blueshifted to the system velocity, and the north-western part redshifted emission between ca. -12.5 and -9.5 km/s – according to its velocity structure it was interpreted as the signature of a rotating disc. All other datasets, i.e. C^{34}S , CS and CH_3OH , show tentative line emission from at least two velocity components more or less symmetrically around the AFGL 490 continuum peak as well, however, they are all less distinctive than in C^{17}O . While for C^{17}O the signal-to-noise-ratio of the line peaks reaches 7, it is only slightly above or even below 3 for the other data sets (except CS observed in VLA-D configuration, with line peaks up to 5 r.m.s). In Fig. 3.2 to 3.5, contour plots of the supposed blue- and redshifted emission (where the maximum extent of blue- and redshifted emission was estimated visually from the spectra cubes) for each transition are shown along with spectra from (or close to) the peaks of both velocity components, and a spectrum integrated over the whole (blue- plus redshifted, within the 1σ contour) emission region are displayed. Except of the earlier C^{17}O data with a smaller synthesized beam, spectra of the other transitions at any positions around AFGL 490 show traces of both blue- and redshifted emission, since the size and separation of the according emission regions is close to or smaller than the beam size.

The separation between blue- and redshifted maximum, the position angle of the vertical to the connecting line between both, and the offset of its midpoint from AFGL 490 are collected in Tab. 3.2. The uncertainties were estimated by varying the positions within a 95% contour of the maxima; they are high especially for the position angle due to spatially broad maxima likely resulting from the low spatial resolution of the data sets considered in this work (i.e. synthesized beam size larger than separation of maxima).

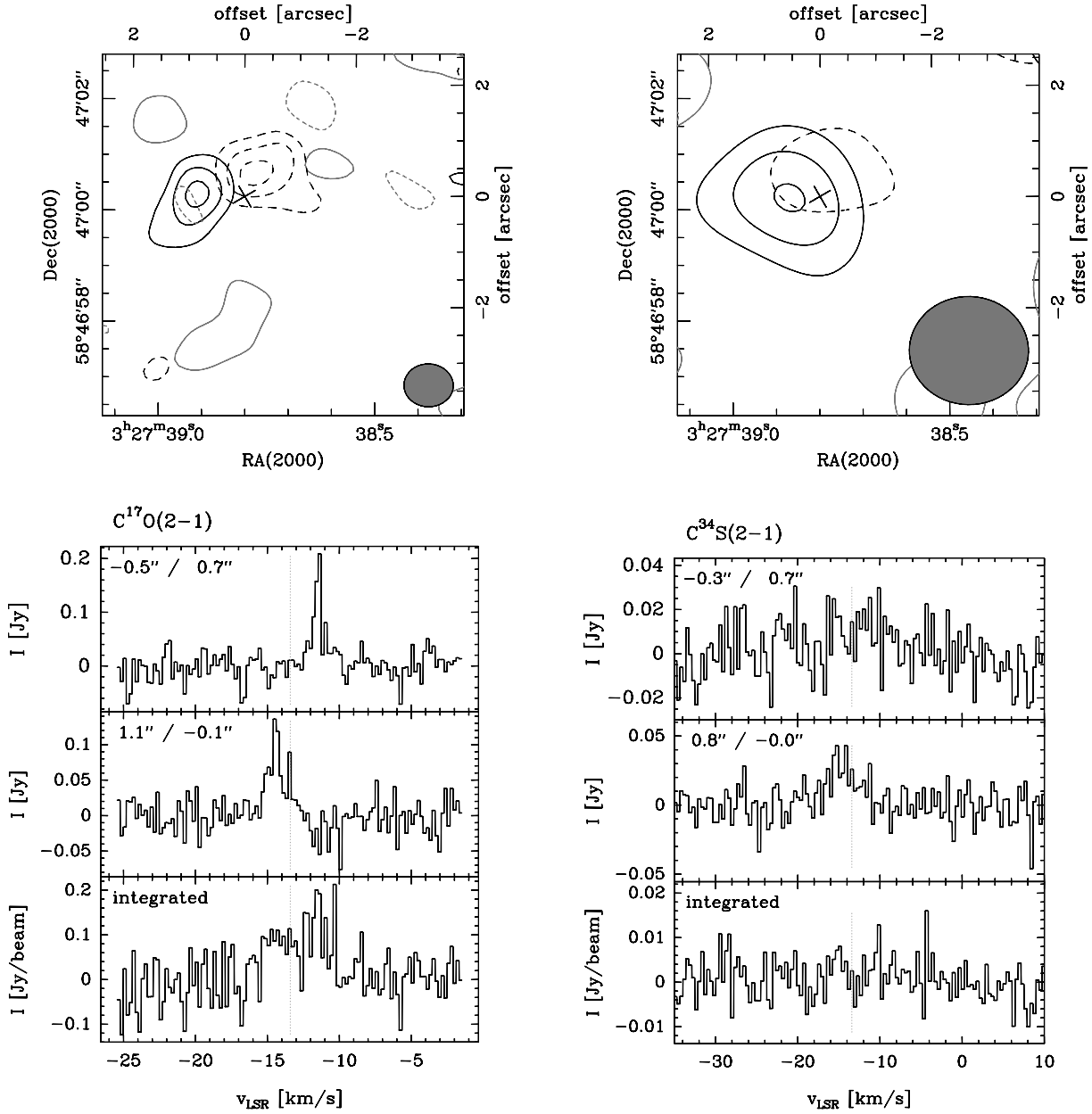


Figure 3.2: Upper panels: Contour maps of the red- (dashed) and blueshifted (solid lines) emission around AFGL 490 for $C^{17}O$ (blue: $[-15.3, -13.3]$ km/s, red: $[-12.5, -9.5]$ km/s) and $C^{34}S$ (blue: $[-16.5, -13.1]$ km/s, red: $[-12.9, -9.0]$ km/s). The contours start at 2.0σ and 1.5σ , respectively, and are equally spaced by the same value; grey dashed and solid lines show the corresponding negative contours. The synthesized beam size is indicated in the lower right corner, a cross marks the continuum position of AFGL 490.

Lower panels: Spectra of $C^{17}O$ (smoothed by a factor 2) and $C^{34}S$ (smoothed by a factor 3) at the maximum position of redshifted (top) and blueshifted emission (middle), and emission integrated over the region inside the 1σ contour covering both blue- and redshifted emission. The dotted vertical line denotes $v_{LSR} = -13.4$ km/s.

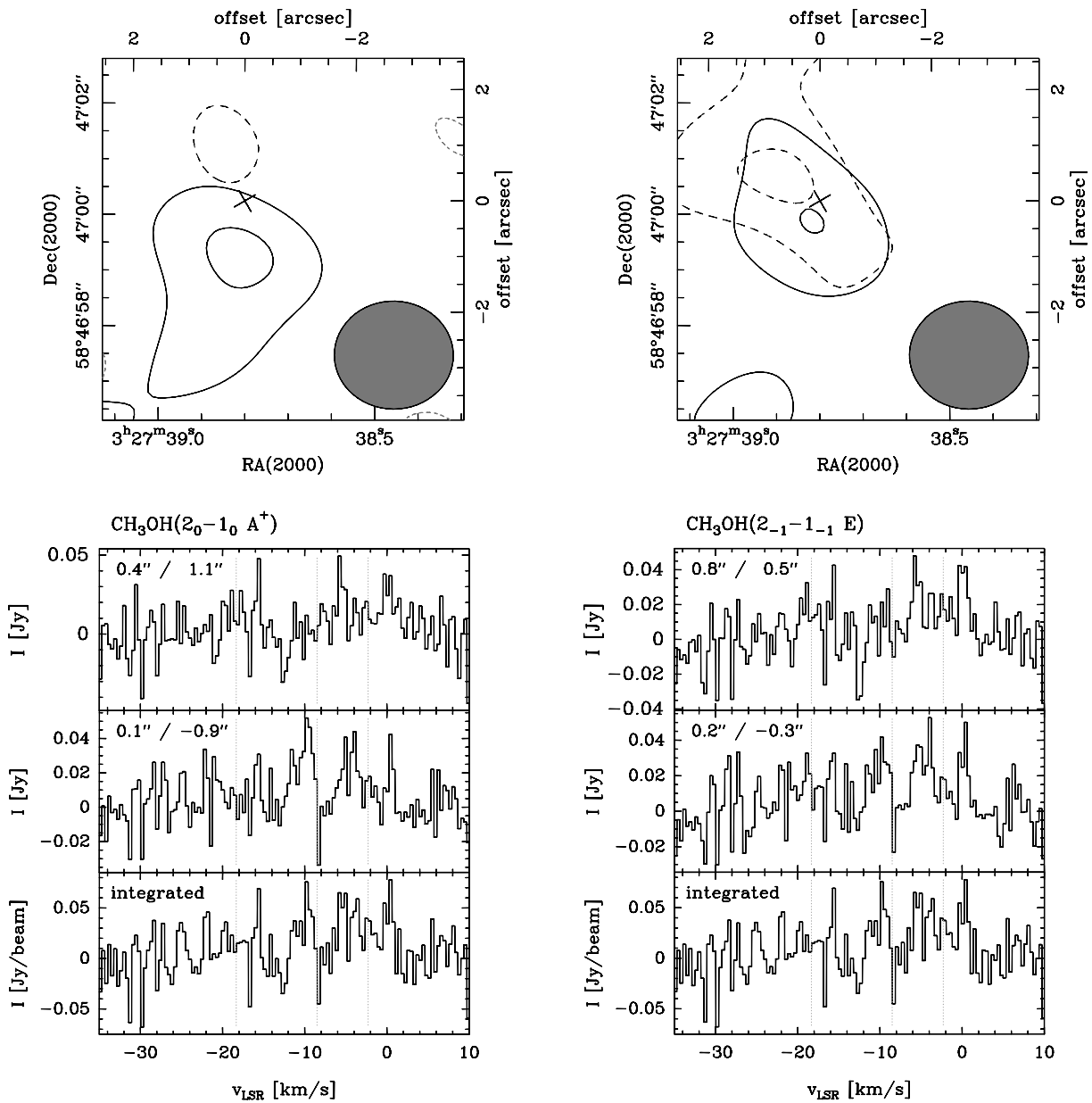


Figure 3.3: Upper panels: Contour maps of the red- (dashed) and blueshifted (solid lines) emission around AFGL 490 for $\text{CH}_3\text{OH}(2_0-1_0 A^+)$ (blue: $[-11.6, -8.5]$ km/s, red: $[-8.5, -5.4]$ km/s) and $\text{CH}_3\text{OH}(2_{-1}-1_{-1} E)$ (blue: $[-5.4, -2.3]$ km/s, red: $[-2.3, +0.8]$ km/s). The contours start at 1.8σ and 2.0σ , respectively, and are equally spaced by the same value; grey dashed and solid lines show the corresponding negative contours. The synthesized beam size is indicated in the lower right corner, a cross marks the continuum position of AFGL 490.

Lower panels: Spectra of $\text{CH}_3\text{OH}(2_0-1_0 A^+)$ and $\text{CH}_3\text{OH}(2_{-1}-1_{-1} E)$, both smoothed by a factor 2, at the maximum position of redshifted (top) and blueshifted emission (middle), and emission integrated over the region inside the 1σ contour covering both blue- and redshifted emission. The three dotted vertical lines denote the line position for a $v_{\text{LSR}} = -13.4$ km/s.

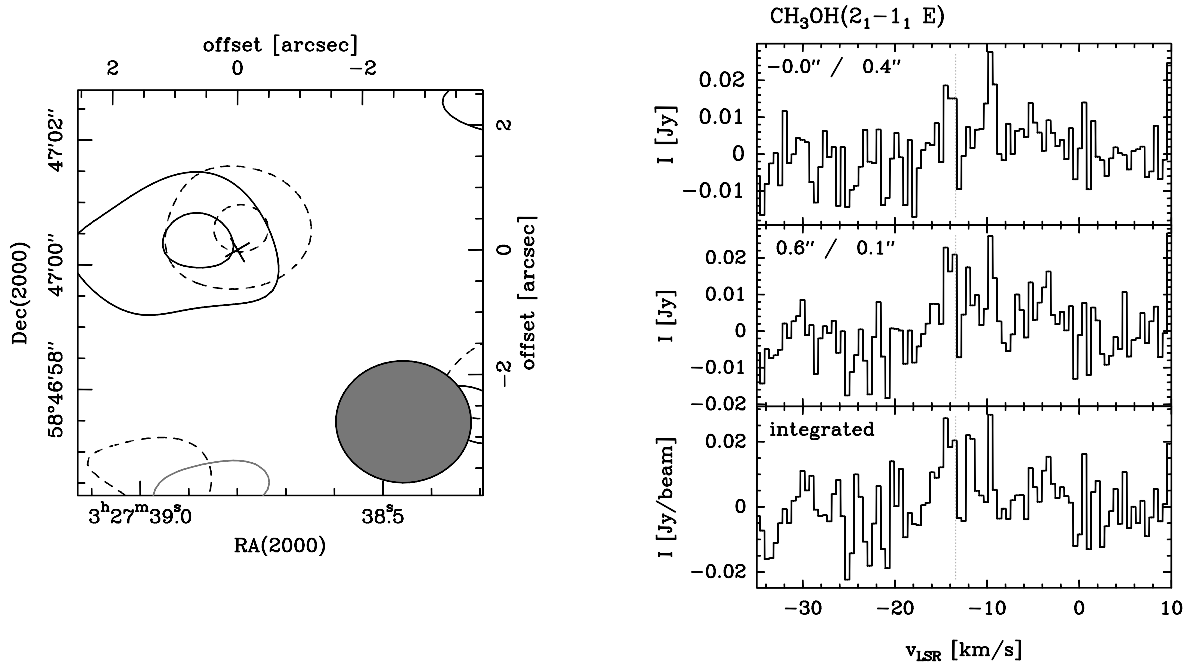


Figure 3.4: Left panel: Contour map of the red- (dashed, $[-14.9, -13.3]$ km/s) and blueshifted (solid lines, $[-10.3, -8.8]$ km/s) emission around AFGL 490 for $\text{CH}_3\text{OH}(2_1-1_1 \text{ E})$. The contours start at 1.7σ and are equally spaced by the same value; grey dashed and solid lines show the corresponding negative contours. The synthesized beam size is indicated in the lower right corner, a cross marks the continuum position of AFGL 490. Right panel: Spectra of $\text{CH}_3\text{OH}(2_1-1_1 \text{ E})$ smoothed by a factor 2 at the maximum position of blueshifted (top) and redshifted emission (middle), and emission integrated over the region inside the 1σ contour covering both blue- and redshifted emission. The dotted vertical line denotes $v_{\text{LSR}} = -13.4$ km/s.

Table 3.2: Geometry of the line emission close to AFGL 490: offset of the midpoint between blue- and redshifted emission maximum from AFGL 490 ($\alpha = 03^{\text{h}}27^{\text{m}}38.80^{\text{s}}$, $\delta = 58^{\circ}47'00.24''$), separation of the maxima, position angle of the vertical to the connecting line, and approximate velocity range of the blue/redshifted emission. Uncertainties are given in brackets in units of the last digit of the preceding value.

Transition	Offset RA [$''$]	Offset Dec [$''$]	Sep. [$''$]	PA [$^{\circ}$]	v_{blue} [km/s]	v_{red} [km/s]
$\text{C}^{17}\text{O}(2-1)^1$	0.37 (5)	0.20 (5)	1.0 (3)	16 (13)	$[-15.3, -13.3]$	$[-12.5, -9.5]$
$\text{C}^{34}\text{S}(2_0-1_0)$	0.20 (10)	0.21 (7)	0.9 (6)	35 (53)	$[-16.5, -13.1]$	$[-12.9, -9.0]$
$\text{CH}_3\text{OH}(2_{-1}-1_{-1} \text{ E})$	0.45 (10)	0.05 (7)	1.0 (8)	127 (45)	$[-5.4, -2.3]^2$	$[-2.3, 0.8]^2$
$\text{CH}_3\text{OH}(2_0-1_0 \text{ A}^+)$	0.21 (6)	0.05 (4)	2.0 (8)	99 (19)	$[-11.6, -8.5]^2$	$[-8.5, -5.4]^2$
$\text{CH}_3\text{OH}(2_1-1_1 \text{ E})$	0.26 (10)	0.25 (5)	0.6 (6)	20 (53)	$[-14.9, -13.3]$	$[-10.3, -8.8]$
CS(1-0) D array	-0.15 (8)	-0.19 (5)	1.0 (4)	64 (41)	$[-17.6, -12.8]$	$[-12.2, -8.6]$
CS(1-0) C array	0.06 (8)	0.01 (5)	0.2 (2)	335 (45)	$[-15.7, -13.1]$	$[-11.9, -8.6]$

(1) Observations published already by Schreyer et al. (2006); re-reduced data included here for comparison.

(2) Values assumed, see text.

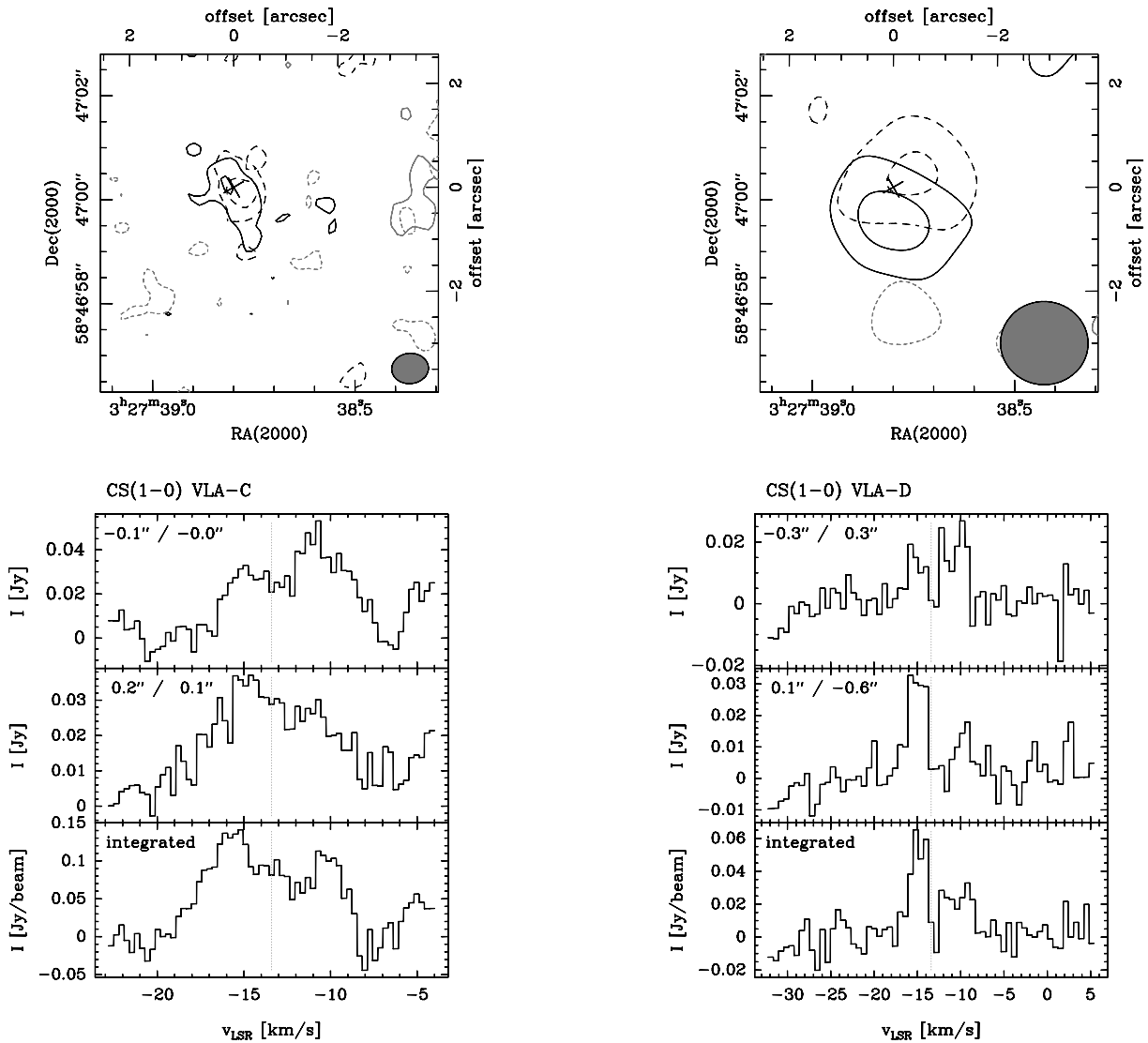


Figure 3.5: Upper panels: contour maps of the red- (dashed) and blueshifted (solid lines) emission around AFGL 490 for CS VLA-C array (blue: $[-15.7, -13.1]$ km/s, red: $[-11.9, -8.6]$ km/s) and CS VLA-D array (blue: $[-17.6, -12.8]$ km/s, red: $[-12.2, -8.6]$ km/s). The contours start at 2.0σ and 2.5σ , respectively, and are equally spaced by the same value; grey dashed and solid lines show the corresponding negative contours. The synthesized beam size is indicated in the lower right corner, a cross marks the continuum position of AFGL 490.

Lower panels: spectra of CS in VLA-C and VLA-D array at the maximum positions of blueshifted (top) and redshifted emission (middle), and emission integrated over the region inside the 1σ contour over the full range of blue- and redshifted emission. The dotted vertical line denotes $v_{\text{LSR}} = -13.4$ km/s.

$C^{34}S$

In the $C^{34}S$ observations, two separated emission regions are visible at locations comparable to the earlier $C^{17}O(2-1)$ data. The south-eastern region of emission, blueshifted relative to the system v_{LSR} , is dominated by a narrow line component at $v_{LSR} = -15.3$ km/s; the main line component of the north-western, less intense, redshifted emission region is located at $v_{LSR} = -10.1$ km/s. The position angle of the line connecting both maxima is larger than for $C^{17}O$, but in agreement with the latter taking into account the large uncertainties.

CS

The CS(1-0) data from VLA-D array observations show two distinct velocity components as well, peaking at -15.6 km/s and -10.9 km/s, respectively, and separated by $1.0''$. While the red-shifted component appears at similar location as in the $C^{34}S$ data, the blue-shifted component is located more to the south, so that the line connecting these regions has a larger position angle than these of the disc-like features seen in $C^{34}S$ and $C^{17}O$. From spectra maps around the center position it appears that there are additional velocity components peaking at $v_{LSR} = -18.8$ km/s and -6.1 km/s, which have their maximum brightness slightly ($< 0.5''$) south and north of the continuum position, respectively. Since CS(1-0) traces less dense gas ($n_{crit} \approx 10^4$ cm $^{-3}$) than the other transitions considered in this work, it is possible that the CS(1-0) emission is contaminated with additional gas and stems not only from the dense disc-like object in the center.

In the VLA-C array CS data, the more extended emission seems to be resolved out by the small synthesized beam. Nevertheless, a redshifted (peaking at -15.6 km/s) and blueshifted (-10.4 km/s) component are discernable, the peaks of which have a very small separation of $< 0.5''$. Here, possibly only the innermost densest parts of the disc might be traced – this is however not supported by the range of blue-/red shift being comparable to the other transitions.

CH_3OH

For the $CH_3OH(3)$ data set containing three lines, the situation is somewhat more complicated, since the lines ($2_{-1}-1_{-1}E$) and ($2_0-1_0A^+$) are separated by 6.2 km/s, which is not far from the separation between red- and blueshifted components seen in the other transitions, and therefore an overlap of different velocity components of these lines is likely. In the observational setup used, the three lines would be situated at -4.91 km/s, $+4.91$ km/s and $+11.13$ km/s from the v_{LSR} of the gas clump giving rise to the emission (i.e. for the system velocity of -13.4 km/s, lines are expected at -18.3 , -8.5 and -2.3 km/s). For the integrated emission of the two strongest lines ($2_{-1}-1_{-1}E$) and ($2_0-1_0A^+$) in Fig. 3.4, based upon the velocity ranges of the other transitions and to avoid overlapping, velocities between -16.5 and -13.4 km/s are considered as blueshifted, and between -13.4 and -10.3 km/s as redshifted (i.e. an interval of 3.1 km/s below and

above the AFGL 490 system velocity). With these ranges, the suspected blue-/redshifted peaks in Fig. 3.4 appear to be oriented rather perpendicular to the line connecting the $C^{17}O$ maxima (the supposed disc plane). Therefore it is doubtful if this $CH_3OH(3)$ emission arises from the same disc-like structure, especially since the emission in the wider environment of AFGL 490 assigned to the outflow walls – which will be discussed chapter Fig. 4.1 – appears at similar v_{LSR} velocities.

In contrast, the $CH_3OH(1)$ data set containing the transition $(2_1-1_1 E)$ shows red- and blueshifted components at positions similar to those of $C^{17}O$; however, these lines are weak.

In summary, the respective orientation of blue- and redshifted maxima is comparable to that of $C^{17}O$ for $C^{34}S$, $CH_3OH(2_1-1_1 E)$ and CS within the uncertainties, while for the $CH_3OH(2_{-1}-1_{-1} E)$ and $(2_0-1_0 A^+)$ lines it is almost perpendicular to the former.

The integrated spectra enclosing both red- and blueshifted emission in Fig. 3.2–3.5 were approximated with two Gaussian line profiles for a rough quantitative description (although their profiles deviate from Gaussian shape). The results are summarized in Tab. 3.3. While the central velocity agrees within the uncertainties for all transitions at a value somewhat lower than the system velocity of AFGL 490 ($v_{LSR} = -13.4$ km/s), the average shift of the supposed red- and blueshifted lines increases from 1.4 km/s for $C^{17}O$ to 2 km/s for CH_3OH and 2.5 km/s for CS and $C^{34}S$. Both the line width and peak intensities differ significantly between red- and blueshifted component for some of the observed transitions, however, the lines both in the integrated spectra as well as at the red/blueshifted maxima do not show a well-defined smooth shape like in $C^{17}O$ in these cases, which could point to an origin from a clumpy rather than a smooth gas distribution.

Integrated intensity

Schreyer et al. (2006) noted that the integrated (over red- and blueshifted parts) intensity of the disc-like emission feature in $C^{17}O$ has an arc-shaped appearance with the bulk of emission located north-east of the continuum peak.

In Fig. 3.6, the integrated intensity for $C^{17}O$ is shown along with that for $C^{34}S$, CS (VLA-D array) and $CH_3OH(2_1-1_1 E)$. For $C^{34}S$ and $CH_3OH(2_1-1_1 E)$, the peak of the integrated line emission appears shifted eastward of the continuum peak, in case of the VLA CS observations, it is shifted south-east – possibly the result of the fact that the blue-shifted emission shown in Fig. 3.2-3.5 is more prominent than the redshifted. However, for these molecular line observations the synthesized beam size is considerably larger than for $C^{17}O$ and therefore does not allow to confirm or rule out the arc-like appearance observed in $C^{17}O(2-1)$.

Table 3.3: Parameters of a two-Gaussian approximation to the integrated spectra in Fig. 3.2–3.5: central velocity midway between red- and blueshifted line component ($v_{\text{mid}} = \frac{v_{\text{red}} + v_{\text{blue}}}{2}$), velocity shift of the red/blueshifted line from the central velocity ($v_{\text{shift}} = \frac{v_{\text{red}} - v_{\text{blue}}}{2}$), average line width Δv of both components (not corrected for instrumental broadening), and peak intensities of the red/blueshifted components, respectively. The quoted uncertainties include only the uncertainties of the fitting process. All parameter are only rough descriptions since the “lines” are of low signal-to-noise-ratio and often not gaussian shape.

Transition	v_{mid} [km/s]	v_{shift} [km/s]	Δv [km/s]	I_{blue} [mJy]	I_{red} [mJy]
$\text{C}^{17}\text{O}(2-1)^1$	-12.9 ± 0.2	1.4 ± 0.2	2.0 ± 0.6	108 ± 41	147 ± 45
$\text{C}^{34}\text{S}(2_0-1_0)$	-12.7 ± 0.2	2.4 ± 0.2	1.0 ± 0.7	8 ± 4	11 ± 5
$\text{CH}_3\text{OH}(2_0-1_0 \text{ A}^+)$	-12.6 ± 0.2	2.2 ± 0.2	1.7 ± 0.8	49 ± 20	55 ± 24
$\text{CH}_3\text{OH}(2_{-1}-1_{-1} \text{ E})$	-13.1 ± 0.2	2.0 ± 0.2	1.1 ± 0.6	57 ± 38	61 ± 25
$\text{CH}_3\text{OH}(2_1-1_1 \text{ E})$	-12.7 ± 0.5	1.8 ± 0.5	2.5 ± 1.9	24 ± 12	11 ± 6
CS(1-0) C array	-12.9 ± 0.2	2.5 ± 0.2	3.3 ± 1.2	121 ± 17	99 ± 26
CS(1-0) D array	-12.8 ± 0.3	2.4 ± 0.3	2.5 ± 1.1	58 ± 12	21 ± 8

(1) Observations published already by Schreyer et al. (2006); included here for comparison.

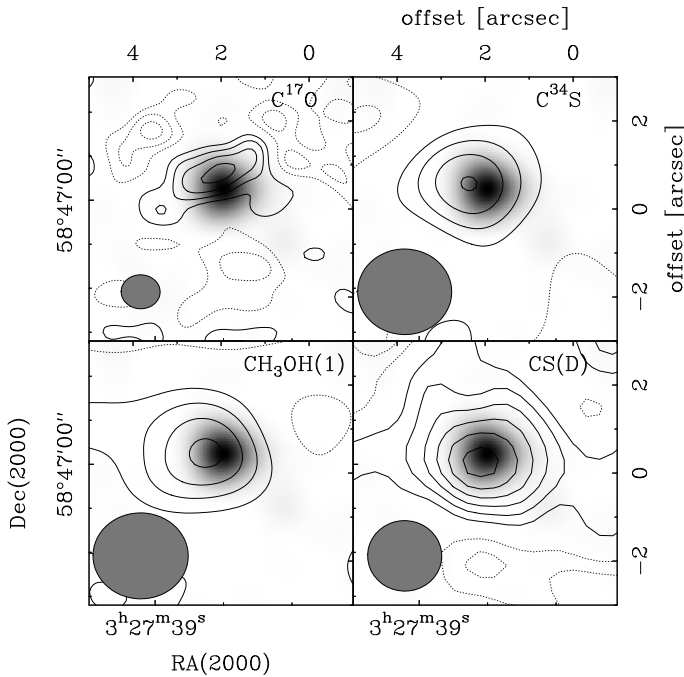


Figure 3.6: Contour plots for $\text{C}^{17}\text{O}(2-1)$, $\text{C}^{34}\text{S}(2-1)$, $\text{CH}_3\text{OH}(2_1-1_1 \text{ E})$ and CS(1-0) VLA(D) of the emission integrated over the whole red- and blueshifted velocity range given in Tab. 3.2, superimposed on a grey-scale image of the 1.3 mm continuum emission. The contours start at 1σ of the corresponding integrated intensity images and are equally spaced by the same value; the offset in arcsec is from the phase reference centre. The C^{17}O data were already published in Schreyer et al. (2006) and are included here for comparison.

Position-velocity-diagrams

For another view on the velocity structure of the emission around AFGL 490, position-velocity-diagrams are collected in Fig. 3.7 and 3.8. For this, a cut along a line starting at the 1σ contour and proceeding through the blue- and redshifted emission maxima in the contour maps in Fig. 3.2–3.5 is taken. In Fig. 3.7, the cut line from $C^{17}O$ is used also for all other transitions, while in Fig. 3.8, for each transition the cut from blue- to redshifted emission of the respective transition is shown. The lower spatial resolution of most other observations compared to $C^{17}O$ is perceivable in the larger extent of the emission along the axis with positional offset. Structures resembling the "S"-shaped pattern of the $C^{17}O$ emission, roughly symmetric about the center of the plot and indicative of rotation (e.g. Harsono et al. 2014), are detectable in $C^{34}S$ and CS (VLA-D array), but not clearly visible in the other panels.

To obtain estimates of the parameters of a Keplerian or other power-law velocity curve, the position-velocity (PV) diagrams were analysed according to the following steps. First, the positions of maxima (exceeding 2σ) in the cuts displayed in Fig. 3.7 and 3.8 were determined channel-by-channel, where the maxima were approximated with Gaussians. Usually the determination of positions in the uv-plane rather than the image plane is preferred (e.g. Harsono et al. 2014), this approach was not used here since especially in CS and $C^{34}S$ the strong emission in the nearby outflow region adulterated fitting the emission positions close to AFGL 490. For the fitting, only maxima within the velocity range given in Tab. 3.2 were taken into account. Furthermore, points close to the midpoint system velocity of AFGL 490 ($v_{LSR} \approx -13.4$ km/s) which do not follow the expected relation – i.e., v decreasing with increasing positional offset from the assumed disc axis, which is not the case for the roughly diagonal distribution seen between -12 and -14 km/s in $C^{17}O$ in Fig. 3.7 – were masked out for the fitting process. This partially visual selection may be prone to bias, but is necessary due to the sparsity of data points.

To determine a midpoint or centre of symmetry of the PV diagrams (p_{mid}, v_{mid}), both values were varied and the value chosen, for which the sum of distances (weighted by the number of points) of points on both sides of the value is closest to equality, i.e. $\sum_{i=1}^N |v_i - v_{mid}|/N - \sum_{j=1}^M |v_j - v_{mid}|/M$ is minimized, where $i = 1 \dots N$ are points with $v > v_{mid}$ and $j = 1 \dots M$ are points with $v < v_{mid}$ (and accordingly for the positional offset p_{mid}). Occasionally, for p_{mid} several equally deep minima occurred, in this case the value was chosen which produced the smallest residuals in the following fitting procedure. To the remaining points, a function of the form

$$v(p) = v_0 \times (p - p_{mid})^q + v_{mid}, \quad (3.2)$$

is fitted, with an exponent q for the velocity law. For a disc in Keplerian rotation viewed under an inclination angle i , $q = -0.5$ and $v_0 = \sqrt{GM_\star} \times \sin(i)$, where the offset $p - p_{mid}$

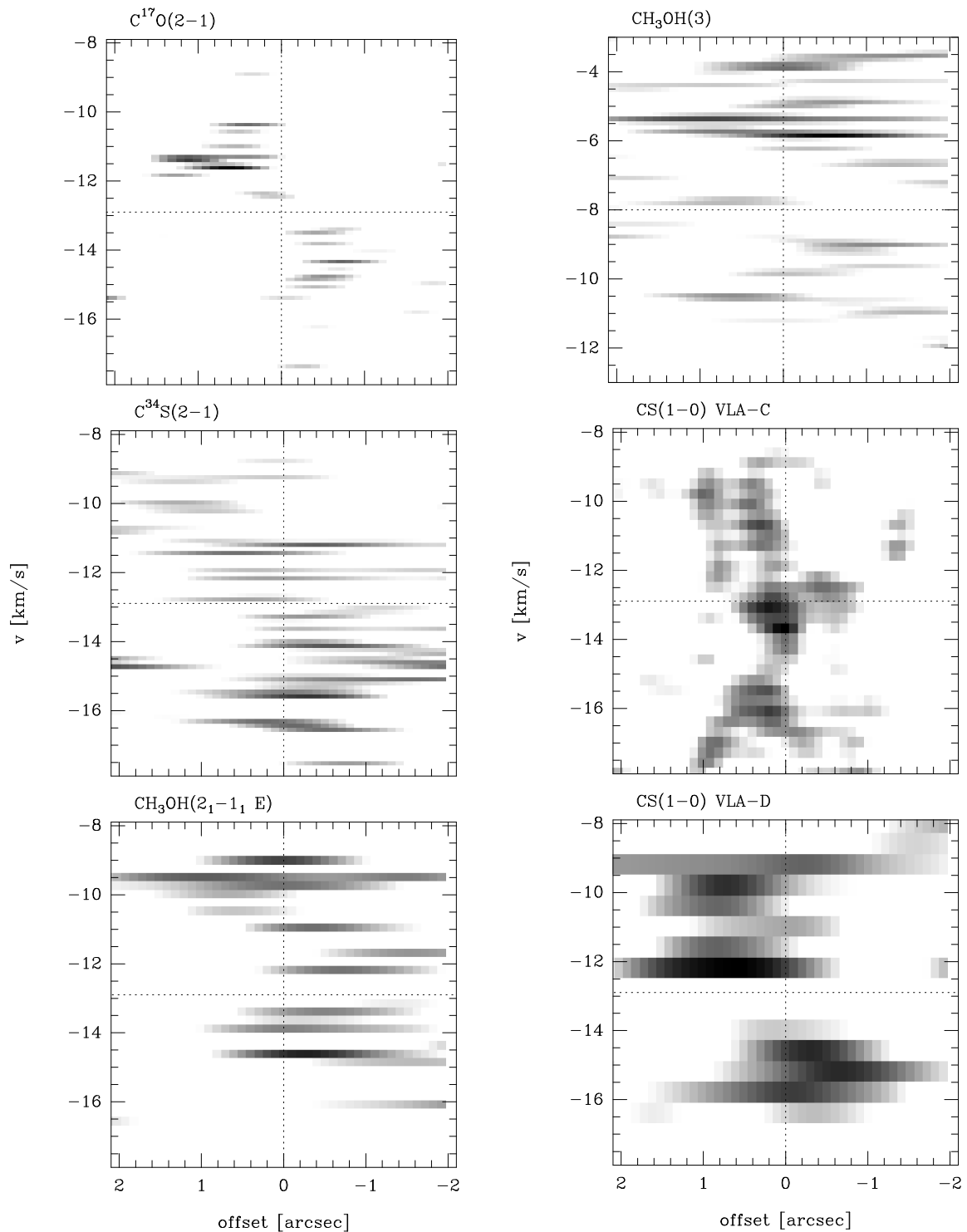


Figure 3.7: Position-velocity diagrams for all observed transitions. A cut along the line connecting blue- and redshifted maximum of the $C^{17}O$ emission is used for all transitions, the dotted lines mark the middle between blue and red $C^{17}O$ peak and $v_{LSR} = -12.9$ km/s, respectively.

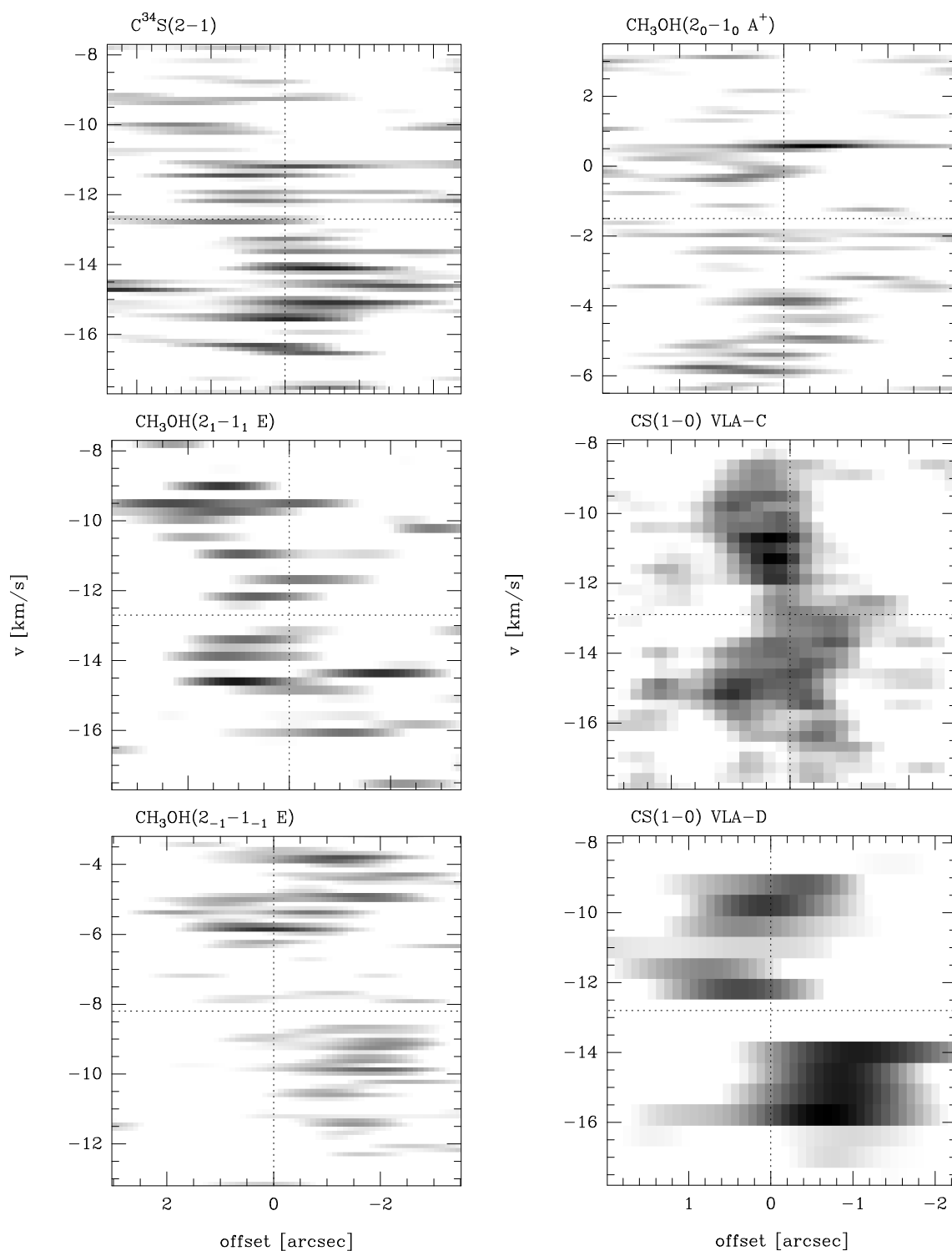


Figure 3.8: Position-velocity diagrams for all observed transitions. For each transition, the cut is taken along the line connecting the blue and red maximum of the according transition, the dotted horizontal and vertical line denote the middle between these maxima and the central velocity for the according transition given in Tab. 3.3 (note the different scale in positional offset, large ticks are separated by $1''$).

has been converted to the physical separation from AFGL 490 assuming the distance of 1 kpc, and the mass of the disc itself is neglected. For the fitting, the sum of distances both in p - and v -direction between points and model curve, weighted by the positional uncertainties and the velocity channel width, is minimized. To estimate the fit uncertainty, the position of the maxima in each velocity channel were varied randomly within a Gaussian distribution with the same σ as their positional uncertainty (since the relative velocity uncertainty is small compared to the relative positional uncertainty). From the resulting distribution of the fit parameter, an lower and upper limit of v_0 was calculated such, that 68.3% of all values fall in this range (the distribution of v_0 is not Gaussian for $C^{17}O$, therefore the uncertainties are not symmetric about the best fit value).

The resulting parameters of a fit with Keplerian velocity profile, and one fit with also q being varied, for $C^{17}O$, $C^{34}S$ and $CS(D)$ are collected in Tab. 3.4. For this, the cuts along the line connecting the $C^{17}O$ maxima (Fig. 3.7) were taken for all three transitions, while the cuts along the $C^{34}S$ and $CS(D)$ maxima (Fig. 3.8) yield significantly worse fits. The best-fit Keplerian velocity profiles ($q = -0.5$) are illustrated in Fig. 3.1.2; clearly the $C^{34}S$ profile represents the least acceptable fit and deviates in v_{mid} , which was already anticipated since the blue- and redshifted points show partially overlapping positions.

Table 3.4: Parameters of velocity profile fits to the position-velocity diagrams of $C^{17}O$, $C^{34}S$ and CS (VLA-D array): exponent of the velocity profile (in the first three rows fixed to -0.5), best-fit value v_0 and its 1σ range, symmetry point of the PV diagram, and χ^2 (non-reduced, i.e. sum of weighted squared residuals) of the fit (see also equation 3.2 and Fig. 3.1.2).

Transition	q	v_0 [km/s]	Range of v_0 [km/s]	v_{mid} [km/s]	p_{mid} [arcsec]	χ^2
$C^{17}O(2-1)^1$	-0.5	43.3	26.5...51.8	-12.88	2.004	103
$C^{34}S(2_0-1_0)$	-0.5	41.7	0.1...44.9	-13.25	2.186	1631
$CS(1-0)$ D config.	-0.5	39.6	0.1...45.1	-12.58	1.868	11
$C^{17}O(2-1)^1$	-0.55	61.2	32.9...76.5	-12.88	2.004	101
$C^{34}S(2_0-1_0)$	-0.21	8.1	2.5...9.2	-13.25	2.186	937
$CS(1-0)$ D config.	-0.48	35.7	23.5...51.5	-12.58	1.868	10

For the Keplerian $q = -0.5$ case, the values of v_0 agree for all three PV diagrams to within 10%. Since v_0 depends both on central object mass and disc inclination, several combinations of both are possible, but cannot be disentangled from the PV diagram alone. For a stellar mass of $8 M_\odot$, the best-fit v_0 would correspond to a disc inclination of $(29 \pm 2)^\circ$. Taking into account the whole 1σ range of v_0 from Tab. 3.4, all transitions agree on an

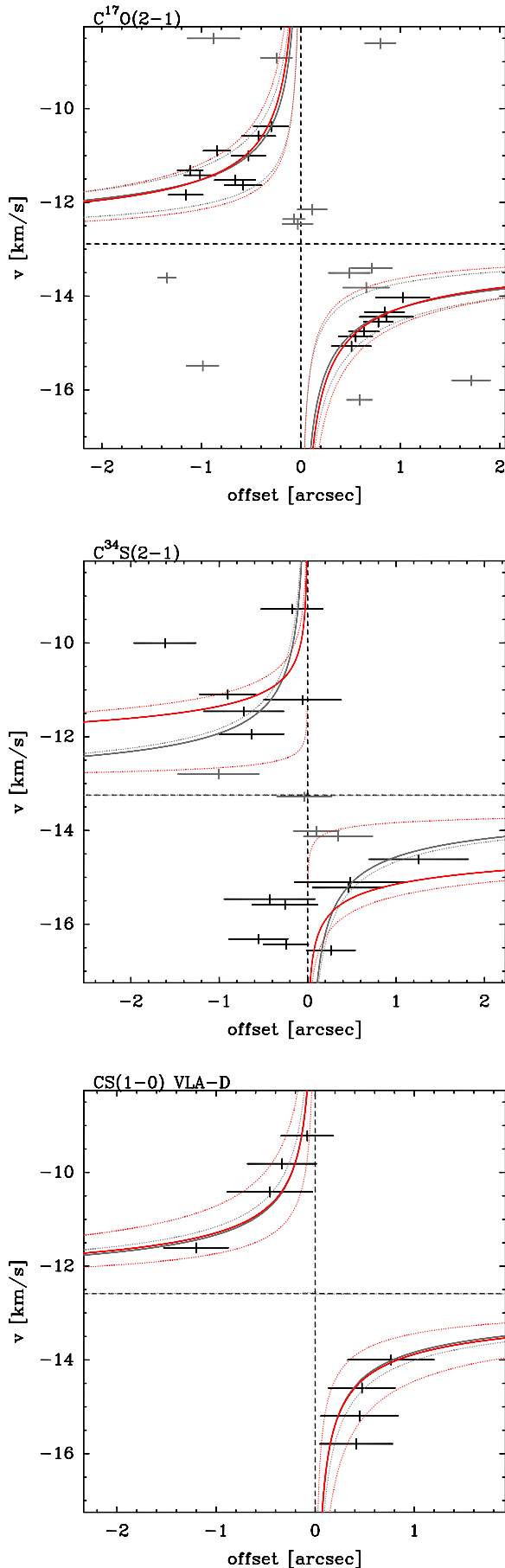


Figure 3.9: Best-fit velocity profiles for $C^{17}O$, $C^{34}S$ and $CS(D$ array). The positions of maximum emission in each velocity channel from Fig. 3.7 with their errorbars are indicated with crosses, where the grey points were not used for the fitting. The best-fit Keplerian ($q = -0.5$) profile is indicated by a solid dark grey line, the best fit velocity profile with a red line; the according 1σ limits given in Tab. 3.4 are shown with dotted lines in the same colour.

upper limit of $i = 38^\circ$, while the lower limit is 18° for $C^{17}O$, but $C^{34}S$ and $CS(D)$ do not exclude even a pole-on configuration of the disc (in both cases due to the fact that some points with the highest red/blueshift overlap in position, possibly due to the lower spatial resolution of these observations). For a $2 M_\odot$ lower or higher stellar mass, the inclination would increase or decrease by about 5° , respectively, while a low mass central object ($2 M_\odot$) would require an inclination as high as 80° , which is unlikely since the morphology of the emission especially in $C^{17}O$ is not in agreement with such a highly inclined disc.

Varying the exponent of the velocity law, the sum of residuals reaches a minimum for q very close to the Keplerian case for $C^{17}O$ and $CS(D)$ ($q = -0.48$ and -0.55 , respectively), but for a shallower profile ($q = -0.21$) in the case of $C^{34}S$. Adopting a velocity law where the disc mass inside a given radius from the central star is taken into account and assumed to rise linearly up to $1 M_\odot$ to an outer disc radius of 1500 au, produces only very slightly shallower velocity profiles than the Keplerian curves shown in Fig. 3.1.2 and does not reduce the residuals.

In summary, the PV diagram of $CS(D)$ agrees well with the earlier observations of $C^{17}O$ and is compatible with the previously suggested circumstellar disc model in nearly-Keplerian rotation. The $C^{34}S$ data favours a somewhat shallower velocity profile, but also exhibits the largest scatter in the position of data points. For a central object of $6\text{--}10 M_\odot$, the PV diagrams suggest a disc inclination of about 30° (with 1σ limits of $0^\circ \dots 45^\circ$).

3.2. Description of the radiative transfer modelling programs

In order to deduce constraints for the physical properties of the material around AFGL490 from the observed spectra, the 2D radiative transfer code URANIA (Pavlyuchenkov et al. 2007) was employed to calculate the molecular emission and generate synthetic spectra from different physical models of a circumstellar disc. The programs used and/or written for this purpose are described in the following sections.

3.2.1 Protoplanetary disc model - general approach

The basis for the physical structure of the protoplanetary disc is a Fortran code provided by Y. Pavlyuchenkov, which calculates the temperature and density structure of a simplified geometrically thin protoplanetary disc model (Pavlyuchenkov 2009, private communication); it is described in the following section while modifications made to the code for the use in this work are introduced in sections 3.2.2 and 3.2.3.

The disc is axisymmetric regarding its rotation axis and symmetric about the disc midplane, therefore only the upper half of a cut in the radial direction is considered for the calculation. The disc is split into thin rings, the vertical structure of which is calculated independent of the neighbouring rings (sometimes referred to as “1+1D approach”). Gas and dust are assumed to be well mixed with a mass ratio of 100 : 1. The surface density distribution of the disc (i.e. surface density integrated in the z -direction) in the radial direction is fixed and described by a power law,

$$\Sigma_0(R) = \Sigma_r \times (R/R_r)^p \quad , \quad (3.3)$$

where R is the radial distance from the star and Σ_r the surface density at the reference radius R_r . The temperature and density structure are calculated under the assumption of a thermal and hydrostatical equilibrium in the vertical direction. In a first step, a grid (in cylindrical coordinates) adapted to the density gradients of the disc is constructed: in the radial direction the grid points are spaced logarithmically. For the vertical direction the structure of an isothermal disc, i.e.

$$\rho(z) = \rho_0 \times e^{-z^2/h^2} \quad , \quad (3.4)$$

with ρ_0 the density at the midplane and the pressure scale height

$$h = \sqrt{\frac{2kTR^3}{\mu m_H GM_\star}} \quad , \quad (3.5)$$

where T is a representative temperature of the disc, is used as an approximation for the real disc density structure. The vertical grid points are chosen such that their spacing is

uniform in $\ln(z)$ in an isothermal disc. Since $\Sigma(z) = \int_0^z \rho(z') dz'$, each grid point i at a certain vertical height z_i of the isothermal disc corresponds to a surface density Σ_i . For the structure of the non-isothermal disc, the same Σ_i are used, but the corresponding z will be different from that of the isothermal disc. In a second step, the actual temperature at each of these grid points is calculated by balancing the heating, which is assumed to occur through absorption of short-wavelength radiation from the central star and by accretion through the disc, and cooling of the disc, which is assumed to occur through thermal infrared emission of the disc dust. The local heating per unit mass as a function of surface density is denoted by $S(\Sigma) = dF/d\Sigma$ (where F is the flux). In general, it is given by the sum of heating due to accretion (under the assumption that the release of gravitational energy is proportional to the density) and stellar irradiation (under neglect of scattering):

$$S(\Sigma) = S_{\text{accr}} + S_{\star} = \frac{G\dot{M}M_{\star}}{4\pi\Sigma_0 R^3} + \frac{L_{\star}}{4\pi R^2} f \kappa_{\text{uv}} e^{-\kappa_{\text{uv}}(\Sigma_0 - \Sigma)} \quad (3.6)$$

In this approach, a fraction f (which can be a function of radial distance from the star) of the incident stellar radiation is penetrated into the disc (which can be estimated as half of the fraction of the stellar flux which travels normal to the disc surface, i.e. $f \approx 0.5\alpha$) and its extinction is approximated by the vertical optical depth. Furthermore, the grey approximation is applied, i.e. an average of the in general wavelength-dependent (dust) absorption coefficients is used. Only two absorption coefficients with values representative for the UV (κ_{uv}) and IR (κ_{IR}) part of the radiation field are used, because the dust of the disc emits practically only at wavelengths corresponding to typical disc temperatures (e.g. D'Alessio et al. 1998), which is much lower than the stellar temperature, and therefore allows to treat UV (stellar irradiation) and IR radiation (disc) field separately.

The vertical radiative transfer of the IR part of the radiation field in the thin disc is described in the plane parallel approximation, scattering is ignored, and the Eddington approximation is used, i.e. the 2nd moment of the radiation field K is equal to one third of the mean intensity J for an isotropic radiation field (see e.g. Paraiah 2002). After integrating over frequency, the following moment equations result:

$$H = -\frac{1}{3\kappa_R} \frac{dJ}{d\Sigma} \quad (3.7)$$

$$\frac{dH}{d\Sigma} = \kappa_P (B - J) \quad (3.8)$$

where H is the 1st moment (Eddington flux) of the radiation field, $B = \sigma T^4/\pi$ the (frequency integrated) Planck function, κ_R and κ_P the Rosseland and Planck mean opacity, respectively (scattering is ignored), and Σ is the surface density ($d\Sigma = \rho dz$, where z is the vertical coordinate axis and ρ the density). Boundary conditions are, that the net flux

at the disc midplane is zero due to the symmetry ($H(0) = 0$), and at the disc surface the Eddington flux equals half of the mean intensity: $H(\Sigma_0) = J(\Sigma_0)/2$. Energy conservation implies that the change of the Eddington flux arises from the heating:

$$\frac{dH}{d\Sigma} = \frac{S(\Sigma)}{4\pi} . \quad (3.9)$$

Under the assumption of local thermodynamic equilibrium (LTE), the temperature at each surface density Σ follows from equation 3.8:

$$T(\Sigma) = \sqrt[4]{\frac{\pi}{\sigma} \left[\frac{S(\Sigma)}{4\pi \kappa_P} - J(\Sigma) \right]} . \quad (3.10)$$

With the integration of equations 3.9 and 3.7, the mean intensity $J(\Sigma)$ at each point can be calculated, and together with the boundary conditions, the temperature only as a function of the heating $S(\Sigma)$ can be written as:

$$T(\Sigma)^4 = \frac{1}{4\sigma} \left[\frac{S(\Sigma)}{\kappa_P} + 2 \int_0^{\Sigma_0} S(\Sigma') d\Sigma' + 3\kappa_R \int_{\Sigma}^{\Sigma_0} \int_0^{\Sigma'} S(\Sigma'') d\Sigma'' d\Sigma' \right] . \quad (3.11)$$

Therefore, if the heating $S(\Sigma)$ consists of a sum of several heating functions, the $T^4(\Sigma)$ for each summand according to equation 3.11 can be added up to yield the final temperature.

From the now known temperature and surface density at each vertical grid point, the density ρ and height above the disc midplane z can be obtained by numerical integration of the equation for hydrostatic equilibrium in the vertical direction of the geometrically thin disc. Starting with a guess value for the density at the midplane ρ_0 , e.g. several times the midplane density of the isothermal disc, z and ρ for the i th grid point are calculated by:

$$\begin{aligned} z_i &= z_{i-1} + \frac{\Sigma_i - \Sigma_{i-1}}{\rho_{i-1}} , \\ \rho_i &= \left(c_{s,i-1}^2 \cdot \rho_{i-1} - \frac{GM_*}{R^3} (\Sigma_i - \Sigma_{i-1}) \cdot z_i \right) / c_{s,i}^2 , \end{aligned} \quad (3.12)$$

where $c_{s,i} = \sqrt{kT_i/\mu m_H}$ is the local sound speed. An iterative procedure uses the bisection method to find an appropriate value of ρ_0 , for which the density $\rho(\Sigma_0)$ at the outer edge of the disc equals the external density (e.g. of the surrounding cloud or interstellar medium). Then, with $T(\Sigma)$, $\rho(\Sigma)$ and $z(\Sigma)$, the disc structure is known as a function of z .

3.2.2 Opacities

In a mixture of gas and dust, i.e. below the dust evaporation temperature of about 1500 K, the dust is the dominating opacity source (e.g. Semenov et al. 2003) for not too hot central stars (ionization of gas by short-wavelength radiation was shown to influence the opacity only

for stars with effective temperature ≥ 20000 K, see Ercolano et al. 2012). The dust opacities depend on various parameters like chemical composition, size and structure (spherical shape, porous grains, aggregates, layered, heterogenous, or homogenous composition) of the dust particles. In general, all these parameters certainly vary with position inside the disc, evolution of the disc, initial chemical composition of the cloud etc. (e.g. dust sedimentation, chemical processes). In the model used here, the dust properties are only used to determine a temperature and density structure for the disc, which is then also assumed for the gas. Therefore, for the following calculations the dust opacities for protoplanetary discs from Semenov et al. (2003) are used, which consider a distribution of dust grains up to $5 \mu\text{m}$ size, where dust, organics and water ice constitute about 1.4% of the complete (dust plus gas) mass, and take into account e.g. the disappearance of ice around 160 K, of volatile organics above ca. 275 K, and destruction of all dust above 1500 K. Their dust opacities (per unit gas-plus-dust mass) for a standard (intermediate iron abundance, “NRM”) dust model with homogenous dust aggregates are applied, i.e. not simple spherical dust grains but dust particles consisting of many small subgrains, which might be a realistic representation of the grain structure in protoplanetary discs. It should be noted that the opacities of Semenov et al. (2003) for porous dust particles – a dust structure which might also be realistic – are about three times higher than those of homogeneous aggregates, which would lead to a significantly warmer surface layer of the disc. With the available tables of κ_ν as a function of wavelength for different temperature regions, the mean Planck opacity κ_P and mean Rosseland opacity κ_R (see e.g. Krügel 2008) are computed:

$$\kappa_P(T_1, T_2) = \frac{\int \kappa_\nu(T_1) B_\nu(T_2) d\nu}{\int B_\nu(T_2) d\nu} \quad , \quad \kappa_R^{-1}(T_1, T_2) = \frac{\pi}{4\sigma T_2^3} \int \frac{\partial B_\nu(T_2)}{\partial T_2} \kappa_\nu^{-1}(T_1) d\nu \quad . \quad (3.13)$$

Here T_1 denotes the temperature of the absorbing material (the dust), while T_2 is the characteristic temperature of the Planck function B_ν , with which the monochromatic opacity κ_ν is weighted before evaluating the mean. The opacity describing the attenuation of the incident stellar light is taken to be $\kappa_{UV} = \kappa_P(T, T_\star)$, and the opacity describing the transfer of the disc (IR) radiation field is $\kappa_{IR} = \kappa_R(T, T)$, where T is the local disc temperature - in practice the temperature at the disc surface at the given radius of the disc from the preceding iteration run is used.

As has been shown in Semenov et al. (2003), the dust opacities vary up to a factor of a few between different models in the literature; therefore in a comparison with other studies computing the structure of a protoplanetary disc, moderate differences to the temperature of the model presented here are expected.

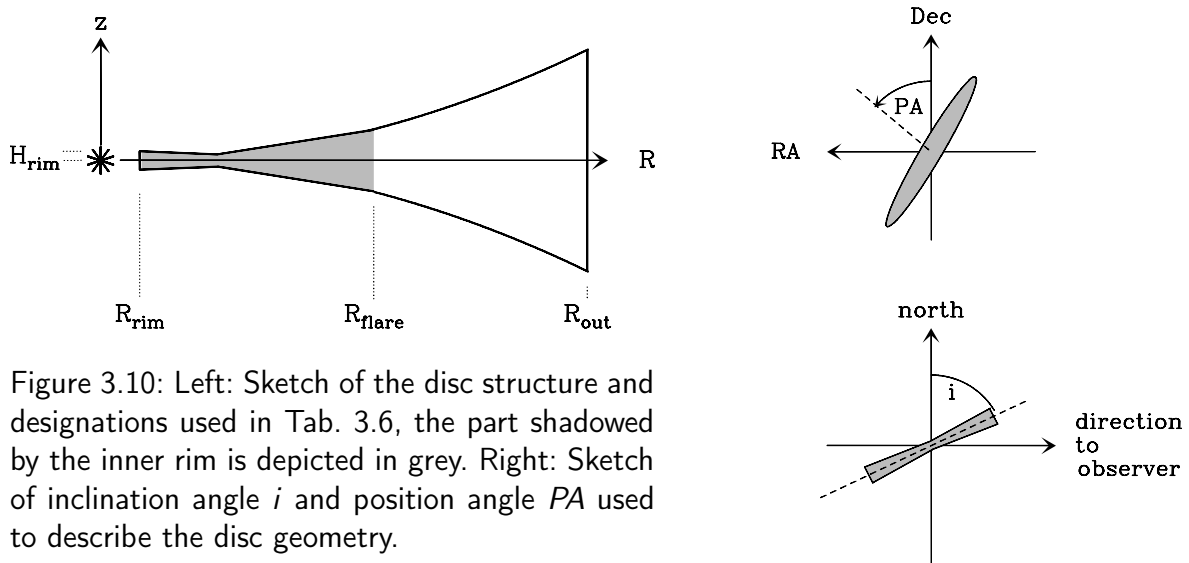


Figure 3.10: Left: Sketch of the disc structure and designations used in Tab. 3.6, the part shadowed by the inner rim is depicted in grey. Right: Sketch of inclination angle i and position angle PA used to describe the disc geometry.

3.2.3 Refined model with puffed-up inner rim and disc shadowing

In a second step, the basic code was modified as to include the model of a disc with inner hole and puffed-up inner rim published by Dullemond et al. (2001). The motivation for this approach are debates in the literature about the inclination angle of the AFGL 490 disc, where molecular line observations favour a moderately inclined disc, while the non-detection of direct light from the central source was interpreted as sign of obscuration (Hodapp 1984) which would point to a higher inclination if the disc was geometrically thin. The model of Dullemond et al. (2001) takes into account that the inner rim of the disc, which is heated by stellar radiation under an angle of 90° to a temperature close to the dust evaporation temperature (ca. 1500 K), has an large scale height (is “puffed-up”) compared to the outer parts of the disc, onto which the starlight impinges with a small angle, and can therefore shadow parts of the disc directly behind the rim. In addition to the stellar irradiation, the disc is heated through irradiation by the inner rim (“self irradiation” of the disc). Moreover, an inner rim with increased scale height could block direct starlight from an observer for a wider range of disc inclinations than a standard flared disc. In the parts of the disc, which are shadowed from both irradiation sources by the puffed-up inner rim, the heating is assumed to occur mainly through radiative diffusion from the unshadowed parts and the approximative expressions for its effect given by Dullemond et al. (2001) are used. The main difference of the approach used in this work to the model of Dullemond et al. (2001) is, that the vertical structure of the disc is not split up into an isothermal surface and inner disc layer, instead the temperature is calculated directly from the heating/cooling balance as a function of the surface density for each vertical point, and the density structure is then determined as in the initial code described above (equations 3.7 to 3.12). Therefore, the temperature varies smoothly from the surface to the midplane As was shown by Dullemond et al. (2002), the moment

equations with a fixed Eddington factor of $\frac{1}{3}$ and grey opacities yield somewhat different disc structures than a full radiative transfer treatment or moment equations with Eddington approximation but full frequency-dependent opacities. Specifically, the method with grey opacities yields somewhat different temperatures at the disc midplane and the temperature rise towards the disc surface is more steep than in the full radiative transfer treatment. Nevertheless, the grey opacities are used because of the more simple implementation and faster model calculations. Moreover, the dust opacities and therefore temperatures may vary substantially as a function of grain size distribution and chemical composition, are difficult to constrain for a particular object, and therefore introduce considerable uncertainties in the temperature structure.

It should be pointed out that later publications treat the structure of the inner rim in a more detailed way (e.g. Isella & Natta 2005; Tannirkulam et al. 2007; Kama et al. 2009), including the dependence of the dust evaporation temperature on the grain chemical composition and density, as well as dust growth and settling, which lead to a curved rim structure instead of the vertical “wall” assumed in Dullemond et al. (2001). Although the exact structure of the rim is of great importance for models of the NIR dust emission and resulting SEDs which was also the main goal of most aforementioned publications, this work in contrast uses the dust temperature and density structure only as “matrix” for the gas distribution. Therefore, the simplification of a vertical inner rim is acceptable for us, its main effect may be the overestimation of the disc’s “self-irradiation” by the inner rim and possibly an overestimation of the extent of the shadowed region (which depends strongly on dust opacities, however). Kama et al. (2009) also showed that the simplified approach of Dullemond et al. (2001) underestimates the temperature in the shadowed region of the disc. Controversial discussions of the existence of the hot inner rim do exist as well (Vinković et al. 2006).

The detailed setup of the refined code is described in the following. Fixed input parameters are the properties of the central star (temperature T_* , luminosity L_* , mass M_*), the maximum radial extent of the disc R_{out} , disc mass M_{disc} , mass accretion rate \dot{M} and the power-law index of the surface density p in $\Sigma_0(R) = \Sigma_{\text{rim}} \times (R/R_{\text{rim}})^p$. The scaling of the surface density (note that it is defined as the integral only over the upper half of the disc in contrast to most of the literature) is computed from the inner disc rim R_{rim} and the disc mass (for $p \neq -2$):

$$\Sigma_{\text{rim}} = M_{\text{disc}} \frac{p+2}{4\pi} \left[R_{\text{out}}^2 \left(\frac{R_{\text{out}}}{R_{\text{rim}}} \right)^p - R_{\text{rim}}^2 \right]^{-1}. \quad (3.14)$$

First, the location of the inner rim of the disc R_{rim} is calculated as the radius where the stellar radiation impinging vertically onto the rim heats it to the dust evaporation temperature

T_{rim} , which is set to 1500 K. The procedure described in Dullemond et al. (2001) is used:

$$R_{\text{rim}} = \sqrt{\frac{L_{\star}}{4\pi\sigma T_{\text{rim}}^4} \left(1 + \frac{H_{\text{rim}}}{R_{\text{rim}}}\right)}, \quad (3.15)$$

where $H_{\text{rim}} = \chi_{\text{rim}} h_{\text{rim}}$ is the (photosphere) vertical height of the inner rim, which equals a dimensionless factor χ_{rim} times the pressure scale height $h_{\text{rim}} = h(R_{\text{rim}})$ (equation 3.5). The factor $(1 + H_{\text{rim}}/R_{\text{rim}})$ represents an approximation for the self-irradiation, i.e. the additional heating of the inner rim by the rim's radiation. As a first guess for R_{rim} , the self-irradiation is neglected. Then, the χ_{rim} satisfying the equation

$$\text{erf}(\chi_{\text{rim}}) = \int_0^{\chi_{\text{rim}}} e^{-x^2} dx = 1 - \frac{1}{8\kappa_{\text{uv}}\Sigma_{0,\text{rim}}} \quad (3.16)$$

is calculated by a simple bisection procedure (here the approximation of Dullemond et al. (2001) is used, who assumed that the vertical optical depth at the location of the rim is roughly eight times the radial optical depth; factors χ_{rim} instead of $\chi_{\text{rim}}/\sqrt{2}$ and 8 instead of 4 compared to Dullemond et al. 2001 in the above equation arise from the different definition of h and Σ_0 used in this work). Here the dust opacity $\kappa_{\text{uv}} = \kappa_{\text{P}}(T_{\text{rim}}, T_{\star})$ is calculated as described in section 3.2.2. The corresponding H_{rim} is then used with equation 3.15 to calculate a new value of R_{rim} . The procedure is iterated until convergence is reached, where Σ_{rim} is updated with equation 3.14 in each step.

With R_{rim} , H_{rim} determined and Σ_{rim} fixed, a grid of points for an isothermal disc as described in section 3.2.1 is constructed. One hundred grid points are used for the disc in the radial and vertical direction, plus 50 additional points in the vertical direction above the disc and 10 radial points inside the dust destruction radius R_{rim} .

The structure of a flared disc without shadow is constructed next. The heating function in this refined model is the sum of accretion heating S_{accr} , stellar irradiation S_{\star} and irradiation by the hot inner rim S_{rim} . For the stellar irradiation, starlight is assumed to penetrate on a radial ray into the disc, and therefore reaches the height z above the midplane corresponding to a surface density Σ after being extinguished over the optical depth $\tau = \kappa_{\text{uv}}(\Sigma_0 - \Sigma)/\alpha$:

$$S_{\star} = \frac{L_{\star}}{4\pi R^2} \kappa_{\text{uv}} \cdot e^{-\kappa_{\text{uv}}(\Sigma_0 - \Sigma)/\alpha} \quad (3.17)$$

Sometimes this function is divided by 2, if only half of the star is assumed to be visible from any location in the disc (e.g. Inoue et al. 2009). For the irradiation by the hot inner rim,

the near-field limit for the flux of the rim given by Dullemond et al. (2001) is adopted:

$$S_{\text{rim}} = \sigma T_{\text{rim}}^4 \left(\frac{R_{\text{rim}}}{R} \right)^2 \kappa_{\text{rim}} e^{-\kappa_{\text{rim}}(\Sigma_0 - \Sigma)/\alpha} \cos \theta_1 \begin{cases} \frac{2}{\pi}(\theta_2 \sqrt{1 - \theta_2} + \arcsin \theta_2), & \text{if } 0 < \theta_2 < 1 \\ 1, & \text{if } \theta_2 > 1 \end{cases} \quad (3.18)$$

with:

$$\theta_1 = \arctan \frac{R - R_{\text{rim}}}{H_{\text{ph}} - H_{\text{rim}}}, \quad \theta_2 = \frac{R/R_{\text{rim}} - 1}{H_{\text{ph}}/H_{\text{rim}} - 1}.$$

Here $\kappa_{\text{rim}} = \kappa_P(T(R, z), T_{\text{rim}})$ is the dust opacity for the radiation from the hot rim, $H_{\text{phot}}(R)$ is the photosphere height of the disc, i.e. the height z above the midplane where the grazing optical depth is $\tau = \kappa_{\text{uv}}(\Sigma_0 - \Sigma(z))/\alpha = 1$ (the incident angle is assumed to be approximately the same as the one of the incident stellar light). $\theta_2 < 1$ corresponds to the case that the whole inner rim at the opposite side of the star is visible at the particular location (R, z) of the disc, while for $\theta_2 > 1$ part of the opposite rim is hidden behind the near side of the inner rim.

With the moment equations and boundary conditions, Eddington and grey approximation as described in section 3.2.1, the local dust temperature at each point (R, z) is then given by:

$$\begin{aligned} T^4(R, \Sigma) = & \frac{\alpha}{4\sigma} \frac{L_*}{4\pi R^2} \left[\left(\frac{\kappa_{\text{uv}}}{\alpha \kappa_{\text{IR}}} - \frac{3\alpha \kappa_{\text{IR}}}{\kappa_{\text{uv}}} \right) e^{\kappa_{\text{uv}}(\Sigma - \Sigma_0)/\alpha} + \left(2 + \frac{3\alpha \kappa_{\text{IR}}}{\kappa_{\text{uv}}} \right) \right. \\ & \left. - (3\kappa_{\text{IR}}(\Sigma_0 - \Sigma) + 2) e^{-\kappa_{\text{uv}}\Sigma_0/\alpha} \right] \\ & + \frac{\alpha T_{\text{rim}}^4 \cos \theta_1 f(\theta_2)}{4} \left(\frac{R_{\text{rim}}}{R} \right)^2 \left[\left(\frac{\kappa_{\text{rim}}}{\alpha \kappa_{\text{IR}}} - \frac{3\alpha \kappa_{\text{IR}}}{\kappa_{\text{rim}}} \right) e^{\kappa_{\text{rim}}(\Sigma - \Sigma_0)/\alpha} \right. \\ & \left. + \left(2 + \frac{3\alpha \kappa_{\text{IR}}}{\kappa_{\text{rim}}} \right) - (3\kappa_{\text{IR}}(\Sigma_0 - \Sigma) + 2) e^{-\kappa_{\text{rim}}\Sigma_0/\alpha} \right] \\ & + \frac{\dot{M}}{4\sigma} \left(\frac{1}{\kappa_{\text{IR}}} + 2\Sigma_0 + \frac{3\kappa_{\text{IR}}}{2} (\Sigma_0^2 - \Sigma^2) \right), \end{aligned} \quad (3.19)$$

where the two cases of the last term in equation 3.18 are abbreviated with $f(\theta_2)$, and the last term of equation 3.19 describes the heating due to accretion. Considering only the stellar irradiation, the surface ($\Sigma = \Sigma_0$) and midplane ($\Sigma = 0$) temperatures of the disc are:

$$T^4(\Sigma_0) \approx T_*^4 \left(\frac{R_*}{R} \right)^2 \frac{\kappa_{\text{uv}}}{4\kappa_{\text{IR}}}, \quad T^4(0) \approx T_*^4 \left(\frac{R_*}{R} \right)^2 \frac{\alpha}{2}, \quad (3.20)$$

i.e. the midplane temperature depends primarily on the angle α of the incident starlight – hence the fraction of starlight penetrated into the disc because of the disc geometry – and the surface temperature mainly on the ratio of UV to IR opacity of the dust – the efficiency of the dust to absorb short-wavelength stellar light compared to the IR radiation of the disc itself.

In the first pass of the iteration, the incident angle of the starlight with respect to the disc surface α is set to 0.05 (although the disc structure converges quickly independent of the initial value of α). After the temperature and density structure has been evaluated (equations 3.19 and 3.12), the photosphere height H_{ph} for each radius is determined. The

incident angle of starlight is

$$\alpha = \frac{d \ln (H_{\text{ph}}/R)}{d \ln R} \frac{H_{\text{ph}}}{R} \quad (3.21)$$

and varies slowly with radius. To avoid numerical instabilities, a power-law function is fitted to the photospheric height divided by radius ($H_{\text{ph}}/R = a R^b$, where a and b are the fit parameters) for several neighbouring points (typically 10–15). The incident angle is then determined from this piecewise fit: $\alpha = a b R^b$, and H_{ph} replaced by the fitted photosphere height to obtain a smoother distribution. These values are used for the next iteration; the structure of the flared disc alone (without shadow) is found to converge typically within 5 iterations.

In Fig. 3.11, an example of the resulting vertical temperature structure is shown, taking the same low-mass star–disc system as in Dullemond et al. (2002). The comparison with their results – the temperature structure from their momentum equation calculations with mean opacities, i.e. similar to the approach used here, are denoted by dashed lines – shows that the code used in this work produces higher surface temperatures at distances < 20 au from the star.

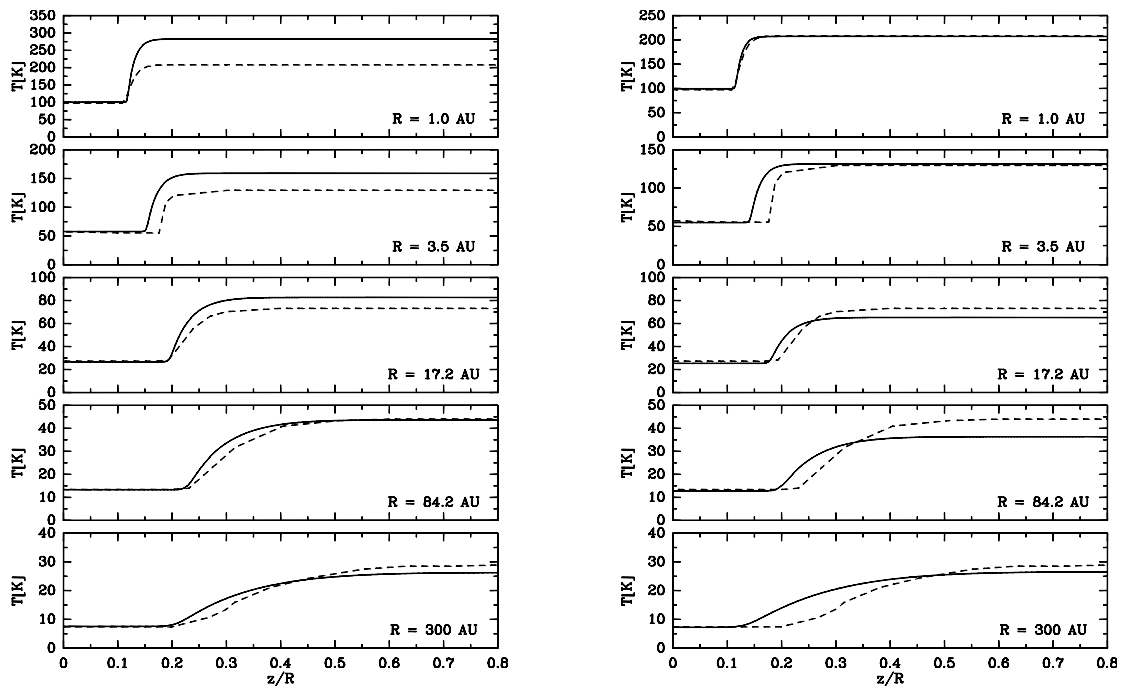


Figure 3.11: Vertical temperature structure at different distances from the star for a disc as in Dullemond et al. (2002), i.e. with $\Sigma_0 = 500 \text{ g cm}^{-2} (R/1 \text{ au})^{-1}$ around a $0.5 M_{\odot}$ star with $T_{\star} = 3000 \text{ K}$. The dashed lines show the result of the momentum equation approach of Dullemond et al. (2002), the solid lines the temperature resulting from the code used in this work. On the left side, the result using opacities as described in section 3.2.2 are shown, on the right side, κ_{UV} is scaled down by a factor of 3.

This is most likely the result of different dust opacities used (cf. equation 3.20): in the right part of the figure the same model is shown, but with UV opacities reduced by a factor

of three. This yields much better agreement with the results of Dullemond et al. (2002), although the photosphere height (the region where the temperature changes from its mid-plane value to the surface temperature) of the model from this work is still somewhat higher.

In the next step, the shadowed region $R_{\text{rim}} < R < R_{\text{flare}}$ is cut out and treated separately. Here, following Dullemond et al. (2001), $R_{\text{flare}} = R_{\text{rim}} \cdot H_{\text{rim}}/H_{\text{ph}}(R_{\text{flare}})$ is the radius at which the normally flared disc reaches a photosphere height which is high enough to not be in the shadow of the puffed-up inner rim. For $R \geq R_{\text{flare}}$, the structure of the normally flared disc is kept without modification. In the shadowed part, the stellar heating S_{\star} is absent, irradiation by the hot inner rim S_{rim} is possible in some parts, and in addition there is heating by radial radiative diffusion from the inner rim and outer flared part S_{dif} . For the radial radiative diffusion, the approximation given in Dullemond et al. (2001) is used. In a simple treatment, the disc height directly behind the rim and in absence of other heating sources, and the disc height due to radial diffusion from the radius R_{flare} , where the disc starts to flare again, are calculated by the following equations. Here it is assumed that the radial points are numbered by j , where the first point is R_{rim} , and the last R_{flare} . For the points in between, the radial diffusion from the inner rim causes a disc height:

$$H_j^{\text{rim}} = R_j \left(\frac{H_{j-1}^{\text{rim}}}{R_{j-1}} + \frac{3H_{j-1}^{\text{rim}}/R_{j-1} - 1}{8R_{j-1}} (R_j - R_{j-1}) \right) , \quad (3.22)$$

and from the flaring radius a disc height:

$$H_j^{\text{flare}} = R_j \left(\frac{H_{j+1}^{\text{flare}}}{R_{j+1}} - \frac{3H_{j+1}^{\text{flare}}/R_{j+1} - 1}{8R_{j+1}} (R_j - R_{j+1}) \right) . \quad (3.23)$$

At each radial point R_j , the disc height H_{dif} is considered to be the larger one of H^{rim} and H^{flare} . In a very rough approximation, to the local kinetic temperature in the shadowed part the temperature which alone in an isothermal disc would cause the disc height H_{dif} , is added:

$$T(R, \Sigma)^4 = \frac{\pi}{\sigma} \left(\frac{S_{\text{rim}}(\Sigma)}{4\pi \kappa_{\text{IR}}} - J(\Sigma) \right) + \left(\frac{\mu m_H G M_{\star}}{2kR^3} \frac{H_{\text{dif}}^2}{\chi_{\text{rim}}^2} \right)^4 . \quad (3.24)$$

The density is again reconstructed using equation 3.12. Here, the temperature and density of the shadowed part is calculated in three passes: a first one with only the radial radiative diffusion from inner rim and flaring part as heating, and a second one including radial radiative diffusion and heating by irradiation from the rim S_{rim} (because it needs a photosphere height to not equal zero) with a fixed value of the incident angle α , and a third pass with radial radiative diffusion and rim irradiation where the incident angle α was determined from the photosphere height of the second pass like described for the flared disc part.

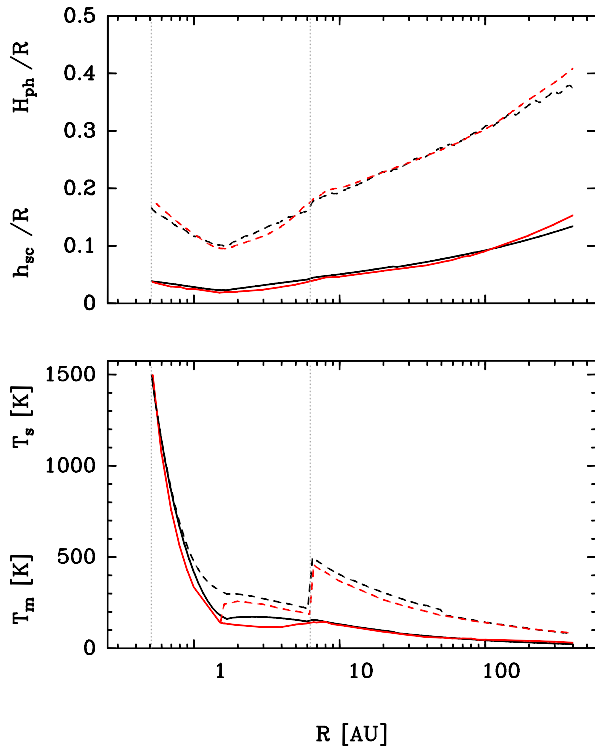


Figure 3.12: Radial disc height and temperature profiles for a disc as in Dullemond et al. (2001), i.e. with $\Sigma_0 = 1000 \text{ g cm}^{-2} (R/1 \text{ au})^{-1.5}$ around a $2.4 M_\odot$ star with $T_\star = 9500 \text{ K}$. The upper plots show the disc photosphere height (H_{ph} , dashed lines) and pressure scale height (h , solid lines). The lower plot shows the disc surface temperature (T_s , dashed lines) and temperature at the midplane (T_m , solid lines). In each panel, red lines denote the results of Dullemond et al. (2001), while black lines show the result of the code described in this work. Gray dotted vertical lines denote the location of the inner rim (close to 0.5 au) and the radius R_{flare} where the disc starts to flare again.

For comparison, the radial structure of the disc height (photospheric and pressure scale) and disc temperature at surface and midplane is shown in Fig. 3.12 for the same parameters of an intermediate-mass star–disc system as in Dullemond et al. (2001), with their results in red and the calculations from the code used in this work shown in black. All curves start at the inner rim of the disc (about 0.5 au for the model case, left vertical dotted line). Directly behind the rim the disc is shadowed and heated only by radial radiative diffusion, which results in a rapid decline of the temperature. The outer region of this shadowed part can be partially illuminated and heated by irradiation from the opposite inner rim, which is visible as an increase of the disc surface temperature above the midplane temperature. In the model calculations considered here, this heating by rim irradiation sets in already at a smaller radius than in Dullemond et al. (2001), possibly a result of the different opacities or the different numerical procedure used. At even larger radii the disc reaches out of the shadow and starts to flare again (ca. 6 au, right vertical dotted line), the illumination by starlight causes a sudden increase of the disc surface temperature. Keeping the different opacity model in mind, which affects the absorption of star light and rim radiation and therefore the value of temperature in the disc surface (consequently also the disc surface height), the deviations between the model calculation of this work and Dullemond et al. (2001) seem acceptable, and the overall structure of the disc is in reasonable agreement with Dullemond et al. (2001).

Finally, the density at $R < R_{\text{rim}}$ is set to the external density (although gas may still exist

inside the dust destruction radius), and the temperature equal to that of the inner rim. This represents another simplification, since significant amounts of gas may still exist inside the dust destruction radius. The material within the disc is given the Keplerian velocity corresponding to its distance from the central star (self-gravity of the disc ignored).

As mentioned before, the gas temperature is assumed to be equal to the dust temperature, and the gas density distribution in the radial direction was fixed by the disc mass and power-law index of the surface density distribution as input parameters. The specific molecular species, the line emission of which is to be modelled, are assumed to be homogeneously distributed in the disc, i.e. the spatial distribution of their number density is equal to the one of molecular hydrogen H_2 multiplied by the fractional abundance X_{mol} listed in Tab. 2.2 and described in section 3.3. However, for discs around low-mass stars significant depletion of molecules up to two orders of magnitude below the values typical for dark clouds have been observed (Dutrey et al. 1997). Therefore, the fractional molecular abundances assumed have to be considered as a first guess and may differ substantially in reality. For CH_3OH , fractional abundances from 10^{-9} in cold dark clouds up to 10^{-6} in hot cores are known to occur (Leurini et al. 2004). Moreover, the molecular spatial distribution will depend on chemical processes leading to their formation and destruction, and will be a function of evolution time. Since these are complex to model, the freeze-out of molecules in very cold parts of the disc is taken into account only approximately: the molecule fractional abundance is set to zero in parts of the disc where the local temperature drops below the typical freeze-out temperatures (10 K for $C^{17}O$, 20 K for $C^{34}S$). As a note of caution, CO has also been observed in regions of circumstellar discs colder than the freeze-out temperature (Dutrey et al. 2007).

3.2.4 Synthetic spectra - radiative transfer with URANIA

A 2009 version of the 2D line radiative transfer code URAN(IA) was then employed to synthesize the molecular line emission for the physical input model. A detailed description of the algorithms used in the URANIA package can be found in Pavlyuchenkov & Shustov (2004) and Pavlyuchenkov et al. (2007); in the following, only a brief outline of the general scheme will be given:

The disc physical model, which was described on a grid in cylindrical coordinates because of its symmetries, is transformed onto a two-dimensional grid in spherical coordinates with points uniformly spaced in the radial and polar angle direction (achieved by interpolation, i.e. the physical parameters at each spherical-grid point are the weighted mean of the parameters of all surrounding disc-adapted grid points, weighted by the inverse of the distance between these points to the power of four). Afterwards, the physical domain of interest is split into cells, within which the physical parameters defined from the input model are assumed to be constant. For the desired molecule and transition, initial level populations are set for each cell. In an iterative procedure, sets of random photon

directions through the grid of cells at random frequencies infalling on each cell are chosen by a Monte Carlo algorithm. Line intensities for each cell and frequency are calculated by direct integration of the equation of radiative transfer (over subintervals smaller than the cellsize) along all photon rays. The resulting averaged mean intensities in each cell are then used to calculate refined level populations. Several approximate molecular line radiative transfer methods (e.g. local thermodynamical equilibrium LTE, full escape probability FEP, large velocity gradient LVG) are available, which are described in detail in Pavlyuchenkov et al. (2007). Following their conclusion that the LVG method provides good balance between agreement with exact Monte Carlo codes (ART) and computation time for a wide range of molecules and transitions, this method is employed. The large velocity gradient method uses the fact, that in the rotating Keplerian disc the velocity gradients in most directions are larger than the local thermal and microturbulent velocities, so that a photon emitted from a certain disc region can be absorbed only in a small part of the disc where the velocity shift to the emitting cell is smaller than the typical linewidth of the transition. Considering only the regions which are “radiatively coupled” allows to speed up the computation compared to a full radiative transfer treatment.

From the level populations computed by the radiative transfer code URAN, synthetic spectra can be produced with the package URANIA, where a map of raw spectra for a given source distance, position angle, disc inclination, velocity resolution, velocity range and spacing of map points is calculated. In principle, these raw maps can be convolved with the same telescope beam as the observations, and the difference between synthetic and observed spectra be evaluated to find the model in best agreement with observations. However, to evaluate the goodness of fit between the modeled disc spectra and observations, the commonly used and appropriate approach is to examine the difference between modeled and observed visibilities in the uv plane (e.g., Guilloteau & Dutrey 1998), since the evaluation in the image plane may suffer from inaccuracies introduced by the imaging process.

Therefore, for each disc model and parameter set, maps for each velocity channels are created without convolution with a beam (i.e. raw maps), and model uv visibilities¹ are calculated from these raw image cubes using the same uv coverage and telescope parameters as used in the observations. Similar to Guilloteau & Dutrey (1998), it is found that in velocity a spacing of the channels identical to that of the observations, and in the spatial directions a pixel size of several times (ca. 8–10) smaller than the beam size is sufficient to obtain model uv visibilities which are not affected by too coarse structures of the model images. For $C^{17}O$, a channel width of 0.102 km/s and pixel size of 0.1'' are used.

¹Using standard GILDAS tasks.

The χ^2 is then calculated by summing the squared differences between model and observed real and imaginary parts of each uv visibility for all velocity channels, multiplied by the weight of the according uv visibility point (which is equivalent to $[\sigma^2 N_{\text{ch}} N_{\text{vis}}]^{-1}$ in the PdBI data sets):

$$\chi_w^2 = \sum_{j=1}^{N_{\text{vis}}} \sum_{i=1}^{N_{\text{ch}}} \left[(Re_{\text{mod}(i,j)} - Re_{\text{obs}(i,j)})^2 + (Im_{\text{mod}(i,j)} - Im_{\text{obs}(i,j)})^2 \right] \times w_j \quad . \quad (3.25)$$

i.e. χ_w^2 represents the square of the average deviation between observed and modeled visibilities in units of the variance per data point. Note that χ_w^2 is not identical to the commonly used “reduced” χ_{red}^2 ; the latter requires the knowledge of the degrees of freedom of the model, which is not possible for the model used here since the modeled intensities do not depend linearly on the model’s input parameters, and therefore the degrees of freedom are not allocable, and especially not necessarily identical to $N_{\text{ch}} \cdot N_{\text{vis}}$ (Andrae et al. 2010).

For the model calculations, it was also necessary to apply a fixed value for disc mass and fractional molecular abundance to minimize computational time. However, the molecular abundances are not precisely known and may vary considerably for protoplanetary discs depending on age, chemical processes and freeze-out onto dust grains. Furthermore, there is a degeneracy between disc mass and fractional molecular abundance, i.e. different combinations of both values may result in similar molecular emission patterns. Therefore, as a first approximation, a fixed disc (gas plus dust) mass and molecular abundance is used, and assumed that the intensity of the lines in the model spectra can be considered to scale linearly with the disc mass – since the molecules and transitions considered are mostly optically thin, the observed intensity scales linearly with the molecular content (for fixed molecular fractional abundance and if excitation conditions do not vary much), so that this approximate approach may be justified if the scaling factor is not more than a few. In addition, it is undesirable that the model spectra of discs around different central stars produce different likelihood of the models only because of different intensity (the best fit could require a different disc mass for the different central stars). Therefore, a multiplicative factor f is applied to the model uv visibilities (which also scale approximately linearly with the model line intensities), i.e. $f \cdot Re_{\text{obs}(i,j)}$ is used instead of $Re_{\text{obs}(i,j)}$, etc., in equation 3.25; and f is varied to find the smallest χ_w^2 , which corresponds to scaling the model spectra such, that their intensity fits best to that of the observed spectra. It turns out that for a disc mass of $1 M_{\odot}$ and the example of C^{17}O , typical scaling factors f are in the range of 0.1–2.5 (increasing both with inclination and central star luminosity).

3.2.5 Discs with inner holes

Discs with inner holes, i.e. inner holes larger than expected from the dust destruction radius, are widespread for low-mass circumstellar discs (e.g., Dutrey et al. 2008). It is not clear how

such an inner hole would have been created in a young massive disc, theoretical discussions (see section 1.1) favour accretion of disc material onto the star and/or photoevaporation as main disc dispersal mechanisms. In principal, the model of a shadowed disc as described above could be used with the inner rim increased artificially to larger values (several hundred au, as suggested by the molecular emission); then equation 3.15 can be inverted to calculate the temperature at this inner disc edge by assuming that it still exhibits a vertical surface to the star. It is however unclear if the inner edge will still have a puffed-up shape when it was created by an unknown disc dispersal mechanism. Moreover, for inner holes of ≥ 100 au, the disc surface height to radius ratio at the inner disc edge $H_{\text{ph}}/R_{\text{in}}$ is about one third, i.e. a puffed-up inner disc would be about two times higher and put the whole disc into shadow (see Appendix A.1), which is questionable. Also the approximative treatment of radial radiative diffusion (equation 3.22) fails for such high $H_{\text{rim}}/R_{\text{rim}}$ ratios.

A comparison of models for the example of C^{17}O with puffed-up inner rim and shadowing and such without a shadow (i.e. a normally flared disc with inner radius at the dust evaporation front is assumed) shows that synthetic spectra for identical star and disc parameters differ in flux, but do not vary significantly in the line shape. For C^{17}O and B type stars, the relative flux difference is $\leq 10\%$ for the majority of the disc (distance from central object ≤ 1200 au), but can be up to 100% in the outermost disc regions (ca. 1600 au; note that at these distances from the star the lines are several orders of magnitude weaker than at the disc center) at intermediate and high inclinations ($> 30^\circ$). For an A5 star, the model spectra of the shadowed disc show up to 40% higher flux throughout the whole disc, irrespective of inclination. This may result from the self-irradiation of the disc by the hot inner rim, since the ratio of rim to central star luminosity is highest for cool central stars. For C^{34}S spectra, the flux differences are about 10–20% for all central star spectral types and all positions across the disc (owing to the large beam of these observations).

The only slight differences are not surprising, if the spectral lines originate mainly from the disc regions close to the midplane, since the main effect of shadowing is to decrease the temperature in the disc surface layer, while the midplane temperature is – although lower than in the normal flared disc case – less affected. Due to limited space, it is referred to discussions of the details of molecular line excitation in protoplanetary discs in the literature (e.g., Pavlyuchenkov et al. 2007). But since the isotopes and transitions – except $\text{CS}(1-0)$ – considered in this work are optically thin, and the disc midplane temperatures never drop below 20 or 10 K, where significant freeze-out of the molecules can be expected (at least in the simple treatment ignoring chemical evolution of the discs considered in this work), it is probable that the emission stems mainly from inner disc parts.

3.3. Parameter space for the modelling runs

The input parameters characterizing the disc model and radiative transfer calculations are summarized in Tab. 3.5. Due to the number of free parameters, the not high signal-to-noise of the observations and computational time, no advanced sampling of the parameter space e.g. by Markov chains is employed, but rather coarse grids of parameters around the most reasonable values are explored, and some values are kept fixed for all models. Some of the modelling parameters can already be constrained from the intensity-integrated images and integrated spectra, as described in the following.

The centre of the disc is fixed at $\alpha = 03^h27^m38.80^s$, $\delta = 58^\circ47'00.24''$, the position of the continuum peak.

The position angle PA is estimated from the angle between the north direction and the long axis of the integrated disc emission of C¹⁷O in Fig. 3.6 ($\approx 26^\circ$), since positions angles of the lines connecting maxima of blue- and redshifted emission (Tab. 3.2) show a large scatter between the molecules; it is fixed at 30° for the modelling.

An estimate for the outer radius R_{out} of the disc is given by the maximal extent of the molecular emission. The disc could theoretically be larger, if the outer parts do not contribute significantly to the emission due to low density and temperature (i.e. insufficient conditions for excitation of line emission), and some uncertainty remains due to the relatively large beamsize of the observations. According to the extent of emission in the C³⁴S(2-1) and older C¹⁷O(2-1) observations, $R_{\text{out}} = 1500$ au is used as first estimate for the disc outer radius.

In general, the central velocity should be identical to the system velocity, which for AFGL 490 is usually assumed to be $v_{\text{LSR}} = -13.4$ km/s. However, to account for possible slight offsets, the central velocity is instead set to the value around which the blue- and redshifted line components are symmetric. For this purpose, the values obtained by approximation of the integrated spectra in Fig. 3.2 with two Gaussians of similar line width but different peak intensity and position (which is useful as a first estimate although the integrated line profiles are not really gaussian) are used, and the central velocity set to the middle between both line components.

Hints on the inner disc radius (more specifically, the inner radius where the molecules in question exist and are excited) may come from two observables. First, the velocity shift between blue- and redshifted lines constrains the inner disc radius for a given central star mass and disc inclination. Assuming Keplerian rotation (which will be the case for the following modelling), the circular velocity at the inner edge of the disc, viewed under an inclination angle i is given by:

$$v_{\text{in}} = 29.86 \text{ km/s} \sqrt{\frac{M_\star}{R_{\text{in}}}} \sin(i) \quad , \quad (3.26)$$

where M_* is taken in units of M_\odot and R_{in} in astronomical units. To reproduce the largest observed velocity shift between red- and blueshifted lines, for a model with fixed star mass and inclination, the inner radius R_{in} must be smaller or equal to the radius defined by equation 3.26 (where the observed shift equals $2 \cdot v_{\text{in}}$). A smaller velocity shift could be possible if the signal of the larger velocities in the spectrum of the disc is small compared to that of the outer material with lower velocity. Second, the spatial distribution of molecular emission may directly show a large inner hole of the disc through absence of emission close to the disc center, if the inclination is small (i.e. the disc viewed close to pole-on). However, the spatial resolution of the data sets except C^{17}O is too poor to expect constraints on the inner disc radius for an object like AFGL 490 at a distance of 1 kpc. For the beginning, an inner radius equal to the dust destruction radius is assumed.

As an estimate for the disc mass, following the values derived by Schreyer et al. (2006) from 1.3 mm dust continuum emission, $M_{\text{disc}} = 1.0 M_\odot$ is used as a first guess. It should be noted that different combinations of disc mass and molecular fractional abundance can yield the same amount of molecules in the disc and therefore comparable spectra. However, the molecular fractional abundance is more difficult to constrain than the disc mass, since the molecular content can vary through chemical processes during evolution of the disc. As a guess value, molecular fractional abundances (relative to H_2) typical for protoplanetary discs are used: 10^{-4} for CO, 10^{-8} for CS (Pavlyuchenkov et al. 2007), and – applying typical isotope ratios of the ISM (Muller et al. 2006, and references therein) – 4×10^{-8} for C^{17}O and 5×10^{-10} for C^{34}S are assumed.

The disc surface density index is assumed to be negative to ensure a surface density profile decreasing towards larger disc radii. It is also expected that the disc temperature does not increase with increasing distance from the central star; in a viscous stationary disc where temperature, surface density, inward radial velocity and viscosity are described by power laws of the distance to the central star, this requires $p \geq -1.5$, which is also a typical value applied for protoplanetary discs (e.g. Dutrey et al. 1997). On the other hand, Rice & Armitage (2009) showed that self-gravitating massive, marginally instable discs evolve to a steady-state with disc surface density index of $p \approx -2$. Therefore, disc surface density indices from $p = -0.5$ to -2.0 are considered here.

Since there is not much known about ongoing mass accretion, no accretion ($\dot{M} = 0$) is assumed for the time being. From equation 3.6 it also becomes clear that for typical values of accretion (of the order of $10^{-6} M_\odot/\text{yr}$), stellar mass to luminosity ratio (10^{-3} for B1 to 0.1 for A5), disc surface density and opacity, the heating due to accretion may reach ca. 15% of the heating provided by stellar illumination, but only for the innermost disc regions and least luminous stars. For stars of spectral type B, accretion as heating source is negligible in the assumed model.

The only constraints on the central star so far stem from its bolometric luminosity, which was compared with a B2–B3 ZAMS star; and fits of a rotating disc to the observed C^{17}O

emission by Schreyer et al. (2006), which suggest a stellar mass of 8–10 M_{\odot} . Therefore, for the first modelling run a range of spectral types from A5 to B1 are considered and construct disc models using the according stellar parameters of (Schmidt-Kaler 1982, see Tab. 3.6). These are main-sequence models, although AFGL 490 is clearly in an earlier stage of evolution. However, fewer models exist for the early evolution of massive stars than for low-mass objects, (e.g. Panagia 1973; Hosokawa & Omukai 2009; Kuiper & Yorke 2013b), and predicted parameters in the pre-main-sequence phase or on the zero-age main sequence vary strongly depending on e.g. the object's age and accretion history (which may be strongly variable, as shown for lower mass FU Ori objects by Bell & Lin 1994). These are not well constrained for AFGL 490, and this work therefore refrains from using these models. Since pre-main sequence stars have a higher infrared luminosity than on the main sequence for the same mass, the temperature of the irradiated disc may be underestimated.

Table 3.5: Overview of input parameters for the disc physical models and the radiative transfer calculation. See also Fig. 3.10.

Parameter	[Unit]	Explanation
M_{\star}	[M_{\odot}]	central star mass
L_{\star}	[L_{\odot}]	central star luminosity
T_{\star}	[K]	central star temperature
R_{in}	[au]	inner disc edge
R_{out}	[au]	outer disc edge
M_{disc}	[M_{\odot}]	disc mass
p		disc surface density power-law index
\dot{M}	[M_{\odot}/yr]	mass accretion rate inside disc
X_{mol}		molecule fractional abundance relative to H_2
v_{turb}	[km/s]	turbulent linewidth (fixed, 0.1 km/s)
i	[$^{\circ}$]	disc inclination
PA	[$^{\circ}$]	disc position angle (fixed, 30 $^{\circ}$)
d	[pc]	distance of the source (fixed, 1 kpc)

3.4. Results of the disc modelling

3.4.1 $\text{C}^{17}\text{O}(2-1)$

In the first modelling run, the C^{17}O data already analysed by Schreyer et al. (2006) is considered once more to check if the approach used in this work (especially fixed molecular fractional abundance throughout the disc instead of time-dependent chemistry) yields consistent results.

The main parameters varied are the type of the central star (M_{\star} , T_{\star} , L_{\star}), and the inclination i of the disc, which is varied from 10 $^{\circ}$ to 80 $^{\circ}$ in steps of 10 $^{\circ}$ (an edge-on

configuration is precluded from the emission morphology, and a face-on orientation as well, since it would not produce shifts of the lines from different disc positions in radial velocity). For the beginning, the outer disc radius is set to 1500 au. The resulting inner radius (dust evaporation radius) R_{rim} , ratio of rim height and inner radius $H_{\text{rim}}/R_{\text{rim}}$, and the radius R_{flare} where the disc reaches again out of the shadow cast by the inner rim, are given in Tab. 3.6. Note that due to the simplified treatment of the disc profile calculation

Table 3.6: Disc models of the first run (inner rim equals dust evaporation radius).

Designation ¹	M_{\star} [M_{\odot}]	T_{\star} [K]	L_{\star} [L_{\odot}]	M_{disc} [M_{\odot}]	p	R_{out} [au]	R_{rim} [au]	$\frac{H_{\text{rim}}}{R_{\text{rim}}}$	R_{flare} [au]
B1_10_20_1500	13.0	25400	1.6×10^4	1.0	-2.0	1500	10	0.33	1.1×10^2
B1_10_15_1500	13.0	25400	1.6×10^4	1.0	-1.5	1500	9.9	0.31	1.0×10^2
B1_10_10_1500	13.0	25400	1.6×10^4	1.0	-1.0	1500	9.8	0.27	77
B1_10_05_1500	13.0	25400	1.6×10^4	1.0	-0.5	1500	9.6	0.24	60
B2_10_20_1500	9.8	22000	5.7×10^3	1.0	-2.0	1500	5.9	0.30	76
B2_10_15_1500	9.8	22000	5.7×10^3	1.0	-1.5	1500	5.8	0.28	68
B2_10_10_1500	9.8	22000	5.7×10^3	1.0	-1.0	1500	5.8	0.25	49
B2_10_05_1500	9.8	22000	5.7×10^3	1.0	-0.5	1500	5.7	0.21	35
B3_10_20_1500	7.6	18700	1.9×10^3	1.0	-2.0	1500	3.3	0.27	42
B3_10_15_1500	7.6	18700	1.9×10^3	1.0	-1.5	1500	3.3	0.25	32
B3_10_10_1500	7.6	18700	1.9×10^3	1.0	-1.0	1500	3.3	0.22	31
B3_10_05_1500	7.6	18700	1.9×10^3	1.0	-0.5	1500	3.2	0.18	21
B5_10_20_1500	5.9	15400	8.3×10^2	1.0	-2.0	1500	2.2	0.25	25
B5_10_15_1500	5.9	15400	8.3×10^2	1.0	-1.5	1500	2.2	0.23	24
B5_10_10_1500	5.9	15400	8.3×10^2	1.0	-1.0	1500	2.1	0.20	22
B5_10_05_1500	5.9	15400	8.3×10^2	1.0	-0.5	1500	2.1	0.17	16
B8_10_20_1500	3.8	11900	180	1.0	-2.0	1500	1.0	0.22	11
B8_10_15_1500	3.8	11900	180	1.0	-1.5	1500	1.0	0.21	11
B8_10_10_1500	3.8	11900	180	1.0	-1.0	1500	1.0	0.18	10
B8_10_05_1500	3.8	11900	180	1.0	-0.5	1500	0.99	0.15	7.8
A0_10_20_1500	2.9	9500	54	1.0	-2.0	1500	0.55	0.20	9.3
A0_10_15_1500	2.9	9500	54	1.0	-1.5	1500	0.55	0.18	6.0
A0_10_10_1500	2.9	9500	54	1.0	-1.0	1500	0.54	0.15	5.2
A0_10_05_1500	2.9	9500	54	1.0	-0.5	1500	0.53	0.12	4.9
A5_10_20_1500	2.0	8200	14	1.0	-2.0	1500	0.45	2.61	...
A5_10_15_1500	2.0	8200	14	1.0	-1.5	1500	0.28	0.16	3.2
A5_10_10_1500	2.0	8200	14	1.0	-1.0	1500	0.27	0.13	2.8
A5_10_05_1500	2.0	8200	14	1.0	-0.5	1500	0.27	0.11	2.5

⁽¹⁾ The designations follow the form {SPT}_{10×M_{disc}}_{10×p}_{R_{out}}.

(i.e. evaluation of the photospheric height by piecewise power-law fit) especially the flaring

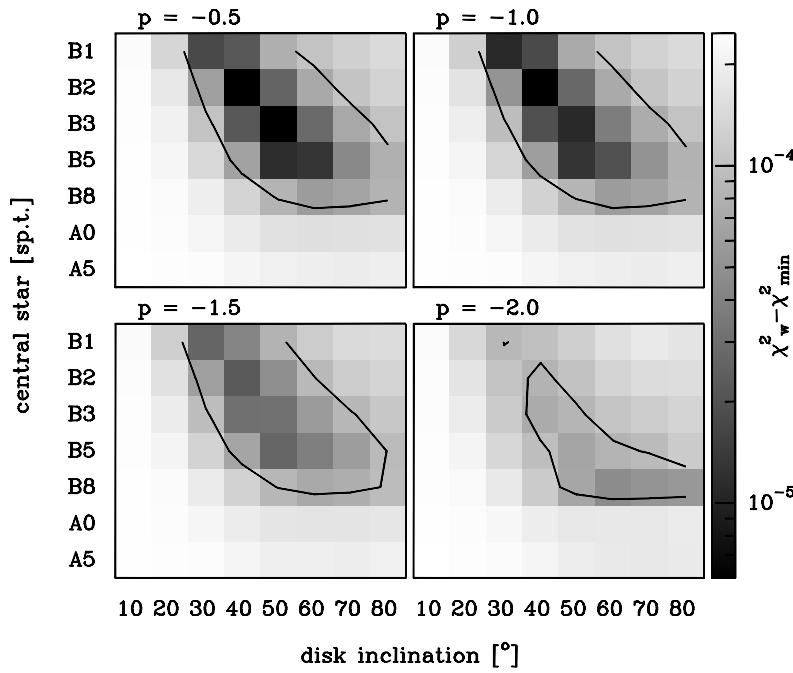


Figure 3.13: Maps of χ_w^2 for C^{17}O for disc models with different central stars and disc inclinations, and for disc surface density indices of -0.5 (upper left) to -2.0 (lower right). The difference of χ_w^2 to the absolute minimum (2.249363 for a B2 star, $i = 40^\circ$, $p = -1.0$) is given to allow for better comparison between the panels. The contour marks the region where $\chi_w^2 - \chi_{\min}^2 \leq 9 \times 10^{-5}$.

radius may vary by up to 12% depending on the starting parameters. The central velocity for the models was first set to the value from the two-Gaussian approximation to the integrated spectra (Tab. 3.3), but the final evaluation showed that χ_w^2 are minimized for a v_{LSR} of -13.1 km/s, therefore this value was applied instead. Fig. 3.13 shows the χ_w^2 for different central stars, disc inclinations and disc surface indices, but a fixed outer disc radius of 1500 au and a disc mass of $1 M_\odot$. The weighted χ_w^2 vary only slightly between the different models, i.e. are in the range 2.2493 – 2.2496 , where the smallest value corresponds to a 40° inclined disc around a B2 star with $p = -1.0$ (the according modelled spectra are overlaid on the observed ones in Fig. 3.14). This is probably due to the fact that the uv visibilities of the observed data set also contain emission outside of the disc, while for the modelled disc no emission is present in the surrounding. As a consequence, comparison of the whole uv dataset would yield a χ_w^2 larger than one even for a disc model that represented the observed disc perfectly, reflecting the residuals outside of the disc. For this reason, the “best-fit” χ_w^2 for the C^{34}S and CS observations presented in sections 3.4.3 and 3.4.4 is even higher than for C^{17}O , since strong emission in the surrounding (originating from the outflow) is present in both datasets.

Visual inspection of the C^{17}O synthetic spectra maps shows that models with a 9×10^{-5} higher χ_w^2 result in spectra significantly different from the observed C^{17}O emission (i.e. especially the blue-/redshift of the lines from v_{LSR} is not reproduced). The region with models yielding a smaller offset from the minimal χ_w^2 , which will be considered as acceptable fits to the observation, is outlined in Fig. 3.13. For comparison, the largest χ_w^2 obtained for models of e.g. very low disc inclination (10°) is similar to the χ_w^2 obtained when using a model free of any emission to model the observed visibilities. Fig. 3.14 shows

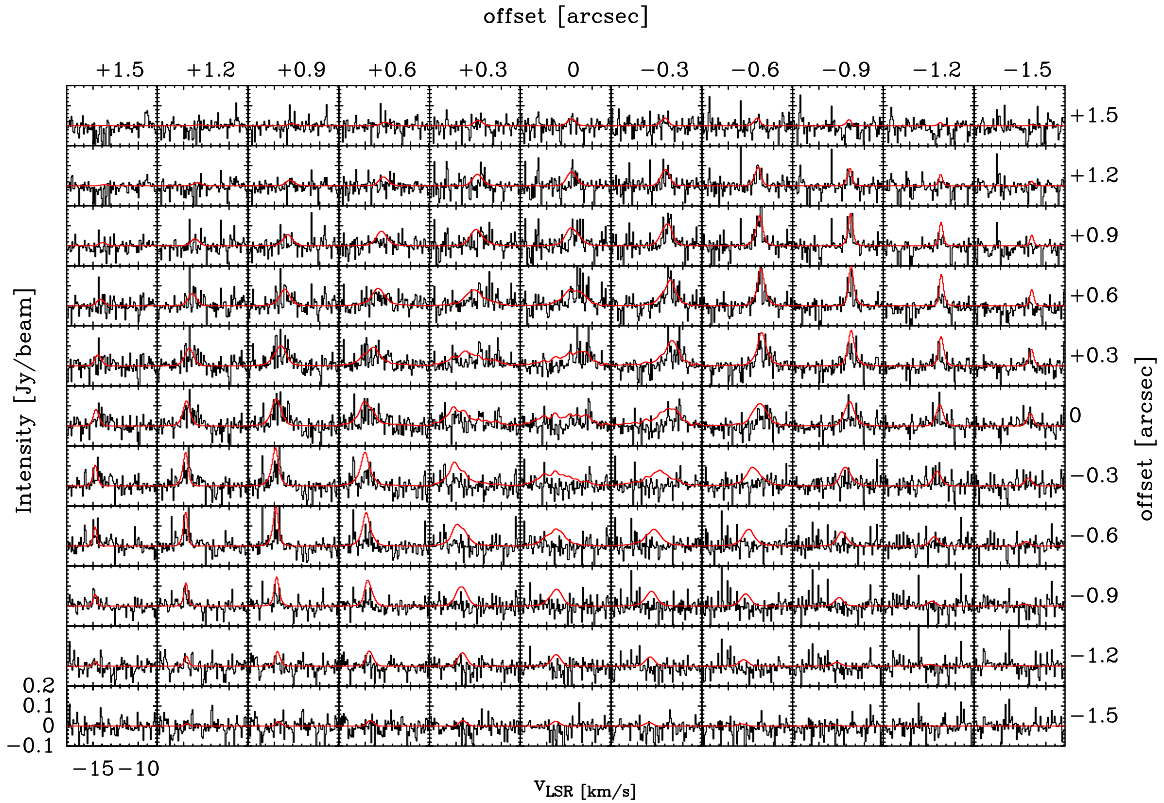


Figure 3.14: Spectra map of observed $\text{C}^{17}\text{O}(2-1)$ emission (black) overlaid with the best fitting model (red) of a disc around a B2 star with inclination of 40° , disc surface density index of -1.0 and disc mass of ca. $0.75 M_\odot$. Offsets are relative to the disc center position. The system velocity for the model is $v_{\text{LSR}} = -13.1 \text{ km/s}$.

that even for the “best-fit” model, the observed spectra are significantly below the modelled ones especially in the south-western part of the emission region, possibly due to a not homogeneous C^{17}O disc, which of course is not well represented by an axisymmetric disc model. This may also be the reason for the comparably high χ_w^2 even for the best-fit model. In general, the smallest χ_w^2 are located along a ridge from B1 and $i = 30^\circ$ to B5 and $i = 60^\circ$, so that this modelling run favours discs with intermediate inclination around early B-type central stars and high disc surface density indices ($p = -0.5 \dots -1.0$). Steeper surface density profiles result in higher χ_w^2 . Only for the steepest profile ($p = -2.0$), a highly inclined disc ($i = 60 \dots 80^\circ$) around a B8 star produces smaller χ_w^2 than less inclined discs around earlier spectral type stars. Irrespective of the disc surface density profile, small disc inclinations of $10\text{--}20^\circ$ and central stars with mass $< 3 M_\odot$ (A0 and A5) are always disfavoured. The scaling factors, i.e. the disc mass in units of M_\odot when the disc indeed has the fractional molecular abundance of C^{17}O which was assumed for the calculations (4×10^{-8}), is about $0.6\text{--}0.8$ for high disc surface density profile indices ($p = -0.5 \dots -1.0$) and central stars of early spectral type plus intermediate disc inclination. The steeper index $p = -1.5$ favours scaling factors of $0.7\text{--}1$, while the steepest profile ($p = -2.0$) with smallest χ_w^2 for highly inclined discs around a B8 star favours much lower scaling

factors of 0.3–0.4. As described earlier, here it is assumed that the line intensity scales approximately linear with the amount of C^{17}O molecules, i.e. with the disc mass if the fractional abundance of C^{17}O is kept constant or vice versa. This will be only true if the molecular emission is optically thin and the disc structure (density and temperature profile) for the scaled version of the disc mass does not change so much as to significantly influence the excitation conditions of the observed line. For a test of this hypothesis, the disc models with surface density profile index $p = -1.0$ were recalculated for a ten times smaller disc mass, i.e. $0.1 M_{\odot}$. The minimized χ_w^2 have a similar distribution as for the $1 M_{\odot}$ disc models (maximum difference 2×10^{-5}). The according scaling factors f for the $M_{\text{disc}} = 0.1 M_{\odot}$ are however not a factor of exactly 10 larger than for the $M_{\text{disc}} = 1 M_{\odot}$ models as assumed above. Instead, they reach from 7–9 for the B1–B3 central stars over 5–7 for B5–B8 to 2–4 for spectral types of A5 and A0, which is likely due to the fact that the cooler central stars sustain discs with lower temperature and smaller scale height, i.e. higher density in emission-originating disc region. As a result, the best-fitting disc masses for the $0.1 M_{\odot}$ models are a factor of 1.2–1.9 smaller than for the $1 M_{\odot}$ models, where the discrepancy is more pronounced the larger the disc inclination and the later the central star’s spectral type.

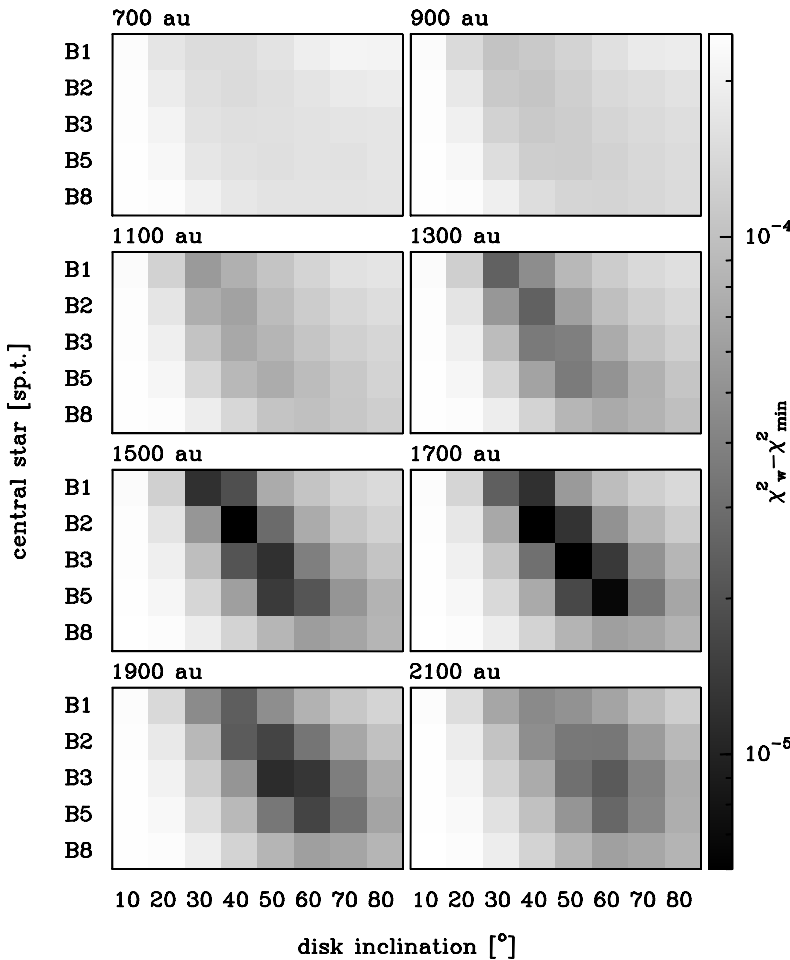


Figure 3.15: Maps of χ_w^2 for C^{17}O for disc models with different central stars and disc inclinations, and for disc outer radii (indicated above each panel) from 700 to 2100 au. The difference of χ_w^2 to the absolute minimum (2.249363 for a B2 star, $i = 40^\circ$, $p = -1.0$, $R_{\text{out}} = 1500$ au) is given to allow for better comparison between the panels.

Furthermore, for a disc surface density index if $p = -1.0$, the outer radius of the discs was varied towards both higher and smaller values (from 700 to 2100 au in steps of 200 au) to test the influence of this parameter. Here, only central stars of spectral type B were taken into account; the results are depicted in Fig. 3.15. From the best-fit models with $R_{\text{out}} = 1500$ au described above it is already clear, that the bulk of the emission must arise close to the outer edge of the disc (beyond ≈ 1000 au) in case of Keplerian rotation (see equation 3.26) to explain the observed blue/redshift of the C^{17}O lines of 1.5 ± 0.2 km/s from v_{LSR} . Therefore it is not surprising, that a decrease of the outer radius leads to an increase of χ_w^2 and makes $R_{\text{out}} < 1200$ au unlikely. Fig. 3.15 shows that the configuration of a 50° inclined disc with $R_{\text{out}} = 1700$ au around a B3 central star (scaling factor $f = 0.68$) yields a χ_w^2 similar to the previously mentioned best-fit model (B2, $i = 40^\circ$, $R_{\text{out}} = 1500$ au), and in general the region of low χ_w^2 is shifting to slightly higher inclinations, which is compatible with the explanation that most of the emission stems from the outer disc regions. For even higher disc extents ($R_{\text{out}} = 1900$ and 2100 au), rising χ_w^2 indicate a worse fit to the observed spectra, which corresponds to the fact that the synthetic spectra further away from the star are higher in intensity than the observed spectra for early B type central stars (B1–B3). For B5–B8 the effect is less pronounced since the disc midplane temperature drops below 20 K beyond 1500 au from the star and CO was assumed to be frozen out onto dust grains and therefore naturally does not contribute to the observable emission. The gas temperature rises with increasing distance from the midplane, but where it reaches the freeze-out temperature, the gas density has already dropped by a factor of ten below that of the midplane.

Looking at the maximum extent of the C^{17}O line wings in the observed spectra (about ± 3 km/s around v_{LSR}), it is however clear that in case of a disc in Keplerian rotation, gas in the regions closer than 200–300 au (for the best fitting combinations of central star type and disc inclination discussed above) to the central star should not contribute perceptibly to the observed spectral lines. The inner rim as well as the flaring radius (Tab. 3.6), and therefore the complete shadowed region, are significantly closer to the central star and are therefore unlikely to affect the shape of observed lines significantly, while the outer irradiated disc parts have the same temperature and density structure for models with and without puffed-up inner rim. Indeed, using a flared disc model without shadow casting puffed-up inner rim (for the example of $p = -1.0$) with small inner disc radii (up to 300 au) results in only marginal changes of the χ_w^2 , the distribution depending on the type of central star and disc inclination remains unchanged to the shadowed disc case, and the synthetic spectra of shadowed and unshadowed disc are practically indistinguishable. An increase of the inner disc radius (≥ 500 au) increases the χ_w^2 , indicating a less good agreement with the observed emission lines.

Summary C¹⁷O

In summary, the disc models presented here favour as explanation for the observed C¹⁷O emission a disc around an 6–10 M_⊙ (B2–B5) star with an extent $R_{\text{out}} = 1500\text{--}1700$ au, disc surface density profile index $-0.5 \dots -1.0$ and intermediate inclination of 40–60° (increasing with later spectral types), where a Keplerian rotation law was assumed for the disc. For the homogeneous C¹⁷O abundance throughout the disc assumed here, the inferred disc masses are about 0.5–1.0 M_⊙. From the C¹⁷O data, it cannot be distinguished between a standard, completely irradiated flared disc model and a model where the inner rim of the disc is puffed-up and casts a shadow on the inner disc parts. In addition, the inner radius of the disc cannot be well constrained, and inner holes with radius up to ca. 400 au cannot be excluded. Taking into account the uncertainties, these results are consistent with those of Schreyer et al. (2006), who found a configuration of a 0.2–1 M_⊙ disc inclined by $\approx 30^\circ$ in Keplerian rotation around an 8–10 M_⊙ (B2–B3) star, and a surface density gradient of $p = -1.5$ as best fitting for the observed C¹⁷O emission, although the models presented here favour a shallower disc surface density profile and somewhat higher disc inclination.

3.4.2 Modifications of the disc modelling

In the following, a few modifications of the disc model used for modelling the molecular emission in the preceding sections will be discussed. To evaluate the implications on the synthetic spectra, the best fit model for the C¹⁷O emission (B2 star, $p = -1.0$, $i = 40^\circ$, for $R_{\text{out}} = 1500$ au) is considered because of the high quality and spatial resolution of the C¹⁷O data.

Computational issues

As a first test, synthetic spectra were calculated with the full radiative transfer method instead of the LVG method to test the deviations. Except of the significantly longer computation time, the final beam-convolved synthetic spectra for the disc from the both methods show no conceivable difference, the minimal χ_w^2 is identical, and the scaling factor f is decreased by $< 1\%$. That means that for the purposes of this work, where the relatively large synthesized beam size will smear out deviations on small spatial scales, and only discs in Keplerian rotation assumed for the modelling, the LVG method indeed represents a sufficiently exact approach. Sources of uncertainty and deviations are more likely the – due to computational load – relatively coarse grid of physical parameters for the model disc, and the simplified approach used for calculating the disc density and temperature structure, than the radiative transfer part.

In a next step, the influence of the relatively coarse coordinate grid (to speed up computation) chosen for disc modelling was considered. Depending on the initial parameters (e.g. initial kinetic temperature, which governs the spatial grid) for calculation of the disc

physical structure, the disc temperature and photospheric height profiles were found to vary somewhat, occasionally showing jumps. For the aforementioned disc model, two runs with (unrealistically) very low (10 K) and high (700 K) initial temperatures were calculated; the resulting best-fit scaling factors deviate by $< 5\%$ and the minimum χ_w^2 by few 10^{-7} from the values found for the standard disc model used in the $C^{17}O$ modelling earlier in this chapter. These deviations in f and χ_w^2 are significantly smaller than the differences between the various star and disc models as seen e.g. in Fig. 3.13. Hence, it can be concluded that although the initial parameters of the disc structure modelling have an influence on the resulting spectra and fit parameters, this influence is small and does not degrade the conclusions drawn earlier in this chapter.

Accretion

In the following, the implications of accretion in the disc are considered. First, the calculations were repeated with an accretion rate of 10^{-5} , 10^{-6} and $10^{-7} M_{\odot}/\text{yr}$ without changing the velocity structure of the disc. As outlined earlier, the contribution of accretion to the disc heating is negligible compared with the stellar heating, therefore the disc structure should remain unchanged. As expected, the beam-convolved synthetic spectra do not change with any of the accretion rates included.

In contrast, a notable effect on the spectra could be expected when the radial inward motion of material necessary for the according accretion rate (of disc material towards the star) is taken into account. In a simple approach, this motion is assumed to occur only in the radial direction, i.e. a velocity component in the z -direction is neglected (due to the geometrically thin disc only a small velocity component in the vertical direction should be necessary to keep the material flow inside the disc structure). The radial velocity component v_r is calculated by requesting that at each radial distance R from the star, the flow of material integrated over a thin annulus and the full disc height equals the given accretion rate, yielding

$$v_r(R) = \frac{\dot{M}}{4\pi\Sigma(R)} \frac{1}{R} \quad , \quad (3.27)$$

which actually represents the average (averaged over the vertical height z) radial inward velocity at radial distance R . Note that in case of the $C^{17}O$ best-fit disc model with disc surface density index $p = -1.0$ this results in a $v_r = \dot{M}(R_{\text{out}} - R_{\text{in}})/M_{\text{disc}}$, i.e. constant throughout the disc. For the standard setup of a $M_{\text{disc}} = 1 M_{\odot}$ disc around the B2 star and an accretion rate of $10^{-6} M_{\odot}/\text{yr}$ this yields $v_{\text{rad}} = 7 \times 10^{-3} \text{ km/s}$, one magnitude smaller than the channel width of the observed spectra and the assumed turbulent linewidth. Therefore, no noticeable effect on the modelled spectra is expected for intermediate mass accretion rates.

Velocity laws

So far, the standard Keplerian rotation law $v_{\text{rot}} = \sqrt{GM_*/R}$ taking into account only the stellar mass was assumed for the calculations. In the following, a few other rotation laws of the form $v_{\text{rot}}(R) = v_0(R/R_0)^q$ are considered: a constant rotational velocity $q = 0$, a rotation law similar to a rigid body $q = 1$, a Keplerian rotation law $q = -0.5$ but with varied v_0 , and rotation laws with $q = -1$ and $q = -2$ where the rotational velocity decreases more quickly with increasing radial distance from the star than in the Keplerian case. In each case, the initial v_0 is chosen such, that – similar to the best-fit disc model – at an inclination $i = 40^\circ$ the projected radial velocity for the outer disc regions (1000–1500 au) is comparable to the one in the observed C^{17}O spectra. For an $R_0 = 1000$ au in the upper equation, this corresponds to $v_0 = 2.5 \dots 3.5$ km/s (but the range of v_0 is extended to cover the minimum χ_w^2 if necessary). The resulting distribution of χ_{min}^2 is shown in Fig. 3.16.

For a rigid-body-like rotation, where the rotational velocity increases linearly with radial distance from the star, a minimum χ_w^2 is reached for $v_0 = 5.2$ km/s (not contained in Fig. 3.16), but this minimum value exceeds the one of the disc in Keplerian rotation by 1.5×10^{-4} . Moreover, the modelled spectral lines exhibit a noticeable larger shift from the AFGL 490 system velocity with increasing distance from the central source, and therefore clearly do not fit to the observed C^{17}O lines. A rigid-body-like rotation law is therefore in disagreement with the observations.

For the constant rotation velocity, the resulting beam-convolved spectra show narrower lines than the standard disc in Keplerian rotation, since the spread in radial velocities is only due to projection of different azimuthal parts of the disc, but not due to different rotational velocities at different disc radii as in case of the other rotation laws (which smear out the emission over a wider velocity range). For the same reason, the spectral lines are more asymmetric especially in the outer disc regions, showing extended wings towards the centre but steep shoulders on the sides facing away from the centre. These line profiles do not represent the observed lines well, however, with the $\Delta\chi_w^2 < 9 \times 10^{-5}$ criteria used in section 3.4.1, a rotation velocity constant throughout the disc with $v_0 = 2.6 \dots 2.9$ km/s cannot be completely ruled out.

For the Keplerian rotation law with $q = -0.5$, the minimum χ^2 is reached for $v_0 = 2.9$ km/s, which is identical to $\sqrt{GM_*/R_0}$ with the stellar mass of the B2 central star. Taking into account not only the stellar mass, but also the mass of the disc inside each radial distance R considered, $v_{\text{rot}} = \sqrt{G[M_* + M_{\text{disc}}(r \leq R)]/R}$ (i.e. these calculations have to be iterated, taking the scaling factor f times the former disc mass as disc mass of the new calculation, yielding a disc mass of $0.71 M_\odot$), yields a slightly (5×10^{-6}) higher χ^2 than the law taking into account only the stellar mass. Applying this velocity law for the disc with $p = -1.0$ and $R_{\text{out}} = 1500$ au for all spectral types A5–B1 and inclinations 10 – 80° as in section 3.4.1, the result is similar: the χ_{min}^2 change by 1.6×10^{-5} at most, and the distribution displayed

in Fig. 3.13 does not change noticeably.

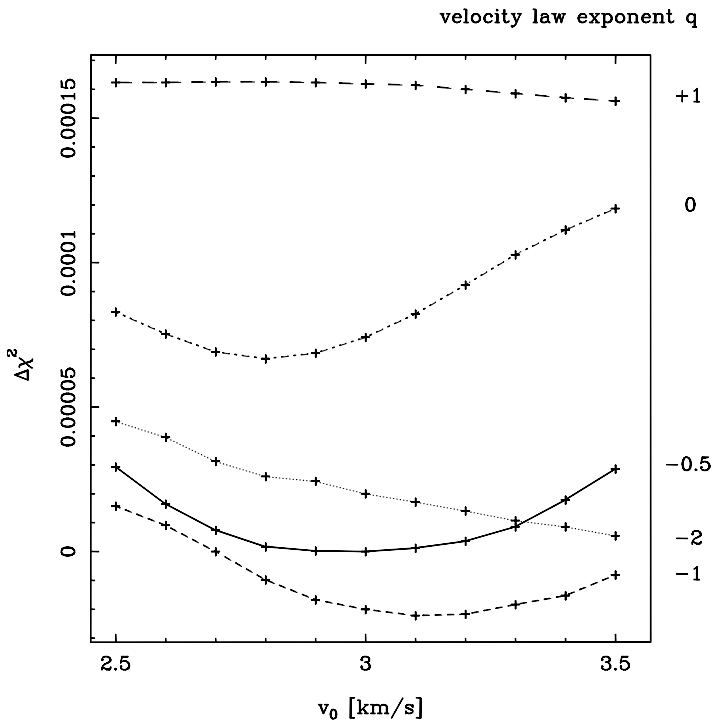


Figure 3.16: Minimum χ^2 for velocity laws of the form $v_{\text{rot}}(R) = v_0(R/R_0)^q$ and several parameters v_0 and q ; displayed is the difference between χ^2 and the χ^2_{min} of a disc in Keplerian rotation $v_{\text{rot}} = \sqrt{GM_*/R}$ around a B2 star. For values $\Delta\chi^2 < 9 \times 10^{-5}$, synthetic spectra deviate significantly from the observed ones. For more details, see text.

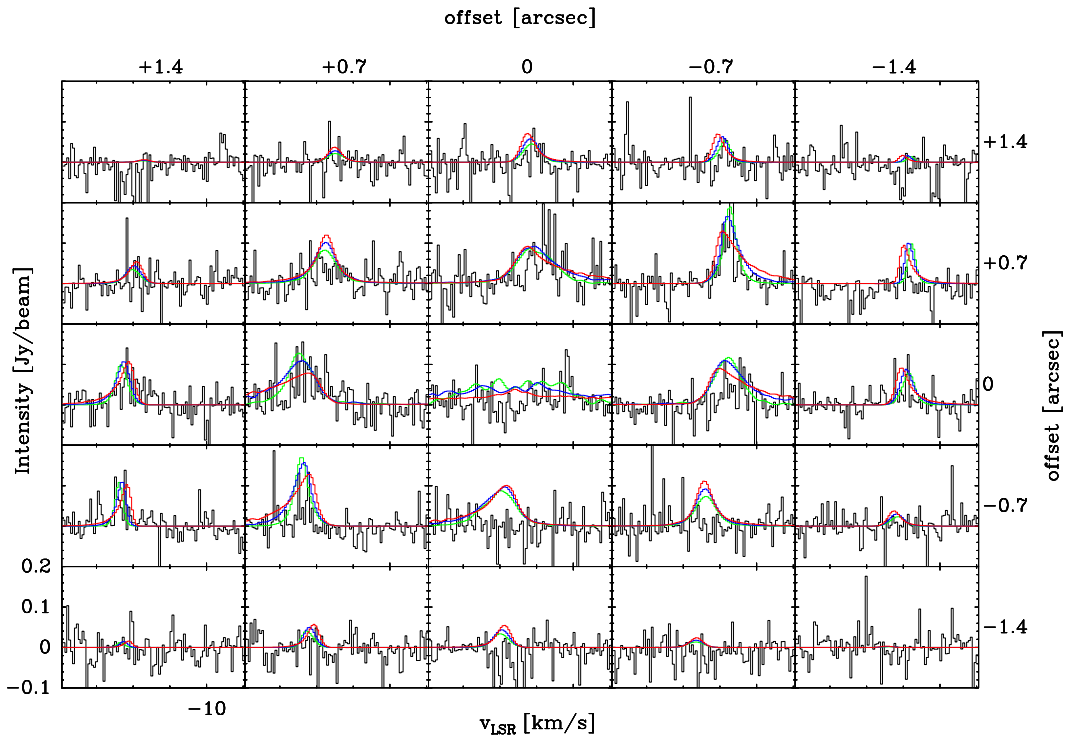


Figure 3.17: Observed C^{17}O spectra (black) overlaid with best-fit model spectra for an $i = 40^\circ$, $R_{\text{out}} = 1500 \text{ au}$, $p = -1.0$ disc around an B2 central star for different rotation velocity laws $v_{\text{rot}} \propto R^q$: $q = -0.5$ (green), $q = -1.0$ (blue) and $q = -2.0$ (red).

For the velocity laws with a steeper index $q = -1$ and -2 , even smaller χ^2 than for the disc in standard Keplerian rotation are reached. For $q = -1$ and -2 , the minimum χ^2 is

reached for $v_0 = 3.1$ km/s and 3.5 km/s, respectively. Here the line profiles in the outer disc regions exhibit an asymmetry opposite to the $q = 0$ case: steep slopes facing towards the central star and extended wings facing away from it. A comparison of the models with smallest χ^2 is shown in Fig. 3.17.

In summary, for this particular disc configuration (B2 central star, disc size 1500 au, inclination 40° , surface density profile index -1.0) laws with an rotation velocity $v_{\text{rot}} \propto R^q$ are favoured for q in the range $-2.0 \dots 0$, where the law with $q = -1.0$ yields the smallest χ^2 in comparison with the observations.

3.4.3 C³⁴S(2–1)

As already presented in the observations summary (see Fig. 3.2 to 3.5), the red- and blueshifted lines of the C³⁴S emission have a somewhat larger separation than those of C¹⁷O, i.e. are shifted from v_{LSR} by about 2.4 km/s instead of 1.4 km/s, and a lower signal-to-noise ratio. Beginning with the same starting parameter set as described in section 3.4.1, i.e. a $1 M_\odot$, $R_{\text{out}} = 1500$ au, $10\text{--}80^\circ$ inclined disc with disc surface density profile indices between -0.5 and -2.0 around stars of type B1–A5, yields the weighted χ^2 presented in Fig. 3.18.

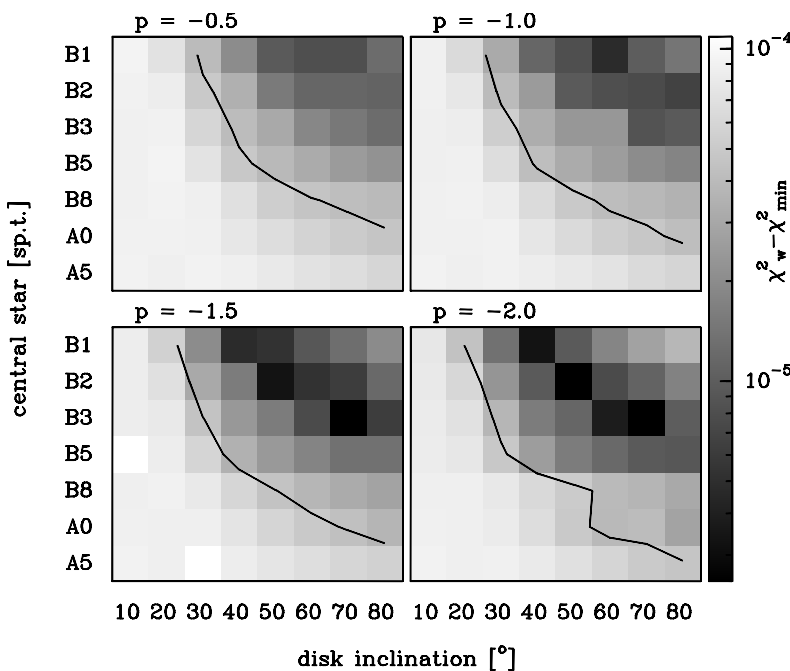


Figure 3.18: Maps of χ_w^2 for C³⁴S(2–1) for disc models with different central stars and disc inclinations, and for disc surface density indices of -0.5 (upper left) to -2.0 (lower right). The difference of χ_w^2 to the absolute minimum (6.60865 for a B2 star, $i = 50^\circ$, $p = -2.0$) is given to allow for better comparison between the panels. The contour marks the region where $\chi_w^2 - \chi_{\text{min}}^2 \leq 4.5 \times 10^{-5}$.

A comparison of the synthetic spectra maps for the same star–disc model for C¹⁷O(2–1) and C³⁴S(2–1) shows as main difference double-peaked line profiles or lines with broad shoulders throughout the disc for C³⁴S, and a less steep decay of the line intensities with increasing distance from the disc center than in the C¹⁷O spectra, while the shift from the system velocity of the dominant line component is similar to that of C¹⁷O, which indicates that the according lines are formed in regions of similar distance to the central

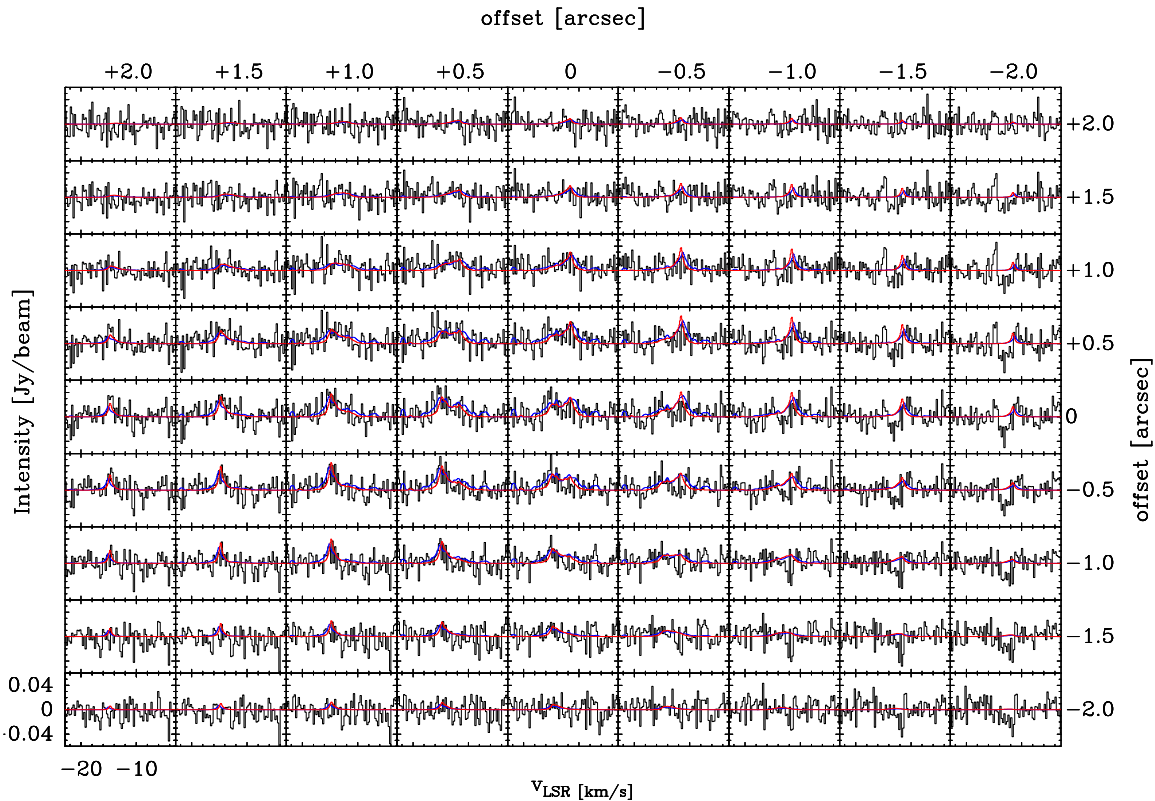


Figure 3.19: Spectra map of observed $\text{C}^{34}\text{S}(2-1)$ emission (black) overlaid with the best fitting model of C^{34}S , a 50° inclined, $1.3 M_\odot$ disc with surface profile $p = -2.0$ around a B2 star (blue) and the best fitting model for $\text{C}^{17}\text{O}(2-1)$, a 40° inclined disc with $p = -1.0$ around a B2 star (red), but with disc mass $0.5 M_\odot$ (instead $0.75 M_\odot$). Offsets are relative to the disc center position. The system velocity for the model is $v_{\text{LSR}} = -13.1 \text{ km/s}$.

star. These facts are a result of the larger synthesized telescope beam (ca. $2''$), so that at each spatial position emission from a larger region, often even from the opposite side of the rotating disc, is incorporated in the beam, which is not the case for the higher resolution observation (ca. $0.8''$). Therefore, also the differences in the synthetic spectra for different star–disc combinations are less pronounced for C^{34}S than for C^{17}O . Indeed, the χ_w^2 distributions in Fig. 3.18 are even shallower than for C^{17}O . Like for the latter, the modelled spectra were inspected visually to find the $\chi_w^2 - \chi_{\text{min}}^2 = 4.5 \times 10^{-5}$, above which the modelled emission lines are clearly offset from the observed ones. The minimal χ_w^2 are reached for early-type (B1–B3) central stars and discs with steep surface density profile indices ($-1.5 \dots -2.0$). This favouring of higher inclinations and steeper surface density profiles than for the C^{17}O observations is a result of the larger blue/redshift of the C^{34}S lines. The disc masses obtained from the fits to the C^{34}S spectra are approximately $0.8\text{--}1.5 M_\odot$ for $p = -2.0$ and $0.4\text{--}1.0 M_\odot$ for $p = -1.0$. However, the best-fit star–disc configuration from the C^{17}O observations (B2, $p = -1.0$, $i = 40^\circ$) – overplotted on the observed spectra in Fig. 3.19 – shows only somewhat narrower line profiles than the model with minimum χ_w^2 (B2, $p = -2.0$, $i = 50^\circ$) and can

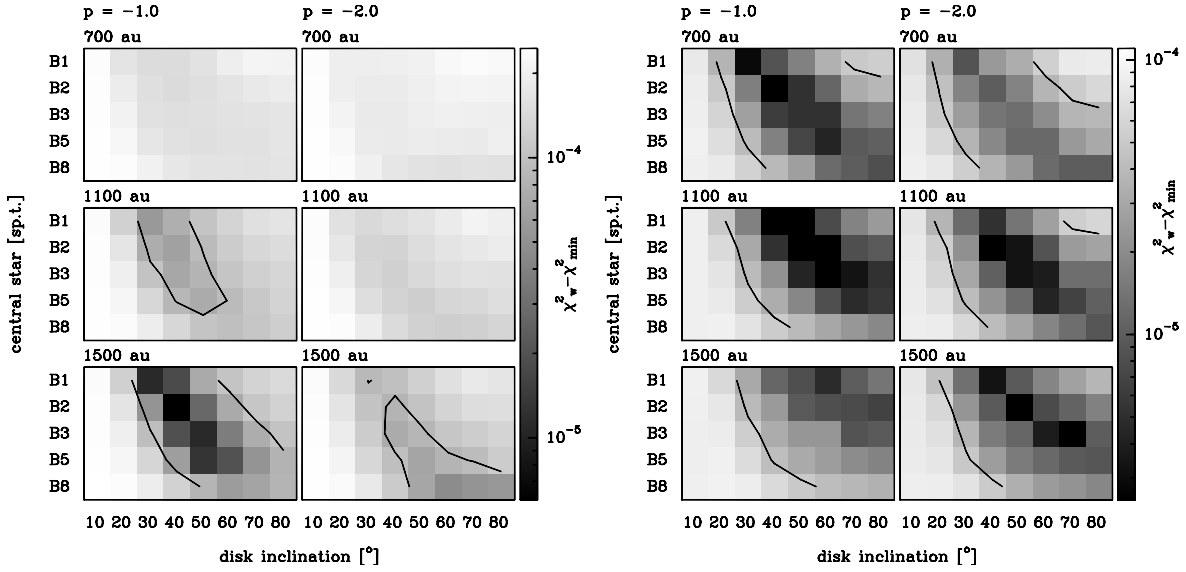


Figure 3.20: Maps of χ_w^2 for disc models with different central stars and disc inclinations, where the disc outer radii is varied from 700 to 1500 au (from top to bottom), for both $C^{17}O$ (left six panels) and $C^{34}S$ (right six panels), each for two disc surface density indices (-1.0 , left row each, and -2.0 , right row). The difference of χ_w^2 to the absolute minimum ($C^{34}S$: 6.608657 for a B2 star, $R_{\text{out}} = 1500$ au, $i = 50^\circ$, $p = -2.0$; $C^{17}O$: 2.249363 for a B2 star, $R_{\text{out}} = 1500$ au, $i = 40^\circ$, $p = -1.0$) is given to allow for better comparison between the panels. The contours mark the regions where $\chi_w^2 - \chi_{\text{min}}^2 \leq 4.5 \times 10^{-5}$ ($C^{34}S$) and 9×10^{-5} ($C^{17}O$).

therefore be considered compatible with the observed $C^{34}S$ spectra. In general, all star–disc combinations beyond a line from (B1, $i = 30^\circ$) to (A0, $i = 80^\circ$) for any of the disc surface density profile indices considered cannot be excluded from the observed $C^{34}S(2-1)$ line emission (see Fig. 3.18), although, as already in the case of $C^{17}O$, the χ_w^2 are overall smallest for central stars of type B1–B5 (M_* ca. 6–13 M_\odot). For the assumed disc-wide homogeneous $C^{34}S$ abundance of 5×10^{-10} , scaling factors $f = 0.4 \dots 1.3$ are found for the star–disc combinations in the regions in Fig. 3.18 enclosed by the contour lines, which is comparable with those from the $C^{17}O$ models despite the large uncertainty in the assumed molecular abundance. As before, the scaling factor (i.e. roughly the disc mass) increases with increasing disc inclination i , earlier central star spectral type, and decreasing surface density profile index p .

As for $C^{17}O$, the influence of the outer disc radius is explored for B type central stars by varying R_{out} for the $p = -1.0$ and $p = -2.0$ surface density profiles. For the same p , the $C^{34}S$ data obviously favour smaller disc radii than for $C^{17}O$, since they yield larger line shifts from v_{LSR} . However, a reasonable assumption would be that the $C^{34}S$ emission originates from the same disc as $C^{17}O$ (i.e. same inclination, central star and mass). Since the model uv visibilities were calculated with the same uv baselines as the observations, filtering out of different emission regions by the different telescope configurations should have no effect.

In this case, the $C^{34}S$ spectra must be dominated by emission from a region closer to the central star than the $C^{17}O$ spectra. While the minimum of χ_w^2 for $C^{34}S$ is reached for $p = -2.0$ and $R_{\text{out}} = 1500$ au, a wider range of models with comparable χ_w^2 is found for the $p = -1.0$ surface density profile which is also favoured by the $C^{17}O$ observations – i.e. staying with the $p = -1.0$ model, both molecular observations favour a similar range of central stars and inclinations (B1, $i = 30^\circ$ to B5, $i = 60^\circ$, inclinations with tendency to be slightly higher for $C^{34}S$) but with outer disc radius of 1500 au for $C^{17}O$ and only 700–1100 au for $C^{34}S$. This could suggest a different distribution of $C^{34}S$ throughout the disc. In the modelling, a higher freeze-out temperature for $C^{34}S$ of 20 K was taken into account, but even for the model with a B5 central star the disc midplane temperature does not drop below 30 K up to 1500 au radius, rendering the freeze-out as cause for the lack of $C^{34}S$ unlikely. It is however possible that the both molecules are not homogeneously distributed over the disc due to chemical evolution, which is not covered by the model used here. For protoplanetary discs around low-mass stars it has been shown that many molecules are concentrated in an intermediate layer of 0.5–1 pressure scale heights due to the chemical evolution, and the CS abundance was found to peak toward the inner disc region in chemical models (Pavlyuchenkov et al. 2007). It is however unsure if these results can be transferred directly to the more massive disc around an almost high-mass object assumed here.

3.4.4 CS(1–0)

With a similar set of start parameters as for the $C^{17}O$ and $C^{34}S$ modelling, discs with different inclinations and disc surface density indices were compared with the CS(1–0) emission measured by the VLA-D array. The resulting weighted χ_w^2 are presented in Fig. 3.21. With the red- and blueshifted emission extending to even larger velocity shifts than in $C^{17}O$ and $C^{34}S$ (Tab. 3.2), it is not surprising that the minimum of χ_w^2 is shifted to even higher central star masses and inclinations: the absolute minimum is reached for $p = -1.5$ at the maximum inclination of 80° and B1/B2 central stars.

However, the spectra map in Fig. 3.22 reveals that the according synthetic spectra does not represent an acceptable approximation of the observed spectra – while the position in velocity of the redshifted and blueshifted component is more or less reproduced, the intensity is much lower due to a small scaling factor f . For inclinations up to 40° , most of the disc models yield scaling factors $f < 1 \times 10^{-3}$, since they predict smaller line shifts than observed and therefore completely disagree with the observed spectra. Larger scaling factors up to $f = 0.7$ are found e.g. for a B1 star and disc with $p = -2.0$, $i = 50^\circ$. As mentioned before, the scaling factor f is useful for estimating the disc mass only for optically thin transitions, while CS(1–0) is expected to be optically thick and dominated by emission originating from regions closer to the disc surface. However, scaling factors in the order of 1 signal that the assumed combination of disc mass and fractional CS abundance yields synthetic line intensities at the same order of magnitude as the observed ones.

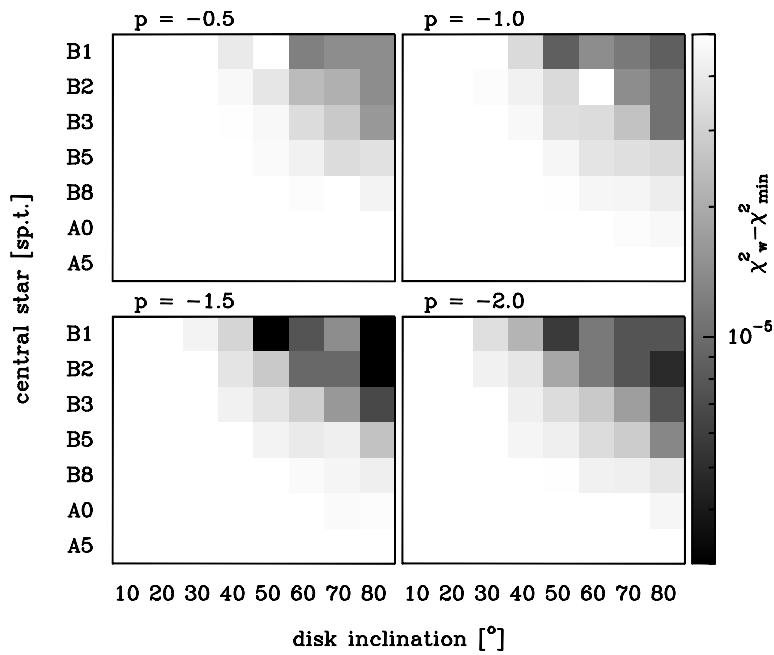


Figure 3.21: Maps of $\chi_w^2 - \chi_{\min}^2$ for CS(1–0) VLA-D array observations for disc models with different central stars, disc inclinations, and for disc surface density indices of -0.5 (upper left) to -2.0 (lower right). The difference of χ_w^2 to the absolute minimum (12.862334 for a B1 star, $i = 80^\circ$, $p = -1.5$) is given to allow for better comparison between the panels.

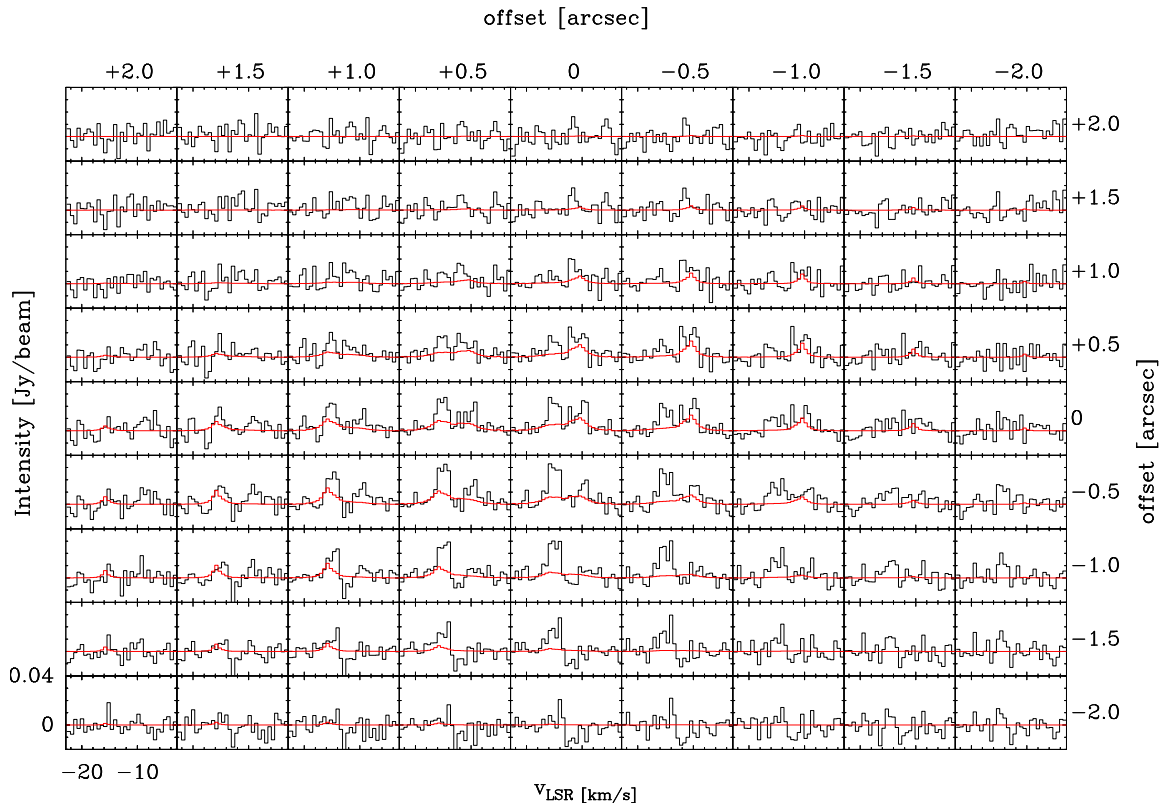


Figure 3.22: Spectra map of observed CS(1–0) VLA(D) emission (black) overlaid with the "best fitting model" of CS(1–0), a 80° inclined, $0.2 M_\odot$ disc with surface profile $p = -1.5$ around a B1 star (red). Offsets are relative to the disc center position. The system velocity for the model is $v_{\text{LSR}} = -13.1$ km/s.

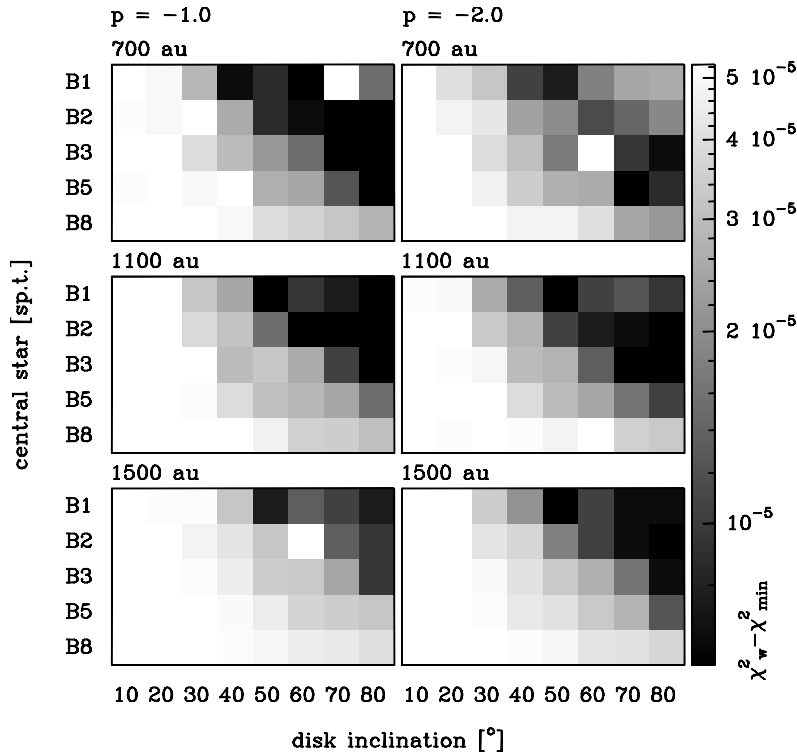


Figure 3.23: Maps of χ_w^2 for CS(D) for disc models with different B type central stars and disc inclinations, and for disc outer radii (indicated above each panel) from 700 to 1500 au. The difference of χ_w^2 to the absolute minimum (12.862335 for a B2 star with either $i = 70^\circ$, $p = -1.0$, $R_{\text{out}} = 700$ au or $i = 70^\circ$, $p = -2.0$, $R_{\text{out}} = 1100$ au) is given to allow for better comparison between the panels.

In summary, disc models with small inclinations exhibiting narrow lines with small shift in velocity, as well as highly inclined models producing very broad line profiles with higher velocity shift, fail to reproduce the observed CS(1–0) emission. It should also be noted that CS(1–0) shows emission over a larger velocity range than the other transitions (Tab. 3.3). Accordingly, a variation of the outer disc radius (Fig. 3.23) favours disc radii of 700–1100 au for surface density profiles of $p = -1 \dots -2$, as was the case for C³⁴S. However, for CS(1–0) even larger inclinations (B1, $i = 40^\circ$ to B3, $i = 80^\circ$) would be required.

While it is possible that the relatively coarse physical disc model used as input for the radiative transfer calculations is not sufficient to trace well the formation of an optically thick line, it is similarly conceivable that the CS(1–0) emission does not originate exclusively from the proposed disc, but also from other surrounding material, since it traces lower density material than its isotope C³⁴S. This possibility is supported by the discussions in the following chapter, which show that the emission in the further environment of AFGL 490 exhibits similar line shifts and is thought to originate in the outflow shell.

3.4.5 CH₃OH(2₀–1₀ E), (2₀–1₀ A⁺) and (2_{–1}–1_{–1} E)

As already discussed in section 3.1.2, it is questionable whether the CH₃OH lines close to AFGL 490 are indeed connected with the supposed disc. It is now widely accepted that methanol forms predominantly on ice-covered dust grains and is enriched in the gas phase by release from the dust – either by sputtering off from the grains in shocks (and therefore abundantly observed in outflow regions), by evaporation of the grain ice mantles due to

heating by a young stellar object, or through non-thermal desorption by UV photons or cosmic rays (the latter probably less effective). This increases typical fractional abundances relative to H_2 from 10^{-9} in cold dark clouds up to 10^{-7} – 10^{-6} in outflow regions (e.g., Tafalla & Bachiller 2011; Kristensen et al. 2010).

CH_3OH is a slightly asymmetric top molecule, since the OH radical is inclined relative to the symmetry axis of the CH_3 group and may rotate internally, introducing additional "torsional" energy levels. Depending on the spin alignment of the protons in the CH_3 group, methanol type A (parallel proton spins) and type E (one antiparallel proton spin) are distinguished, which can be treated like separate molecules (Flower et al. 2012). Therefore, compared to the diatomic molecules CO and CS, in the same range of excitation energies methanol possesses a much larger number of energy levels (e.g., Rabli & Flower 2010b), making it a valuable tool for probing different physical environments due to the multitude of transitions with only small spacing in frequency. Since a complete set (J, K) of rotational levels (where $|K| \leq J$ and K is the projection of J onto the molecule symmetry axis) up to a rotational quantum number J_{\max} contains $(2J_{\max} + 1)^2$ energy levels, the number of possible collisional transitions scales with $\frac{1}{2}J_{\max}^4$ and therefore quickly grows to numbers which hamper radiative transfer calculations due to the computational load. Leurini et al. (2004) took into account only the lowest 100 levels (i.e. complete up to $J_{\max} = 9$), which was reasonable for their sources with temperatures < 50 K. However, the disc models presented here reach higher temperatures above hundred Kelvin in the disc regions of intermediate height, which would require inclusion of more than 220 levels to not yield considerably deviant level populations by neglecting significantly populated higher levels. Due to computational limitations, in the work presented here the treatment with URAN(IA) is limited to a complete coverage up to $J_{\max} = 10$ for the torsional ground state (121 levels). The energy levels covered are thus incomplete above 130 K and it is expected that the outcome of the radiative transfer calculations for CH_3OH is not a good description of the true disc emission. In addition, the collisional rates in the molecular data files from the Leiden database (based on calculations by Rabli & Flower 2010a) cover a temperature range only up to 200 K. Moreover, Leurini et al. (2007) showed that infrared pumping – likely occurring in the immediate vicinity of such luminous protostars like AFGL 490 and not included in the radiative transfer calculations of this work – of the level populations may play an important role. For these reasons, together with the suspicion that the CH_3OH emission observed close to AFGL 490 may not originate from the disc, a modelling of the CH_3OH emission for the disc is not attempted here, but it is definitely a desirable task for future work.

Optically thick lines

The question remains, what is the cause for the asymmetric shape of the integrated C^{17}O intensity (Fig. 3.6), which is also visible in the spectra maps as a deficit of spectral lines south-west of the AFGL 490 continuum peak (according to the large-scale outflow structure,

the side of the disc near to the observer) and the apparently lower line intensity close to the disc centre. Schreyer et al. (2006) argued that this could be the result of a clumpy disc structure due to the young age and possible nonsteady accretion history of AFGL 490, or that the emission shape traces density wave structures which can be excited in massive, gravitationally unstable discs. On the other hand, Gómez & D'Alessio (2000) showed that for a disc model around a T Tauri star, optically thick $C^{17}O(2-1)$ lines from an inclined disc will show lower intensity on the side closer to the observer than on the far side (due to the disc flaring and temperature decreasing outwards, and hence lines of sight on the far side of the disc intersecting warmer regions). They also showed that a reduced contrast between line and continuum close to the disc centre is natural result of high continuum opacities, i.e. the combined intensity of continuum and line becomes optically thick if the continuum is intense, resulting in a lower line intensity in the centre of the disc than in the outer parts after continuum subtraction, which appears as “emission hole”. This also contributes to the fact, that the line emission traces mainly the outer parts of the disc (besides the effect that the area contributing to emission at high velocities close to the disc centre is smaller than that of the outer disc regions, Gómez & D'Alessio 2000 and references therein). At a first look, these features resemble the $C^{17}O(2-1)$ observations of AFGL 490 with an apparent lack of line emission close to the centre and the south-western part of the disc. However, taking into account the geometry of the large-scale outflow with the redshifted lobe facing north-east and the blueshifted one south-west, and assuming perpendicularity of disc and outflow, the south-western part would represent the far side of the disc which in analogy to (Gómez & D'Alessio 2000) should be brighter if the $C^{17}O$ emission were optically thick. The opacity at the line center of a (thermally broadened) molecular transition is given by:

$$\kappa_{\text{line}} = \frac{A_{\text{ul}} g_{\text{u}} c^3}{8\pi\nu^3} \sqrt{\frac{m_{\text{mol}}}{2\pi kT}} \frac{X_{\text{mol}}}{Q\mu m_{\text{H}}} (1 - e^{-h\nu/kT}) e^{-E_{\text{l}}/kT} \quad , \quad (3.28)$$

where the transition is characterised by the spontaneous emission coefficient A_{ul} , energy of the lower level E_{l} , weight of the upper level g_{u} and partition function Q . With the according values from the Leiden molecular database, partition functions from Cologne database of molecular spectroscopy (CDMS, Müller et al. 2001, 2005) and $X_{\text{mol}} = 4 \times 10^{-8}$, for $C^{17}O(2-1)$ this would correspond to $\kappa_{\text{line}} \approx 0.3, 0.06$ and $0.01 \text{ cm}^2/\text{g}$ at 38, 75 and 150 K, respectively. On the other hand, for a disc surface profile with $p = -1.0$, disc mass $1 M_{\odot}$, outer disc radius 1500 au and negligible inner disc radius, the disc surface density follows $\Sigma(R) = 950R^{-1} \text{ g/cm}^{-2}$ for the radius R in units of au (note that here Σ denotes the density integrated over the full disc thickness and not only half of it as earlier in this chapter). This in turn means that looking pole-on on the disc, an optical depth of $\tau \approx \Sigma\kappa_{\text{line}} = 1$ is exceeded only at radii less than 100 au (for B2–B5 type central stars with typical midplane temperatures around 75 K at these radii). Such small distances from the central stellar object are not resolved by the observations considered here, and the outer disc regions should

produce optically thin emission unless viewed under a very high inclination angle which could increase the path length (although the surface layers will be less dense and warmer, further decreasing the opacity). Hence, it appears more probable that the $C^{17}O$ asymmetric emission pattern is due to a clumpy structure as proposed by Schreyer et al. (2006, and references therein), which could also be the reason for the not smooth but “spiky” shape of the spectral lines (as if they were composed of a number of narrower velocity components and not a smoothly filled disc).

For $C^{34}S(2-1)$ however, the lines may become optically thick already at several hundred up to 1000 au from the centre (depending on the central star luminosity and hence disc temperature), and for $CS(1-0)$ the lines are expected to be optically thick throughout the whole disc. This estimate however holds for the fractional molecular abundances from Tab. 2.2, which are assumptions and not well constrained; an one magnitude lower abundance would make $C^{34}S(2-1)$ optically thin like $C^{17}O$.

However, the effect of line formation at different depths in the disc on the near and far side of the disc should also be covered by the radiative transfer calculations used in this work. In addition, there is no clear sign that the $C^{34}S$ and CS emission are shifted toward the south-east of AFGL 490 (as could be expected for a significantly brighter far side of the disc), but this is difficult to assess due to the low spatial resolution. The reduced line-to-continuum contrast close to the central object could be lost since the continuum radiation was not included in the calculations, but this should affect only the innermost disc regions and decrease with decreasing continuum frequencies (section 3.1.1).

3.5. Summary and discussion

Subsuming the results of the disc modeling for $C^{17}O(2-1)$, $C^{34}S(2-1)$ and $CS(1-0)$, the overall picture is inconclusive. All transitions show a red- and blueshifted velocity component symmetric about the central source AFGL 490, where the amount of velocity shift and width of the lines is of a similar order of magnitude, but their scatter between the different transitions exceeds the uncertainties of the values. The position angles agree within their large uncertainties, but exhibit a large scatter as well. The position-velocity diagrams along a cut connecting the $C^{17}O$ velocity components favour a Keplerian velocity profile with disc inclination $\leq 30^\circ$ if the central object had $8 M_\odot$. The comparison of observations with synthetic spectra from radiative transfer modelling favours moderately massive central objects ($6-13 M_\odot$) with discs of higher inclinations ($30-50^\circ$) and shallow surface density profile ($p = -0.5 \dots -1.0$) for $C^{17}O$, while even higher disc inclinations ($8-13 M_\odot$, $i = 40-70^\circ$) and a steeper surface density profile ($p = -1.5 \dots -2.0$) are suggested by the $C^{34}S$, and inclinations up to the maximum value of $i = 80^\circ$ by the CS (VLA-D array) data, which however are expected to be optically thick. For a moderately shallow surface density profile with $p = -1.0$, the $C^{17}O$ observations suggest an outer disc

radius of 1500–1700 au, while the $C^{34}S(2-1)$ and $CS(1-0)$ data favour a smaller extent of 700–1100 au, which could point to CS being more concentrated in the inner disc regions than CO. For discs around low-mass stars, different apparent outer disc radii are known for CO due to selective photodissociation (Dartois et al. 2003), and a gradient of CS abundance peaking in the inner disc region has been mentioned by Pavlyuchenkov et al. (2007), but the topic remains to be explored for massive discs. Therefore, the parameters, especially the inclination, of the supposed circumstellar disc around AFGL 490 from $C^{17}O$, which had been first reported in Schreyer et al. (2006), could not be constrained more tightly by the $C^{34}S$ and CS transitions considered in this work.

The consideration of a disc model with a “puffed-up” inner rim showed that such disc structure is indistinguishable from a standard flared disc model for the transitions and telescope parameters of the observations considered in this work. The ratio between inner rim height and its distance from the central star in Tab. 3.6 also shows that even for the most luminous central star (B1), a disc inclination of $i \geq 72^\circ$ would be necessary to block direct stellar light from an observer only by the inner rim; it is therefore improbable that a high inner disc rim is the cause for the absence of direct starlight noticed in the literature (Hodapp 1984). Taking into account the ratio of disc photosphere height to disc radius in the Appendix A.1, if the outermost disc regions were responsible for the absorption of the central source’s light, disc inclinations of $\leq 60^\circ$ could be sufficient, which is closer to the values obtained from the radiative transfer modelling from $C^{34}S$ but in contradiction to the values from $C^{17}O$ and the fitting of the PV diagrams. Recent simulations (Kuiper & Yorke 2013a) show that the incorporation of optically thick gas inside of the dust sublimation radius may provide effective shielding from the stellar radiation, therefore shifting the inner rim significantly inward – in such a case, the direct light from the central object could be readily blocked by the disc even at lower inclinations than mentioned before.

The disc model used for the radiative transfer calculations in this work is, as outlined earlier, a simplified approach and a range of improvements or extensions are conceivable. Among these are a more sophisticated treatment of the chemical structure than the homogeneous molecule distribution assumed, a more realistic treatment of the physical disc structure (as mentioned before, e.g. the assumptions of gas temperature identical to that of the dust, consideration of only vertical heat transfer in the irradiated disc parts, the use of grey opacities, neglect of dust evolution in the different disc parts are simplified; also for massive discs models taking into account the disc’s self gravitation or non-axisymmetric density distributions may be more realistic), or the inclusion of the effects of an infalling envelope, and of course exploration of a larger parameter space. However, all these are computationally extensive and depend on many poorly constrained parameters like the primordial chemical composition of the material building up the disc, and there is ample discussion in the literature about details of disc structure, of which the form of the inner rim (e.g. Kama

et al. 2009), its location (shifted inward by optical depth of gas inside the dust-free inner region Kuiper & Yorke 2013a) and the effects thereof on the temperature structure of the outer disc regions is only one example.

Moreover, for potential discs around massive stellar objects at typical distances of 1–2 kpc, currently existing observations cannot compete with the spatial resolution reached for protoplanetary discs around low-mass stars at distances of around 100 pc, which allow for an investigation of fine details as even the vertical disc structure (e.g. DM Tau in Dartois et al. 2003). In the case of AFGL 490 presented here, it is unlikely that the two times lower spatial resolution and partially lower signal-to-noise ratio of the $C^{34}S$ and CS data could yield tighter constraints on the possible disc than the previous $C^{17}O$ observations did. Therefore it may be beneficial to limit the physical disc modelling to a computationally less extensive simple power-law structure (e.g. Piétu et al. 2007), possibly including chemical stratification, for the time being and concentrate on obtaining observations of well selected high-density tracers at higher sensitivity and spatial resolution. Such observations are rendered possible for southern-hemisphere massive disc candidates since the advent of ALMA; but similar chances for improvement of observations for AFGL 490 and other northern-hemisphere targets are in reach by the current extension of the PdBI to NOEMA, where a doubling of the number of antennas and extent of baselines is anticipated to significantly improve the spatial resolution and sensitivity of the interferometer within the next few years.

4 Emission of the wider environment – the outflow

4.1. Observations and analysis

In addition to the emission in the immediate vicinity (up to $2''$, corresponding to 2000 au for a source distance of 1 kpc) of AFGL 490, the $C^{34}S$, CS and CH_3OH data sets show emission regions to the north-west and south-east up to a separation of $30''$ (corresponding to 30 000 au) from the central source, while in $C^{17}O$ (Schreyer et al. 2006) no significant emission is discernable at separations $>2''$ from the central source. The emission in the wider environment occurs mostly in form of single clumps, only in the VLA-D array observations of CS(1–0), it appears as more extended emission (Fig. 4.5) – probably because of the lower velocity resolution and sensitivity of the transition to lower density gas. The term “wider environment” here refers to emission up to the edge of the primary beam size of the observations considered in this work and will be discussed in the following chapter. Emission at even larger separations from AFGL 490 has been studied in single-dish observations (Schreyer et al. 2002).

transition. In all of the datasets the region between $2''$ (innermost disc-like emission region) and $4''$ from AFGL 490 appears to be devoid of emission.

An overview of the emission in the wider environment of AFGL 490 for the $CH_3OH(3)$, $C^{34}S$ and CS(D) observations is shown in Fig. 4.1, 4.2 and 4.5, along with spectra of the most prominent emission features.

4.1.1 $CH_3OH(2_0-1_0 E)$, $(2_0-1_0 A^+)$, and $(2_{-1}-1_{-1} E)$

In the $CH_3OH(3)$ data set, a number of clumps with line emission predominantly between -25 and 0 km/s are detected in the wider environment of AFGL 490. The most prominent clumps with clear line emission are numbered in Fig. 4.1 in the order of decreasing peak intensity. The position and sizes of the individual clumps were determined by approximating them with an elliptical Gaussian, the resulting parameters are collected in Tab. 4.1. The accompanying spectra in Fig. 4.1 were obtained by integration within the previously determined elliptical region; grey lines indicate the nominal position of the $CH_3OH(2_0-1_0 E)$, $(2_0-1_0 A^+)$ and $(2_{-1}-1_{-1} E)$ lines for the system velocity -13.4 km/s of AFGL 490. The line parameters were determined by a simultaneous fit of Gaussian line profiles to all three lines using the CLASS package¹. For this, the separation of the three transitions was fixed to their theoretical value and the line width restricted to be the same for all three lines, while v_{LSR} , amount of line width and the line intensities were left free to vary. Where two separate velocity components are discernable like in clumps 2, 3 and 8, both are listed in Tab. 4.1; in clumps 1, 5 and 11 where the association of the lines to a velocity component is ambiguous

¹part of the *Grenoble Image and Line Analysis Software*

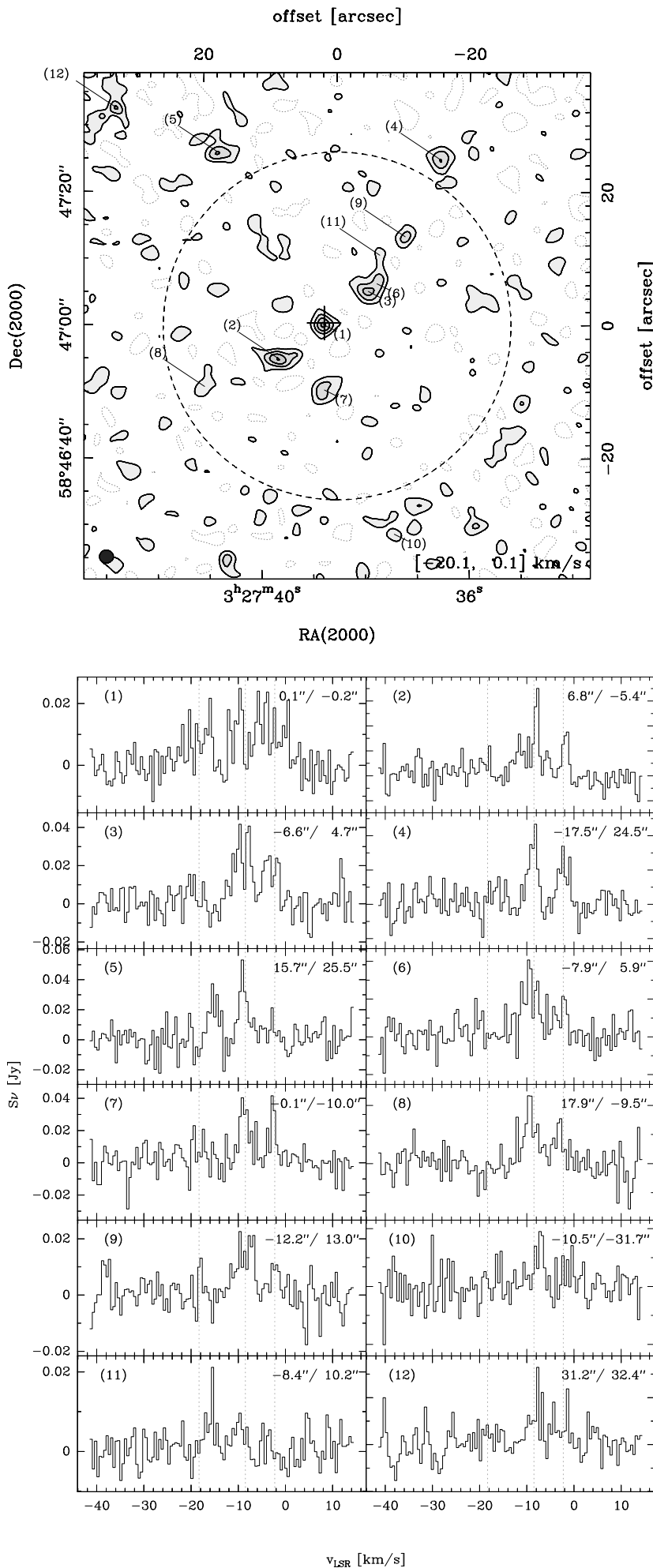


Figure 4.1: $\text{CH}_3\text{OH}(3)$ emission integrated over the velocity range -20.1 to -0.1 km/s. Contours start from 1.5σ ($\sigma = 33$ mJy/beam km/s) and are equally spaced by the same value; negative contours are indicated by dashed lines. The AFGL 490 continuum peak is marked by a cross, the synthesized beam size is indicated in the left lower corner of the panel, the primary beam is outlined by the dashed circle. Emission peaks with presumable lines are numbered, and the spectra integrated over the area of an elliptical gaussian fitted to each peak are shown below (smoothed by a factor of four). In the spectra panels, the offset from AFGL 490 is indicated in the right upper corner, and dotted grey lines indicate the positions of the line triplet for a system velocity of -13.4 km/s.

all conceivable combinations are listed. The individual fits are collected in Appendix A.2. Although there is partially ambiguity in the assignment of the lines to the transitions, there are strong indications for emission from gas clumps with v_{LSR} velocities slightly blue- and redshifted around the AFGL 490 system velocity – ca. $-12.7 \dots -14.6$ km/s – and more strongly blueshifted components – ca. -16.8 and -20 km/s. In clump 12 there are hints of additional narrow lines at -25 , -31 and -40 km/s, which have a separation from each other somewhat too large to consist another blue-shifted line triplet. Noticeably, except for the possible but unsure line combinations 1a and 1b, there is no sign of velocity components significantly (> 1 km/s) redshifted from the AFGL 490 system velocity.

Clumps 4, 5 and 10 are situated slightly outside the half-power primary beam width (where the noise in an image corrected for primary beam attenuation already increases conceivably) but appear to be real detections due to the clearly visible lines. Clump 12 is more arguable since it is located at almost twice the primary beam radius. Clumps 8, 2, 3, 6, 11, 9 and 4 appear to be located along a shallow curve opened towards the north-east, crossing the emission region in the vicinity of AFGL 490. They seem to outline the red lobe of the large-scale outflow of AFGL 490 (e.g. Kawabe et al. 1987; Mitchell et al. 1992).

The positions of the clumps can be well approximated by a parabolic function, where the symmetry axis of the parabola has a position angle of 38_{-4}^{+1} ° and reaches its base point $0.5_{-1.5}^{+0.4}$ '' southwest of the AFGL 490 continuum position, the full opening angle (see equation 4.1) at $r_0 = 10$ '' is then determined as 155_{-17}^{+3} ° (for this, the size of the clumps were taken as limits within which the positions were varied). The clumps 5 and 12 lie roughly along the direction of the symmetry axis, which passes midway between them. In clump 12, hints of more strongly blueshifted lines around $v_{\text{LSR}} = -30 \dots -40$ km/s are visible, but their detection is doubtful due to the position far outside of the primary telescope beam. Otherwise, it could be argued if they represent clumps in the bow shock of a well-collimated jet. However, being located in the red outflow lobe, a redshifted v_{LSR} and a broad velocity distribution would be expected then.

In the $\text{CH}_3\text{OH}(1)$ data set containing the 2_1-1_1 E transition, no clumps with distinct emission lines are visible in the wider environment of AFGL 490, possibly because of the in general low intensity of the $\text{CH}_3\text{OH}(2_1-1_1$ E) line compared to the noise of the observations.

4.1.2 $\text{C}^{34}\text{S}(2-1)$

Similar to the $\text{CH}_3\text{OH}(3)$ data, the emission of $\text{C}^{34}\text{S}(2-1)$ in the wider environment of AFGL 490 occurs in several clumps as is visualized in the integrated intensity image Fig. 4.2, the clumps with clearly detectable line emission are again numbered ordered with decreasing peak intensity. Fits with a gaussian profile to the individual lines yield velocities between -8.4 and -15.3 km/s, i.e. in contrast to the CH_3OH emission, also velocity components redshifted up to 5 km/s from the AFGL 490 system v_{LSR} are observed, while there are no clear signs of the possible -20 km/s component seen in methanol. In clump 1, there is a

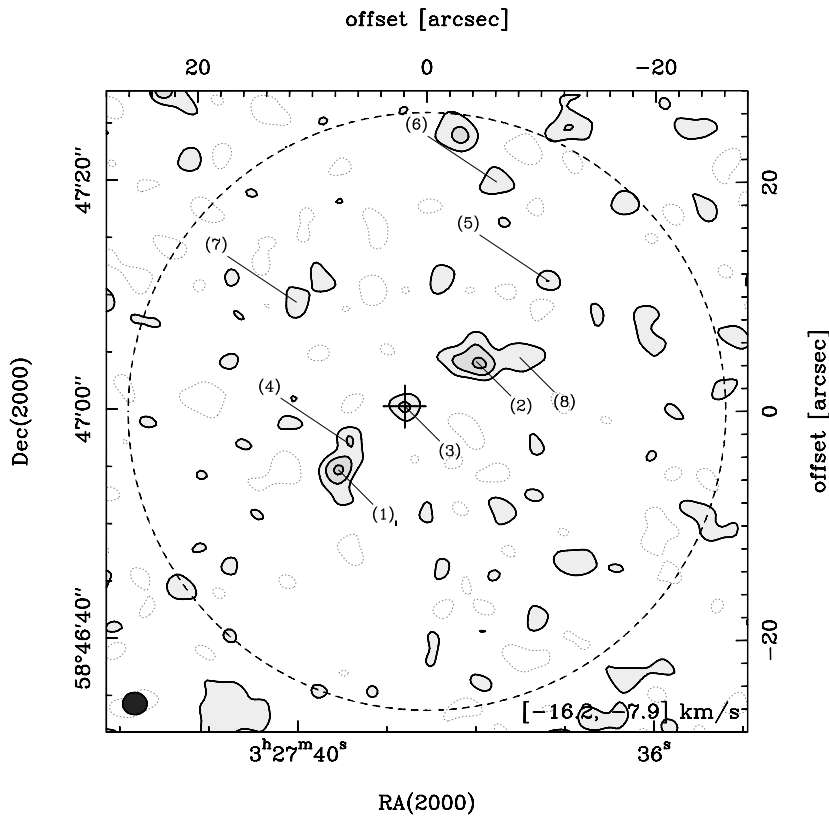


Figure 4.2: $C^{34}S(2-1)$ emission integrated over the velocity range -16.2 to -7.9 km/s. Contours start from 1.5σ ($\sigma = 19$ mJy/beam km/s) and are equally spaced by the same value; negative contours are indicated by dashed lines. The AFGL 490 continuum peak is marked by a cross, the synthesized beam size is indicated in the left lower corner of the panel, the primary beam is outlined by the dashed circle. Emission peaks $>3\sigma$ and with presumable lines are numbered, and the spectra integrated over the area of an elliptical gaussian fitted to each peak are shown below (smoothed by a factor of four). In the spectra panels, the offset from AFGL 490 is indicated in the right upper corner, a dotted grey line indicates the system velocity -13.4 km/s, and small ticks on the ordinate are spaced by 0.01 Jy.

hint of a weak velocity component around $+2$ km/s. As for the CH_3OH data, the most prominent clumps 1, 4, 3, 2 and 8 can be approximated with a parabolic curve, which is however opened to the south-west with a full opening angle at $r_0 = 10''$ of $132_{-17}^{+28}^\circ$ and a base point situated $0.4_{-0.4}^{+0.9}''$ north-west of AFGL 490. The position angle of this parabola, however, with a value of $35 \pm 4^\circ$ agrees remarkably well with that from the CH_3OH data, and is not far from the position angle of the circumstellar disc (first part of this work, Schreyer et al. 2006). The symmetry axis passes close to clump 7.

As in $\text{CH}_3\text{OH}(3)$, the existence of two velocity components almost at the same position is especially evident for the two clumps about $8''$ north-west and south-east of AFGL 490, i.e. along the plane of the disc and perpendicular to the outflow direction (designated as clump 3 and 2 in CH_3OH , clump 1 and 2 in C^{34}S). These positions coincide with the most intense parts of the bar-like structure seen in $\text{CS}(2-1)$ observations by Schreyer et al. (2002). Although the shape of the emission clumps is somewhat irregular, in CH_3OH their longer axes are inclined to the direction of the red outflow lobe, and in C^{34}S toward the blue lobe, in agreement with the aforementioned parabolas.

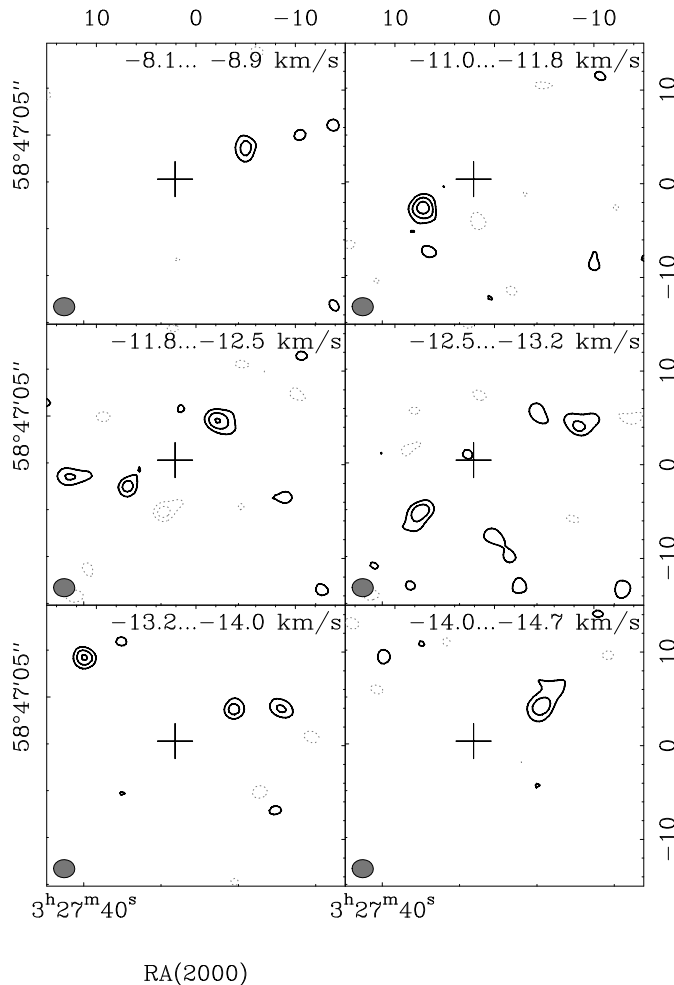


Figure 4.3: Maps of emission integrated over the strongest velocity components visible in the spectra maps of the left panels. Contour lines start at 1.2σ and are equally spaced by the same value; negative contours are indicated with grey dashed lines. The synthesized beam size is indicated in the lower left corner of the panels.

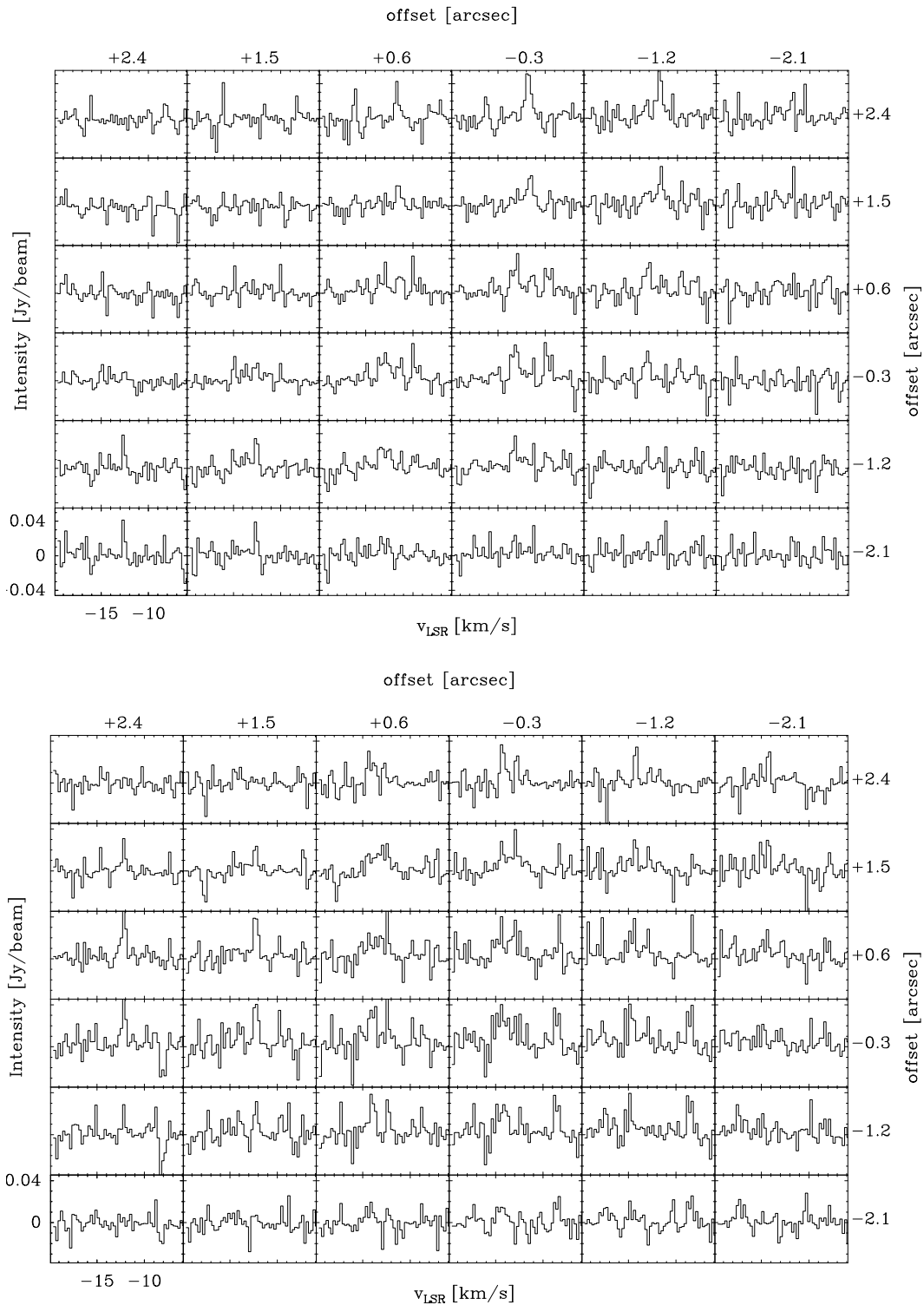


Figure 4.4: Spectra maps of the $C^{34}S(2-1)$ emission in the area of clump 1 (upper panel; south-east of AFGL 490) and clump 2 (lower panel; north-west of AFGL 490); the given offsets are relative to the central clump positions listed in Tab. 4.1.

However, the two velocity components seen in spectra integrated over the whole clump and listed in Tab. 4.1 represent only the strongest components, a closer view on clumps 1 and 2 reveals a more complicated velocity structure. In Fig. 4.4, spectra maps covering the area of clump 1 and 2 are shown – emission in narrow lines around -8 , -10 , -12 , -13 , -14 and -16 km/s are visible. There is, however, no clear pattern discernable in the locations of red- and blueshifted emission in the sense that e.g. emission at one v_{LSR} is located predominantly toward the red or blue outflow lobe, or that there were a velocity gradient visible along the r direction (cf. Fig. 4.9) which could indicate a rotational motion of the outflow system. Instead, the channel maps in Fig. 4.3 and also later for CS(1–0) in Fig. 4.6 indicate a complex structure where emission with different velocities mixes at similar positions perpendicular to the outflow direction.

4.1.3 VLA CS(1–0)

In the VLA-D array observations of CS(1–0), the wider environment of AFGL 490 is dominated by extended emission regions southeast and northwest of the continuum peak; they appear narrow close to AFGL 490 and broaden with increasing distance from the central source, curving away from the line connecting both regions, so that the overall shape seems to outline the cone walls of the large-scale molecular outflow of AFGL 490 (Fig. 4.5).

As for the other transitions, the derived positions of the most intense clumps and line fits to their spectra are collected in Tab. 4.1. Most prominent lines originate from components with velocities of -9.8 to -16.1 km/s, i.e. moderately blue- and redshifted around the AFGL 490 system velocity. Due to the velocity resolution of 0.6 km/s of the CS(D) data, in some clumps there may be additional velocity components which cannot be clearly disentangled (e.g. clumps 2, 17, 18). In clumps 8, 10 and 15 there are hints for an additional component at approximately $+3$ km/s, which is however weak and hence somewhat unsure. As in CH₃OH and C³⁴S, two velocity components at the same position are most obvious along a line perpendicular to the outflow axis, namely in clumps 13, 9, 8 (central region around AFGL 490), and in clump 1 the broad line shows an asymmetric line shape, indicating either a blue wing or the presence of another underlying line component. A line perpendicular to the connecting line through these positions has again a position angle of $40 \pm 5^\circ$, compatible with the position angles of the CH₃OH and C³⁴S parabolas. A comparison of the geometry for all three molecules is given in Fig. 4.7. Although the position angle of the possible disc around AFGL 490 was not well constrained in section 3.1.2, it is roughly perpendicular to the outflow axis obtained here.

A different view on the velocity structure of the large-scale emission in CS(1–0) is given in the channel maps in Fig. 4.6.

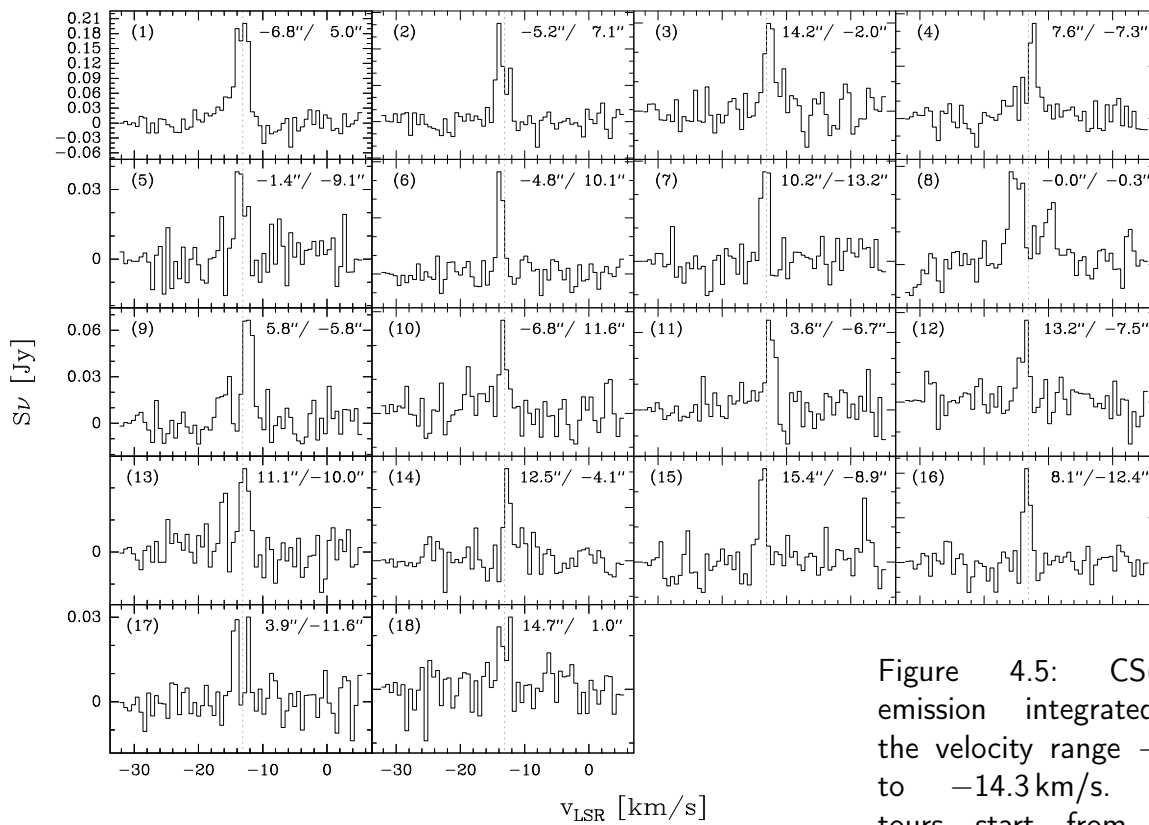
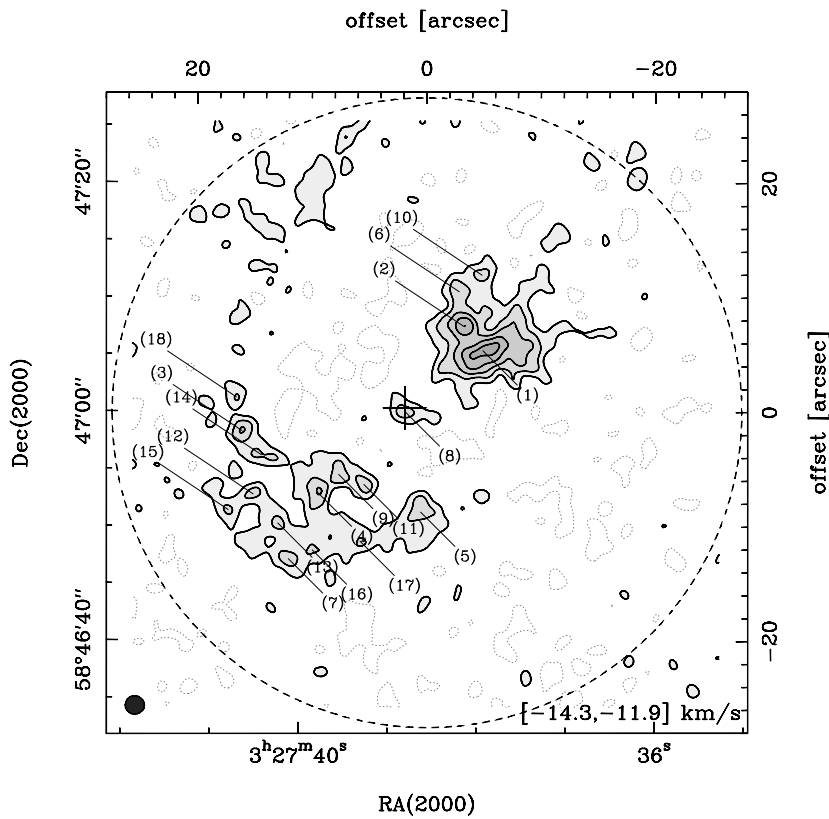


Figure 4.5: CS(1-0) emission integrated in the velocity range -11.9 to -14.3 km/s. Contours start from 1.5σ ($\sigma = 11$ mJy/beam km/s) and are equally spaced by the same value; negative contours are indicated by dashed lines. The AFGL 490 continuum peak is marked by a cross, the synthesized beam size is indicated in the left lower corner of the panel, the primary beam is outlined by the dashed circle. Emission peaks $>3\sigma$ are numbered, and the spectra integrated over the area of an elliptical gaussian fitted to each peak are shown below. In the spectra panels, the offset from AFGL 490 is indicated in the right upper corner, a dotted grey line indicates the system velocity -13.4 km/s, and small ticks on the ordinate are spaced by 0.01 Jy.



The clump south of AFGL 490, nr. 5, which has no counterpart symmetric to the outflow axis and which is also seen as clump 7 in the CH_3OH data, corresponds to the extension already detected in the $\text{CS}(2-1)$ observations of Schreyer et al. (2002) and may be due to an inhomogeneity of the outflow or a denser clump in the line of the south-western outflow lobe.

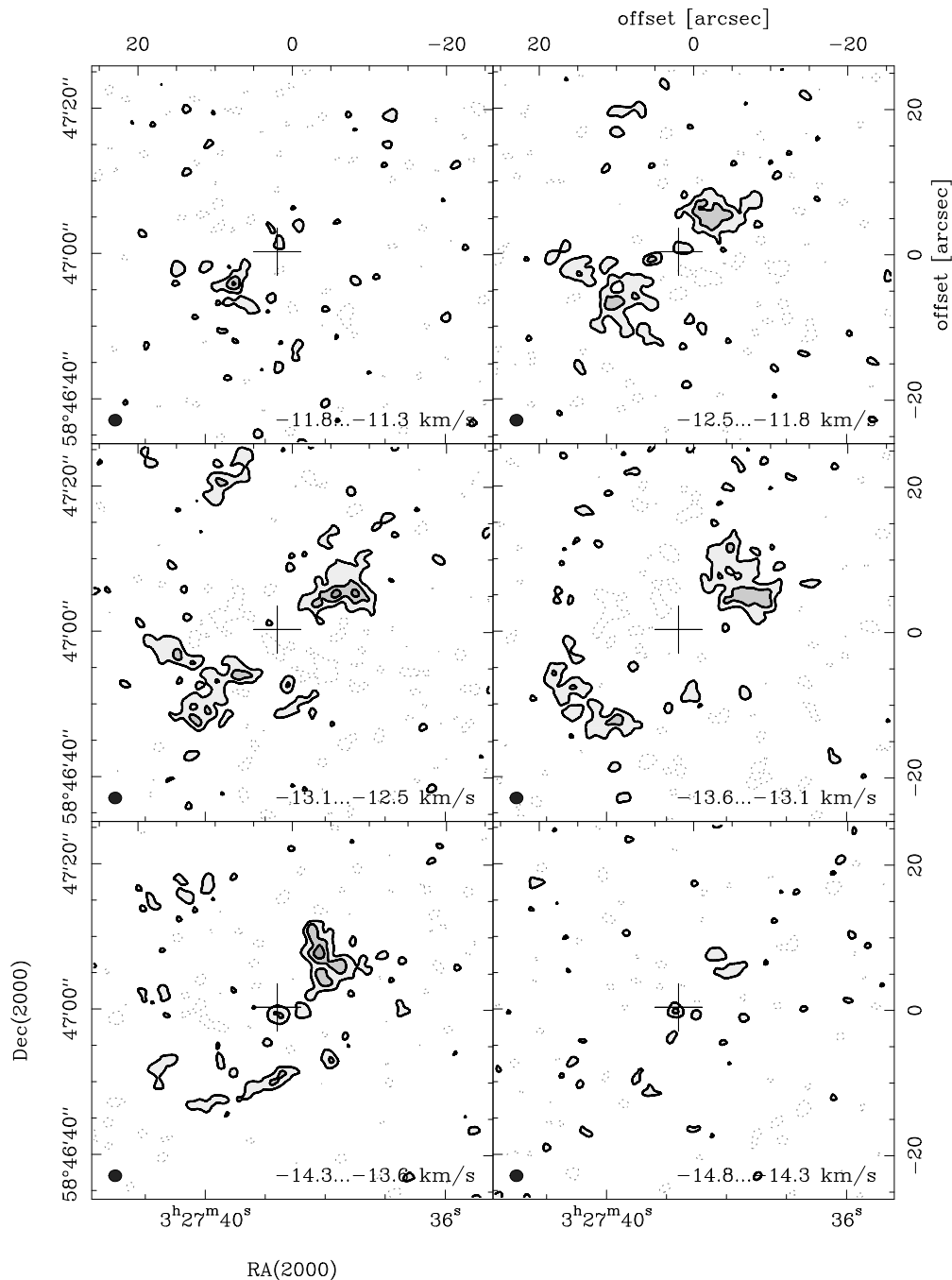


Figure 4.6: Channel maps of the $\text{CS}(1-0)$ emission around AFGL 490 from VLA(D) observations. Contours start from 1.5σ (8.8 mJy/beam and channel) and are equally spaced by the same value. The cross marks the continuum peak position, and the synthesized beam size is indicated in the left lower corner of the panels.

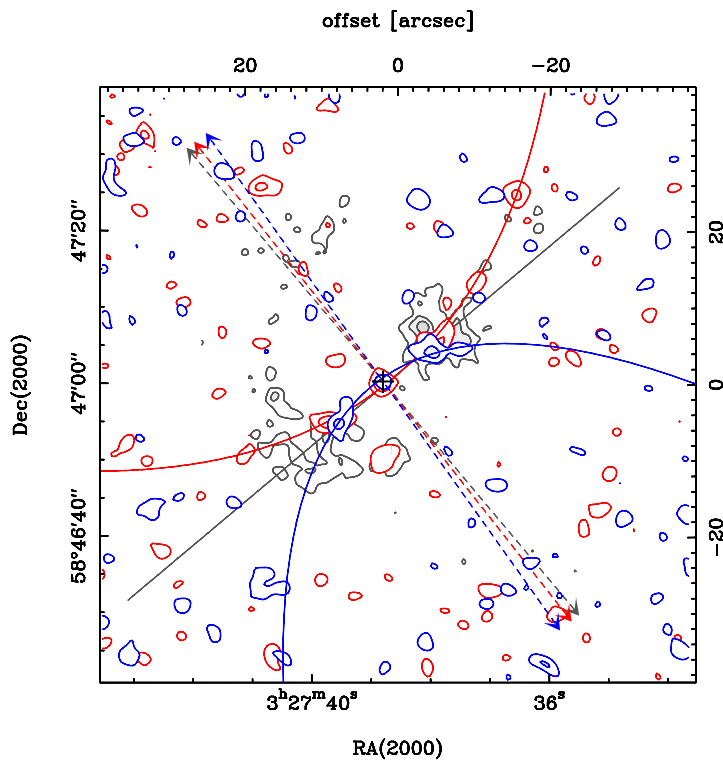
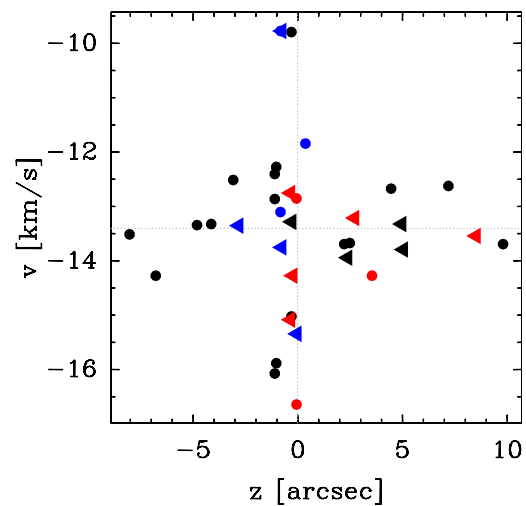
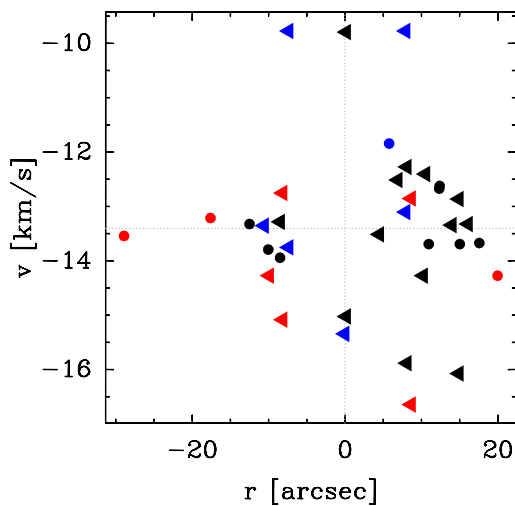


Figure 4.7: Left: CS emission (grey), $C^{34}S$ (blue) and CH_3OH (red) contours (only positive contours, starting at 2σ and spaced by the same value) overplotted with the parabolic curves described in the text. Below: v_{LSR} of line components versus projected distance perpendicular (r) and parallel (z) to the average symmetry axis position angle (38°); colors indicate the transitions as in the left panel. In addition, triangles are used to denote clumps with $r < 0$ in the v versus z plot, and clumps with $z < 0$ in the v versus r plot; circles denote clumps with $r > 0$ and $z > 0$ accordingly.



In the lower part of Fig. 4.7, the (not doubtful) velocity components of all transitions listed in Tab. 4.1 are displayed in a kind of position-velocity diagrams, where the clump positions have been projected on the outflow axis and an axis perpendicular to it (designated as z and r , respectively), assuming the average position angle 38° . In addition, triangles and circles are used to distinguish clumps with $r < 0$ and $r > 0$ in the v versus z plot, and similarly for $z > 0$ / < 0 in the v versus r plot. No distinct velocity gradients are visible, although the scatter of velocities appears to be more pronounced to the north-west of AFGL 490. If the outflow were rotating (hints for rotation have been found e.g. in the outflow of an low-mass young stellar object in Launhardt et al. 2009), one would expect the clumps with $r < 0$ to be more blueshifted than the clumps with $r > 0$ (considering the subset with $z < 0$ and $z > 0$ separately), since a rotation should be inherited from the inner disc and hence in the same direction. However, in Fig. 4.7 no such clear gradient is visible; instead, a large scatter of velocities is found especially for clumps south-west of AFGL 490 ($z < 0$, triangles). The cross-like pattern in the v vs. z diagram shows that the largest blue/redshifts occur in a plane perpendicular to the outflow.

Comparison with other observations of the outflow region

Fig. 4.8 shows the outflow region of AFGL 490 as seen in different observations in the literature. Optical and infrared images show scattered light along the south-western, blue outflow lobe. In single-dish observations, the high-velocity red- and blueshifted components of CO(1–0) trace the molecular outflow mainly along the outflow axis, while HCN(1–0) observations outline the walls of the outflow shells. In comparison, the interferometric observations considered in this work trace only the emission at the very central region of the outflow. The parabolas obtained from the C³⁴S and CH₃OH observations (compare Fig. 4.7) are overlaid on the K' band image of Hodapp (1994) and the outflow walls seen in HCN(1–0) by Kawabe et al. (1987) in Fig. 4.8; they are in good agreement with these observations of the outflow region extending beyond the field of the view of the interferometric observations presented in this work.

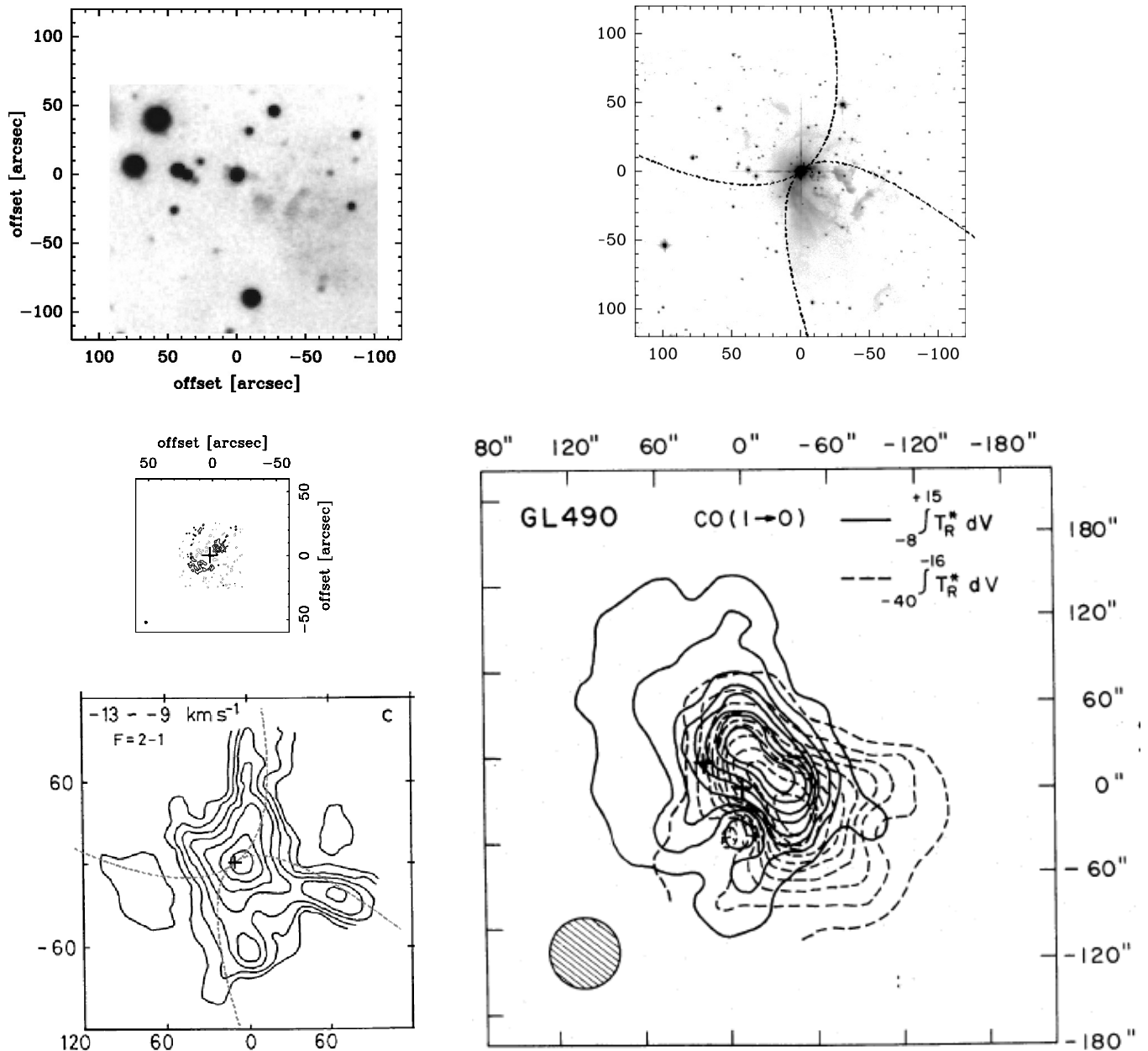


Figure 4.8: Compilation of the outflow region of AFGL 490 as seen at different wavelengths. All panels are shown on the same scale and AFGL 490 is centered at offset (0'',0''). Upper left panel: Combined R , I and z band observations taken at the Jena University Observatory¹. Upper right panel: K' -band image of Hodapp (1994); black dotted lines denote the parabolas obtained from Fig. 4.7. Left middle panel: CS(1-0) emission from the VLA(D-array) observations analysed in this work. Right lower panel: red- and blueshifted CO(1-0) emission, taken from Snell et al. (1984). Left lower panel: HCN(1-0) emission between $v_{\text{LSR}} = -9 \dots -13$ km/s from Kawabe et al. (1987); grey dotted lines denote the parabolas obtained from Fig. 4.7.

¹Observations of 10×3 min in each band were obtained at March 7/8th 2011 with the STK camera at the 0.9 m telescope of the Jena University Observatory (Mugrauer & Berthold 2010). Image reduction was carried out using *IRAF* and included dark and flatfield correction, alignment and summation of the individual frames.

Table 4.1: Properties of the emission clumps in Fig. 4.1, 4.2 and 4.5: position relative to AFGL 490, major and minor axis of an elliptic Gaussian fit to the clumps, and parameters of line fits to the clump spectra (velocity, peak intensity and line width not corrected for instrumental broadening). Uncertainties are given in brackets in units of the last digit of the value. Multiple velocity components are indicated by a second number behind the clump designation; question marks indicate weak or otherwise doubtful velocity components.

Position	RA position offset ["]	Dec position offset ["]	Size [" \times "]	v_{LSR} [km/s]	I [mJy]	Δv [km/s]
CS (1)	−6.847 (19)	4.987 (3)	6.96 \times 4.17(4)	−13.28 (8)	204 (13)	2.6 (2)
CS (2-1)	−5.213 (1)	7.095 (1)	3.09 \times 2.74(1)	−13.94 (5)	83 (7)	1.1 (1)
CS (2-2?)	−5.213 (1)	7.095 (1)	3.09 \times 2.74(1)	−12.1 (3)	\approx 40	...
CS (3)	14.211 (3)	−1.962 (2)	2.63 \times 2.02(3)	−12.62 (13)	29 (4)	2.0 (3)
CS (4)	7.629 (6)	−7.346 (1)	3.57 \times 2.25(1)	−12.40 (9)	53 (6)	1.5 (2)
CS (5)	−1.394 (1)	−9.097 (1)	2.90 \times 2.77(1)	−13.51 (15)	39 (7)	1.8 (4)
CS (6)	−4.786 (7)	10.143 (5)	3.01 \times 2.39(3)	−13.79 (5)	60 (6)	1.0 (1)
CS (7)	10.153 (1)	−13.168 (4)	2.49 \times 1.84(1)	−13.32 (9)	31 (4)	1.3 (2)
CS (8-1)	−0.050 (1)	−0.334 (1)	2.72 \times 1.76(2)	−15.02 (18)	28 (4)	2.7 (4)
CS (8-2)	−0.050 (1)	−0.334 (1)	2.72 \times 1.76(2)	−9.79 (37)	17 (6)	2.3 (9)
CS (9-1)	5.762 (14)	−5.795 (11)	3.72 \times 3.05(1)	−12.27 (9)	76 (8)	1.7 (2)
CS (9-2?)	5.762 (14)	−5.795 (11)	3.72 \times 3.05(1)	−15.88 (23)	25 (6)	2.0 (5)
CS (10)	−6.775 (1)	11.591 (1)	2.20 \times 1.89(1)	−13.32 (11)	25 (5)	1.3 (3)
CS (11)	3.555 (6)	−6.682 (6)	3.13 \times 2.08(5)	−12.51 (11)	35 (5)	1.6 (3)
CS (12)	13.218 (5)	−7.507 (4)	2.89 \times 1.67(2)	−13.69 (14)	23 (4)	1.7 (3)
CS (13-1)	11.075 (12)	−10.038 (16)	2.81 \times 2.11(30)	−12.86 (14)	27 (5)	1.7 (3)
CS (13-2)	11.075 (12)	−10.038 (16)	2.81 \times 2.11(30)	−16.07 (29)	\approx 18	...
CS (14)	12.484 (300)	−4.087 (300)	4.93 \times 1.64(300)	−12.67 (8)	53 (7)	1.1 (2)
CS (15)	15.399 (1)	−8.866 (4)	2.55 \times 2.06(2)	−13.67 (9)	30 (5)	1.1 (2)
CS (16)	8.064 (11)	−12.397 (9)	3.66 \times 2.80(7)	−13.34 (7)	66 (7)	1.2 (2)
CS (17-1)	3.885 (7)	−11.634 (8)	3.66 \times 2.80(7)	−14.27 (7)	41 (28)	0.8 (6)
CS (17-2?)	3.885 (7)	−11.636 (8)	2.89 \times 2.64(4)	−12.20 (14)	30 (5)	0.7 (2)
CS (18-1)	14.691 (4)	0.976 (4)	2.20 \times 1.64(2)	−13.69 (17)	11 (3)	1.4 (4)
CS (18-2?)	14.691 (4)	0.976 (4)	2.20 \times 1.64(2)	−12.2	13	...
C ³⁴ S (1-1)	5.756 (1)	−5.535 (15)	3.00 \times 2.44 (3)	−13.10 (11)	33 (6)	1.1 (2)
C ³⁴ S (1-2)	5.756 (1)	−5.535 (15)	3.00 \times 2.44 (3)	−9.77 (11)	26 (8)	0.8 (3)
C ³⁴ S (2-1)	−6.280 (27)	3.937 (15)	4.22 \times 2.85 (9)	−13.75 (23)	32 (5)	3.0 (6)
C ³⁴ S (2-2)	−6.280 (27)	3.937 (15)	4.22 \times 2.85 (9)	−8.51 (10)	38 (11)	0.7 (2)
C ³⁴ S (3-1)	−0.056 (18)	−0.003 (16)	2.30 \times 1.99 (4)	−15.34 (11)	18 (5)	0.9 (3)
C ³⁴ S (3-2?)	−0.056 (18)	−0.003 (16)	2.30 \times 1.99 (4)	−10.23	40	...
C ³⁴ S (4)	4.792 (20)	−3.270 (25)	2.91 \times 2.21 (7)	−11.84 (6)	41 (6)	0.8 (1)
C ³⁴ S (5)	−12.571 (8)	10.981 (8)	1.95 \times 1.57 (2)	−11.90 (8)	17 (4)	0.7 (2)
C ³⁴ S (6)	−8.046 (29)	19.613 (24)	2.75 \times 2.25 (6)	−12.62 (14)	19 (4)	1.3 (3)
C ³⁴ S (7-1)	9.442 (18)	9.122 (27)	2.91 \times 1.98 (7)	−13.85 (15)	21 (5)	1.4 (3)
C ³⁴ S (7-2?)	9.442 (18)	9.122 (27)	2.91 \times 1.98 (7)	−8.40 (11)	32 (30)	0.3 (5)
C ³⁴ S (7-3)	9.442 (18)	9.122 (27)	2.91 \times 1.98 (7)	−4.24 (7)	26 (8)	0.5 (2)
C ³⁴ S (8)	−10.069 (22)	4.286 (9)	4.50 \times 2.49 (7)	−13.35 (8)	48 (9)	0.8 (2)

Position	RA position offset ["]	Dec position offset ["]	Size [" × "]	v_{LSR} [km/s]	I_3 [mJy]	I_2 [mJy]	I_1 [mJy]	Δv [km/s]
CH ₃ OH (1a)	0.143(17)	-0.214(16)	2.66×2.56(3)	-11.05(10)	16(4)	18(4)	18(4)	1.4(2)
CH ₃ OH (1b)	0.143(17)	-0.214(16)	2.66×2.56(3)	-16.89(8)	25(4)	13(4)	10(4)	1.1(2)
CH ₃ OH (1c)	0.143(17)	-0.214(16)	2.66×2.56(3)	-4.81(12)	...	16(4)	23(4)	1.5(3)
CH ₃ OH (1d)	0.143(17)	-0.214(16)	2.66×2.56(3)	-20.85(11)	25(5)	19(5)	...	1.3(3)
CH ₃ OH (2-1)	6.787(31)	-5.369(14)	4.81×2.36(8)	-12.85(5)	46(8)	77(8)	15(7)	1.0(1)
CH ₃ OH (2-2)	6.787(31)	-5.369(14)	4.81×2.36(8)	-16.64(8)	17(6)	33(7)	11(6)	1.0(2)
CH ₃ OH (3-1)	-6.638(27)	4.747(19)	3.80×2.66(8)	-12.75(14)	27(5)	47(6)	5(5)	1.1(1)
CH ₃ OH (3-2)	-6.638(27)	4.747(19)	3.80×2.66(8)	-15.08(9)	26(4)	32(4)	13(4)	1.8(2)
CH ₃ OH (4)	-17.517(17)	24.497(1)	3.08×2.85(4)	-13.54(11)	27(4)	39(5)	...	2.2(3)
CH ₃ OH (5a)	15.672(25)	25.508(10)	4.36×2.34(9)	-13.91(11)	12(5)	46(6)	...	1.8(3)
CH ₃ OH (5b)	15.672(25)	25.508(10)	4.36×2.34(9)	-20.12(10)	43(5)	30(5)	...	2.1(3)
CH ₃ OH (6?)	-7.948(11)	5.908(17)	4.25×2.36(6)	-14.27(23)	...	29(3)	...	3.9(5)
CH ₃ OH (7)	-0.061(10)	-10.037(3)	4.31×2.93(3)	-13.77(12)	28(5)	37(5)	...	2.2(3)
CH ₃ OH (8-1)	17.933(26)	-9.501(25)	3.43×2.04(8)	-14.27(13)	12(2)	21(3)	...	2.2(3)
CH ₃ OH (8-2?)	17.933(26)	-9.501(25)	3.43×2.04(8)	-17.09(6)	14(5)	19(5)	...	0.5(1)
CH ₃ OH (9a?)	-12.183(28)	12.967(25)	3.24×2.12(7)	-13.21(23)	...	18(3)	3(2)	3.4(5)
CH ₃ OH (9b?)	-12.183(28)	12.967(25)	3.24×2.12(7)	-22.73(14)	12(6)	13(6)	...	0.7(3)
CH ₃ OH (10?)	-8.609(38)	-31.249(28)	3.08×2.25(9)	-12.03(20)	...	16(4)	...	2.0(5)
CH ₃ OH (11a)	-6.429(13)	10.632(21)	2.49×1.58(5)	-20.58(10)	9(3)	15(3)	4(3)	1.2(2)
CH ₃ OH (11b)	-6.429(13)	10.632(21)	2.49×1.58(5)	-14.60(13)	6(3)	11(4)	...	0.9(3)
CH ₃ OH (12?)	33.146(900)	32.816(900)	2.57×2.32(90)	-13.10(30)	9(3)	15(3)	5(3)	3.5(6)
CH ₃ OH (12 ¹)	33.146(900)	32.816(900)	2.57×2.32(90)	-40.16(10)	24(9)	0.5(2)
CH ₃ OH (12 ¹)	33.146(900)	32.816(900)	2.57×2.32(90)	-31.40(22)	19(17)	0.3(3)
CH ₃ OH (12 ¹)	33.146(900)	32.816(900)	2.57×2.32(90)	-25.71(19)	14(8)	0.7(5)

(¹) The fit, i.e. v_{LSR} and line width, refers only to the line for which an intensity is given.

Continuation of Tab. 4.1 for methanol, here the intensities of all three lines CH₃OH(2_0-1_0 E), (2_0-1_0 A⁺) and ($2_{-1}-1_{-1}$ E) are included. Several velocity components at the same position are indicated by additional numbers behind the clump number, letters behind the clump number indicate that there are at least two ambiguous possible v_{LSR} to fit the detected lines, question marks indicate doubtful fits.

4.2. Modelling of the outflow emission

Altogether, the CH_3OH , C^{34}S and CS data seem to outline the densest parts of cones of AFGL 490's large-scale outflow. The mixture of moderately blue- and redshifted velocity components in the most intense clumps $8''$ north-west and south-east of AFGL 490 may be due to an overlap of emission from the blue and red outflow shell along the line of sight. On the other hand, the absence of emission in the region $2\text{--}4''$ from AFGL 490 is reminiscent of hydrodynamical simulations of massive star formation by Krumholz et al. (2009), where gas infalling from the surrounding cloud towards the disc is shocked at the walls of the outflow cavities, and proceeds to accrete onto the disc only through a thin region in the disc plane. In this picture, the dense clumps located about $8''$ north-west and south-east from AFGL 490 could represent the shock regions of the outflow walls, while material travelling inward from there is not detected in the observations until reaching the dense disc $\leq 2''$ from the centre. It would be desirable to use the well detected emission features to derive further constraints on the geometry of the AFGL 490 system.

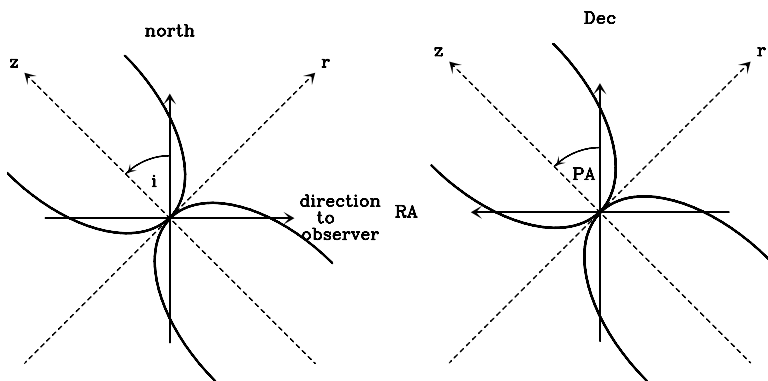


Figure 4.9: Sketch of the outflow model: inclination angle i and position angle PA used to describe the geometry; z and r denote the axes of a cylindrical coordinate system in which z is the symmetry axis of the outflow.

Although molecular outflows are commonly observed accompanying forming stars, the exact formation of their different components and shapes is not yet completely understood, where as sources for the outflow shells wide-angle winds as well as collimated jets are discussed (e.g. Cabrit et al. 1997; Hollenbach 1997). In this work, only a more or less qualitative description of morphology and kinematics is attempted. The typical bipolar outflow consists of two opposing cavities (or outflow cones) with low gas densities formed by the stellar wind. The boundary between the cavities and the more dense, ambient cloud or envelope consists of a relatively thin shell or wall of high density: in the model of Lada (1985), shocked, swept-up material which moves mostly tangential to the shell surface (away from the central star) and with a smaller velocity component perpendicular to the shell towards the ambient cloud, decelerating on its way through the shell. The gas in the wall has a high density and temperature due to shocks, and, in the case of high-mass central stars, can be additionally heated by UV irradiation. The densities and temperatures, as well as the shock origin, may drive a peculiar chemistry (Tafalla & Bachiller 2011; Bruderer et al.

2009). Especially CH_3OH is thought to be released from grain surfaces in shocked gas and therefore may have strongly enhanced gas phase abundances along the outflow walls. Since the aim of this work is only to constrain the geometry and kinematics of the observed outflow emission, the chemistry, excitation and radiative transport of the molecular emission in the outflow shells is not modeled in this work, but a very simplified approach similar to Pety et al. (2006) is applied: the gas is assumed to be isothermal and the molecular emission to be optically thin and proportional to the gas density in the shell, so that the observed intensity distribution is proportional to the density integrated along the line of sight (i.e. column density). A simple Fortran routine was created to model different geometries: a three-dimensional grid (two dimensions in the plane of the sky, one dimension representing the line of sight to the observer) is created, for each grid point the location in a coordinate system rotated by inclination i and position angle PA is calculated and the according model density and radial velocity at this point evaluated. Finally the density is summed up along the z -direction (towards the observer) to create a synthetic map for each radial velocity channel. For comparison with the observed intensities, the maps are convolved with the beam of the observation using the standard task implemented for this purpose in GILDAS. The shape of the outflow shells is usually assumed to be conical (e.g. Pety et al. 2006) or parabolic (e.g. Bruderer et al. 2009). For the case of AFGL 490, the parabolic shells are obviously more suitable, the location of which can be described in a cylindrical coordinate system (z denoting the vertical direction along the outflow axis, and r the radial direction perpendicular to it) as:

$$z = \frac{\pm r^2}{2r_0 \cdot \tan(\theta_0/2)} \quad , \quad (4.1)$$

where θ_0 is the (full) opening angle at an (arbitrary) base distance of r_0 . Here, the shells are assumed to touch in the zero point of the coordinate system. The density in the shell is assumed to decrease linearly with radial distance from the central object (i.e. $\rho \propto (r^2 + z^2)^{-1}$), applying the density gradient found for the envelope by Schreyer et al. (2002). The thickness of the shell Δr in the radial direction is assumed to be constant for all z (inspired by the calculations of Bruderer et al. (2009), where the width of the region heated by FUV irradiation is approximately constant with z). For the convolution, a circular beam of $2''$ size is used to simulate the CH_3OH , C^{34}S and CS observations.

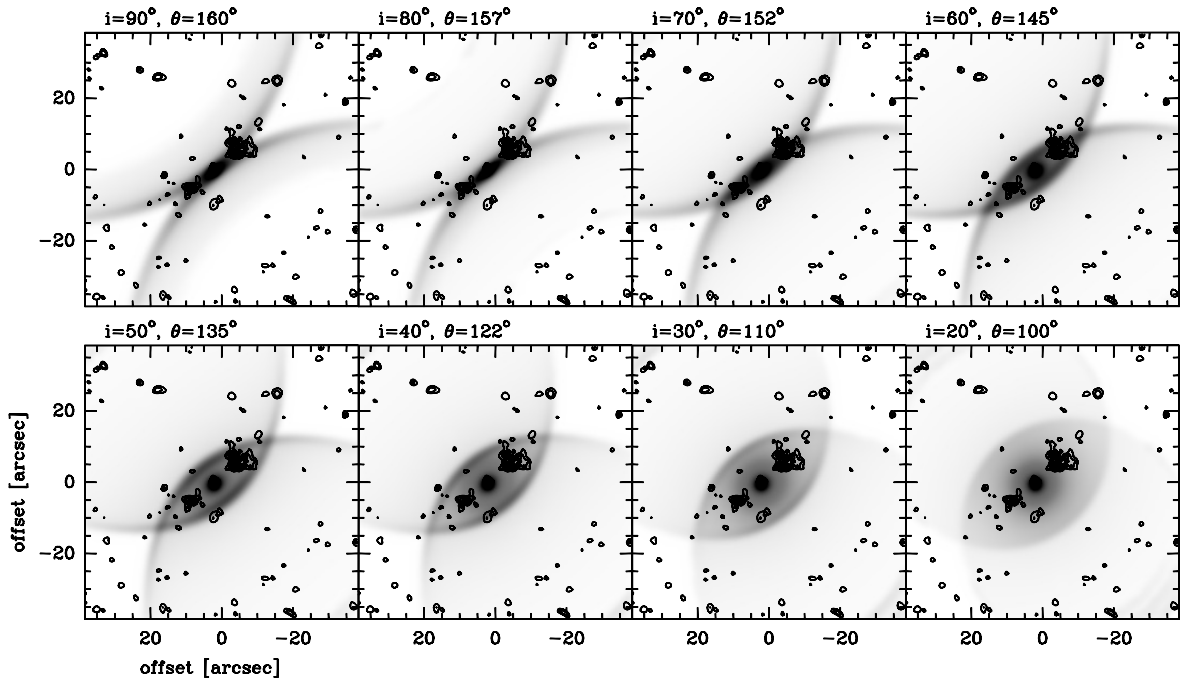


Figure 4.10: Integrated intensity images for an outflow model consisting of two parabolic shells are shown as grey scale image, overplotted with contour lines of CS, $C^{34}S$ and CH_3OH emission (for simplicity, all in the same colour and only positive contours starting at 2.5σ and spaced by the same value). The position angle of the outflow model is 38.8° , the inclination and opening angle (at $r_0 = 10''$, see equation 4.1) are indicated above each panel.

Integrated intensity images (without any assumptions about the velocity structure) for inclination angles $20\text{--}90^\circ$ and overplotted with the contour images of all three observed transitions are shown in Fig. 4.10. The outflow opening angle was chosen such, that the projected shell crosses the most distinct far clump in CH_3OH , clump 4.

In these projected images, for high inclinations of $70\text{--}90^\circ$, all the CH_3OH clumps 8, 2, 3, 6, 11 and 9 (used earlier for the fitting of a parabolic curve) agree well with the shell of the red outflow lobe. At these inclinations, also the innermost $C^{34}S$ and CS clumps fall along the parts of the outflow shells which appear bright in projection (at $70\text{--}80^\circ$, they coincide with the projected crossing point of both shell lobes). For low inclinations of $30\text{--}40^\circ$, the projected outlines of both shells cross in such a way, that the intense CH_3OH clumps 8 and 9, and CS clump 3 lie on the outline of the shell opened to the south-west, and the CH_3OH clump 7, equivalent to CS clump 5, on the outline of the opposite shell. Then the clumps $8''$ from AFGL 490, which are the most intense in all three transitions, fall into the region where both shells overlap in projection – they do not appear brightest in this simulation, however, the assumption of an homogeneous density structure of the outflow wall is very simplified. It may not hold especially for the innermost region, where a lack of shocked gas could be the result of regions almost in the plane of the inner disc being not affected by the outflow mechanism; or the opposite case, the aforementioned scenario where enhanced

emission arises due to an additional shock region where infalling gas meets the outflow walls; or even a mixture of both is conceivable. But in such a case, i.e. if the density were locally enhanced in a ring of e.g. about 8000 au radius in the plane of the disc, it would appear as elliptical ring of emission at low inclinations. Therefore, while in the integrated intensity images the outer, smaller emission clumps would be compatible with either a high-inclination ($70\text{--}90^\circ$) or low-inclination ($30\text{--}40^\circ$) case, the brightest emission clumps of all three transitions at $8''$ separation from AFGL 490 appear to favour high inclinations.

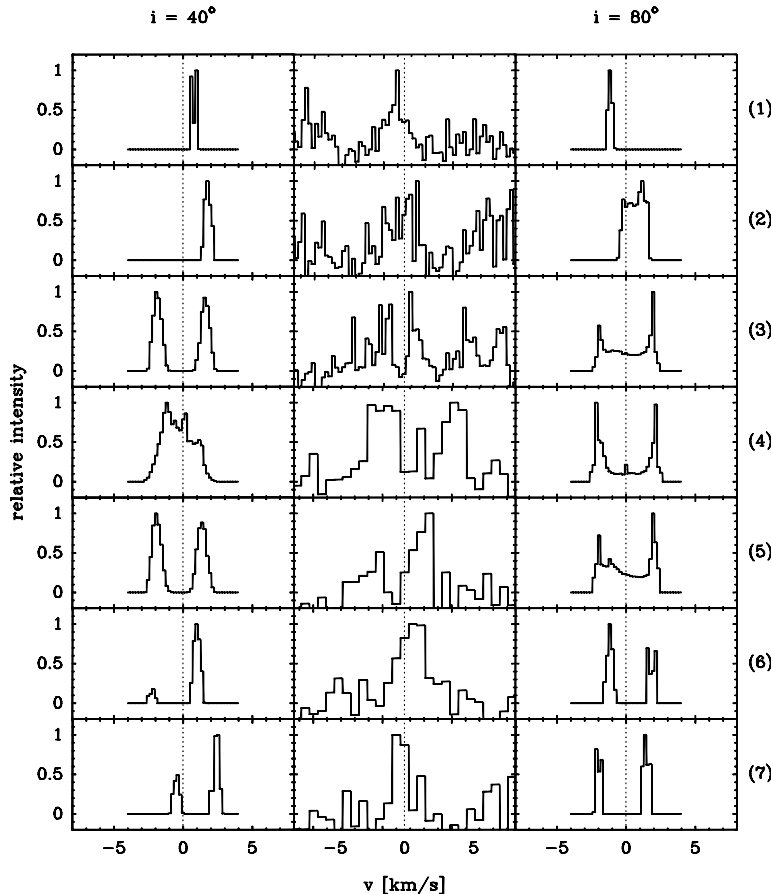


Figure 4.11: Comparison of spectra at selected positions (see text for details). Left row: Synthetic spectra of an outflow model inclined by 40° , middle row: observed spectra ($\text{CH}_3\text{OH}(3)$ in first three panels, CS in the others). Right row: Outflow model inclined by 80° (right). The velocity is given relative to the system velocity (-13.4 km/s for AFGL 490) which is denoted by a vertical dotted line. Note that in the $\text{CH}_3\text{OH}(3)$ spectra, the right third of the panel contains additional lines from the second transition in the data set.

In a second step, the velocity structure of the outflow is taken into account in an attempt to discriminate between the high- and low-inclination case. In general, the velocity at each point in the shell could have components tangential to the shell (v_t), perpendicular to the shell (v_p), and possibly an azimuthal component v_{az} (i.e. tangential and vertical to the curve in the (r, z) plane described in equation 4.2, and the azimuthal component would be perpendicular to this plane) due to rotation of the outflow system. Since there is no sign of rotation detected (Fig. 4.7), the latter two are assumed to be negligible compared to v_t . In a first run, the tangential component is assumed to be constant, $v_t = 2$ km/s, and the intrinsic linewidth is set to 0.1 km/s. For the two cases $i = 40^\circ$ and $i = 80^\circ$, spectra at seven representative positions of the outflow model are compared with the observed ones: (1) one position along the symmetry axis of the outflow toward the red lobe represented by CH_3OH clump 5, (2) a position north-west of AFGL 490 on the outline

of the red lobe shell corresponding to CH₃OH clump 9, (3) the intense emission area 8'' north-west of AFGL 490 corresponding to CH₃OH clump 3, C³⁴S clump 2 and CS clump 1, (4) a position centered at AFGL 490 (CH₃OH 1, C³⁴S 3, CS 8), (5) the intense emission area 8'' south-east of AFGL 490 (CH₃OH 2, C³⁴S 1, CS 4), (6) one position north-east of AFGL 490 on the red lobe corresponding to CS clump 14, (7) the emission region south of AFGL 490 seen in CH₃OH clump 7 and CS clump 5, and (8) a small emission region north-west of AFGL 490 along the blue outflow shell corresponding to CH₃OH clump 9.

A comparison of observed and modelled spectra at these positions is shown in Fig. 4.11. Positions 1, 2, 4 and 8 agree qualitatively with the $i = 80^\circ$ model (however, position 4 seen in CH₃OH exhibits a broad emission peak more resembling to the $i = 40^\circ$ model), position 6 agrees better with the $i = 40^\circ$ model, position 3 and 5 with both (the $i = 40^\circ$ model somewhat better since the region between both lines is almost free of emission), while at position 7 the observations are in contradiction to both models. An perfect agreement is not expected since the observed emission is likely to originate from single clumps rather than the superposition of smoothly emitting outflow shells; this may be especially the case for position 7.

Hence, from this simple model no definite conclusion can be drawn about the inclination angle of the outflow-disc-system either; the most intense emission regions 8'' north-west and south-east of AFGL 490 alone favour somewhat the model with lower inclination of 40° , while for the $i = 80^\circ$ model the spectra at a larger number of positions are qualitatively reproduced.

Additional peculiar emission features

In the CH₃OH(3) data set, a peculiar line profile reminiscent of inverse P Cygni profiles is seen about 1.1'' east and 1.4'' south of the AFGL 490 position, i.e. at the south-eastern edge of the innermost emission region around AFGL 490, where the dominant emission line appears to be accompanied by an absorption component redshifted by ~ 1 km/s. The spectrum of this position without continuum subtraction is displayed in Fig. 4.12. It is not completely clear if this pattern is real, or a spurious feature introduced by the data reduction process (e.g. phase errors), since the "absorption line" dips somewhat below the zero line, but remains above it in most of the region it is observed (about $\pm 0.5''$ around the position of the displayed spectrum).

A similar profile at approximately the same position is seen in the VLA-D array observations of the CS(1-0), but there it extends clearly below the zero line. In the VLA-C array data of the same transition, the quality of the spectra is not sufficient to confirm this pattern. Similar line profiles appear also at other positions in the CH₃OH(3) field of view (Fig. 4.13), namely in the emission region ca. 8'' north-west of AFGL 490 (clumps 3/6), where no continuum emission is detected and the "absorption" lines therefore clearly extends below the

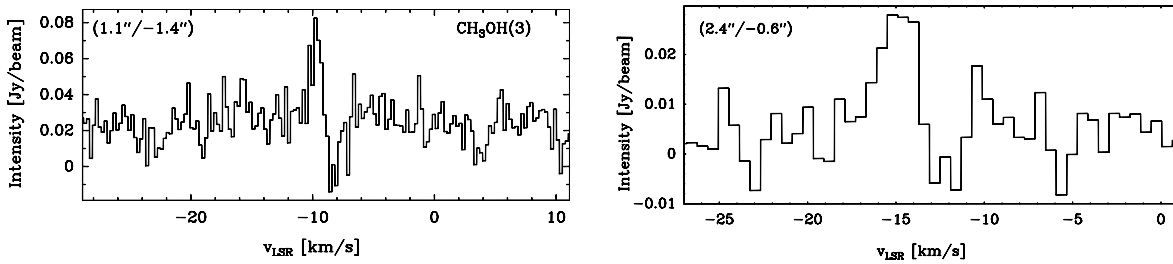


Figure 4.12: Spectra of PdBI $\text{CH}_3\text{OH}(3)$ (upper panel) and CS(1–0) VLA D-array (lower panel) without continuum subtraction, the offset from AFGL 490 is indicated in the upper left corner.

zero line. This could be due either to the "absorption" lines being an artefact, or the extended emission on top of which they appear being resolved out by the interferometer beam. If the lines are no artefact, they could be a sign of cooler material flowing in the direction of AFGL 490 along the line of sight. Since they appear both in direction of the central object and the bright emission regions assigned to the outflow shell, they could originate from envelope infalling envelope material (reminding of the simulations of Krumholz et al. (2009), where infalling material from the envelope is shocked at the location where it reaches the outflow shells). The interpretation that these line profiles are real is supported by the detection of similar profiles in CS in both emission regions south-east and north-west of AFGL 490 associated with the outflow; they are shown in Fig. 4.14.

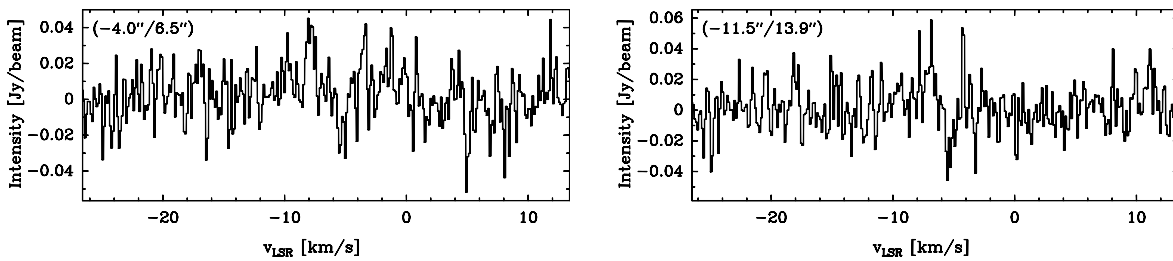


Figure 4.13: Spectra of $\text{CH}_3\text{OH}(3)$ in two clumps along the north-western side of the outflow wall, the offset from AFGL 490 is indicated in the upper left corner.

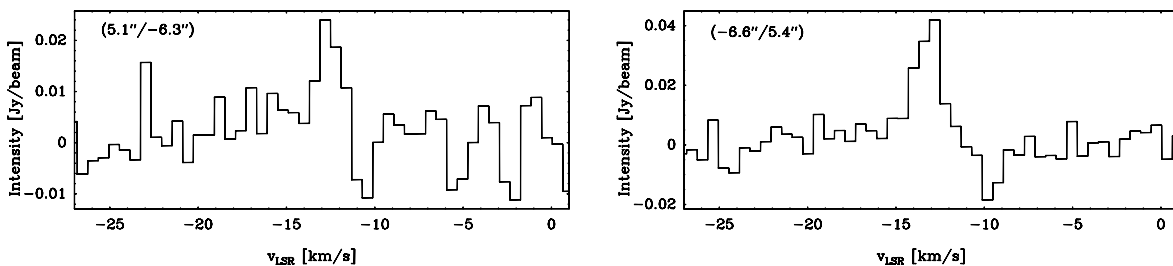


Figure 4.14: Spectra of CS(VLA-D array) in clumps of the outflow region south-east and north-west of AFGL 490; the offset from AFGL 490 is indicated in the upper left corner.

4.3. Summary and discussion

In the wider environment of AFGL 490 (4–30", corresponding to 4000–30000 au for a distance of 1 kpc), the CH₃OH(3), C³⁴S and CS(VLA-D array) observations outline the shells of the large-scale molecular outflow, which is not traced in the earlier C¹⁷O observations of Schreyer et al. (2006). The emission of CH₃OH and C³⁴S occurs in single clumps, where methanol traces predominantly a parabola outlining the north-eastern, red outflow lobe, while C³⁴S is located along a parabola opened toward the south-west, blue outflow lobe. Both observations indicate a opening angle of the outflow of $144 \pm 16^\circ$ (projected on the plane of the sky, at an base distance of 10" from the source). CS(1–0) shows more extended emission not only on the outline of the shells, but also between them. All three molecular line observations yield an position angle of the outflow axis of $38 \pm 7^\circ$, which is roughly perpendicular to the plane of the inner disc. There is no clear sign of rotation visible in the emission assigned to the outflow. Especially the intense emission in two regions south-east and north-west of AFGL 490 are suggested to be parts of the outflow walls or possibly the region where infalling envelope material shocks at the outflow shells, rather than a only a flattened envelope as suspected earlier (Schreyer et al. 2002). Integrated intensity images of a simple model of an outflow consisting of two parabolic shells viewed under different inclination angles provide two possible scenarios for the observed clump locations: a highly inclined outflow (i ca. 80° , with outflow opening angle ca. 160°), where the most intense emission regions 8" south-east and north-west of AFGL 490 are located at the point where the shells start to meet; and a low-inclination case ($i \approx 40^\circ$, opening angle ca. 120°), where the intense emission would originate from a region where both outflow lobes overlap in projection. The low-inclination case would however require a different density structure than the one assumed for the outflow model (smoothly decreasing with increasing distance from the central object), since it suggests strongest emission in two bows north-east and south-west of AFGL 490. Assuming a constant outflow velocity of 2 km/s (constant tangential to the shell, not to the outflow axis), the comparison of observed and modelled spectra favours the high-inclination case by qualitatively reproducing the observed velocity components, while the exact shape of the lines at the most intense emission regions 8" south-east and north-west of AFGL 490 is better represented by the $i = 40^\circ$ model.

In summary, the simple outflow model favours slightly a high inclination of the AFGL 490 disc-outflow-system, but the model may be too simple and the velocity structure of the single emission clumps within the outflow shell too complex to yield a definite conclusion.

5 Summary and outlook

The close ($\leq 30\,000$ au) environment of the young, embedded, intermediate-mass object AFGL 490 was studied by analysis of Plateau de Bure and Very Large Array interferometric observations in $C^{34}S(2-1)$, $CH_3OH(2_{-1}-1_{-1}E)$, $(2_{0-1_0}A^+)$, $(2_{0-1_0}E)$, $(2_{1-1_1}E)$ and $CS(1-0)$.

The observed molecular emission can be divided into two distinct regions: a central region up to radial distances $\leq 2''$ from AFGL 490, and emission in a wider environment separated 4–30'' from the central source.

The innermost emission region, which was interpreted as signature of a rotating gas disc by earlier $C^{17}O$ observations (Schreyer et al. 2006), shows one blue- and one redshifted velocity component located symmetrically about AFGL 490 for each of the observed transitions considered in this work. The orientation of the blue- and redshifted emission is similar to that of the $C^{17}O$ disc for $C^{34}S$, CS and $CH_3OH(2_{1-1_1}E)$ within their large uncertainties, while for the remaining CH_3OH transitions it is almost perpendicular to the aforementioned. An analysis of position-velocity diagrams for CS and $C^{34}S$ favour a Keplerian velocity profile with a low inclination angle ($\approx 30^\circ$) for a central star mass of $8 M_\odot$. In a second step, synthetic spectra were calculated with the line radiative transfer code URANIA (Pavlyuchenkov et al. 2007) for different disc models (with “puffed-up” inner rim and shadowed disc parts following Dullemond et al. 2001, or a standard flared disc model) around a range of central stars (A5–B1). The comparison with the observed spectra suggests intermediate-mass central stars ($6-13 M_\odot$) and discs with moderate inclination ($30-50^\circ$) and shallow surface density profile ($p = -0.5 \dots -1.0$) for $C^{17}O$, while higher disc inclinations ($8-13 M_\odot$, $i = 40-70^\circ$) and steeper surface density profiles ($p = -1.5 \dots -2.0$) are favoured by the $C^{34}S$ observations. The $CS(VLA-D)$ data suggest inclinations up to the maximum considered value of $i = 80^\circ$, but achieve a not acceptable fit, probably because the lines are expected to be optically thick. Concerning the disc radius, the $C^{17}O$ observations suggest a value of 1500–1700 au, while the $C^{34}S(2-1)$ and $CS(1-0)$ data favour a smaller extent of 700–1100 au (for a surface density profile $p = -1.5$), which could point to CS being more concentrated in the inner disc regions than CO .

In the wider environment of AFGL 490, $CH_3OH(3)$, $C^{34}S$ and $CS(VLA-D)$ observations trace presumably the densest parts of the AFGL 490 molecular outflow shells, which was not discernable in the earlier $C^{17}O$ observations of Schreyer et al. (2006). The CH_3OH and $C^{34}S$ emission occurs in single clumps, which can be well approximated with parabolas of a wide opening angle and pointing to an position angle of the outflow axis of $\approx 38^\circ$, close to the position angle of the disc symmetry axis.

A simple model of an outflow consisting of two parabolic shells was employed to attempt a derivation of further constraints on the system's inclination angle, but also here two scenarios with a moderate (ca. 40°) and high (ca. 80°) inclination appear possible, with a slight tendency to the high-inclination case.

Peculiar line profiles reminiscent of inverse P Cygni profiles are detected in $\text{CH}_3\text{OH}(2_0-1_0\text{A}^+)$ and $\text{CS}(1-0)$ both toward the central region ($\leq 2''$ from AFGL 490) and toward two intense emission regions $8''$ south-east and north-west of AFGL 490 presumably associated with the outflow shells. Their appearance in two separate line observations obtained by different telescopes makes them likely real detections; they could be a sign for material infalling from the envelope. No indisputable signs of a collimated jet are detected in the analysed observations.

Altogether, the picture of the possible AFGL 490 circumstellar disc remains somewhat inconclusive from the observations analysed here, and the disc parameters derived for C^{17}O by Schreyer et al. (2006) could not be constrained more tightly by the C^{34}S and CS transitions considered in this work. Especially the question of the system's inclination, which was suggested to be moderate from the C^{17}O observations by Schreyer et al. (2006) and high from the absence of direct stellar radiation by Hodapp (1984), could not be solved definitely neither with the disc nor the outflow models. This ambiguity of the inclination angle translates into an uncertainty of the central stellar objects' mass, for which this work indicates a value of $6-13 M_\odot$ – i.e. at and above the upper limit of intermediate-mass objects, for which only few discs are known.

Modifications and improvements of the adopted simple disc model are desirable for the future, but even more important may be the obtainment of spatially high resolved and sensitive line observations of the disc region – for AFGL 490 and other massive disc candidates. For nearby (~ 1 kpc) objects, typically at the boundary between intermediate and high-mass ($\sim \text{B}2-\text{B}3$, $\leq 10 M_\odot$), present-day interferometers like PdBI and VLA may carry out valuable research, but the expected capabilities of NOEMA and ALMA will allow for a more detailed study of these transitional objects (for a Herbig Ae star, the prospects of ALMA observations are illustrated e.g. in de Gregorio-Monsalvo et al. 2013), and bring into reach discs around truly high-mass objects at larger distance. For AFGL 490 it has been shown that spatially resolved observations of the circumstellar gas disc in optically thin but reasonably intense transitions as $\text{C}^{17}\text{O}(2-1)$ are feasible. Further observations at higher resolution in additional isotopes like ^{13}CO and C^{18}O are desirable to address the details of the disc structure around this advantageously isolated object without signs for a close companion (despite the high multiplicity fraction expected for B type stars, Raghavan et al. see e.g. 2010). The planned increased sensitivity and spatial resolution of NOEMA are especially valuable to study similar interesting disc candidates on the northern hemisphere, e.g. S140-IRS1. ALMA in Cycle 2 configuration and NOEMA may achieve similar physical resolution

of discs comparable to that of AFGL 490 for distances up to ca. 2 kpc, and beyond with full ALMA capabilities - which for the first time brings truly high-mass objects into reach. In addition, the high spatial resolution could allow for constraints on the size of the dust disc from continuum observations, which has not been considered in this work.

Zusammenfassung

Die nahe Umgebung ($\leq 30\,000$ au) des jungen mittelschweren Objektes AFGL 490 wurde mittels Analyse interferometrischer Beobachtungen von Plateau de Bure and Very Large Array in den Übergängen $C^{34}S(2-1)$, $CH_3OH(2_{-1}-1_{-1} E)$, $(2_0-1_0 A^+)$, $(2_0-1_0 E)$, $(2_1-1_1 E)$ und $CS(1-0)$ untersucht.

Die beobachtete Linienemission lässt sich in zwei Bereiche gliedern: einen zentralen Emissionsbereich bis zu einem Abstand von $2''$ zu AFGL 490, und einen Emissionsbereich in der weiteren Umgebung im Abstand von $4-30''$ zum Zentralobjekt.

Der innere Emissionsbereich, der in früheren $C^{17}O(2-1)$ -Beobachtungen (Schreyer et al. 2006) als rotierende Scheibe interpretiert wurde, zeigt in den in dieser Arbeit betrachteten Übergängen jeweils eine blau- und rotverschobene Geschwindigkeitskomponente, die symmetrisch um AFGL 490 positioniert sind. Die Ausrichtung der blau- und rotverschobenen Geschwindigkeitskomponente von $C^{34}S(2-1)$, $CS(1-0)$ und $CH_3OH(2_1-1_1 E)$ ist innerhalb der Unsicherheiten mit der der $C^{17}O$ -Scheibe vergleichbar, während für die restlichen CH_3OH -Übergänge die Ausrichtung nahezu senkrecht zu den zuvor genannten ist. Eine Analyse der Positions-Geschwindigkeits-Diagramme von $CS(1-0)$ und $C^{34}S(2-1)$ legt eine Scheibe mit Keplerschem Geschwindigkeitsprofil und geringer Inklination ($\approx 30^\circ$ für eine Zentralobjekt mit $8 M_\odot$) nahe. Im zweiten Schritt wurden synthetische Spektren mittels des Strahlungstransportprogrammes URANIA (Pavlyuchenkov et al. 2007) für verschiedene Scheibenmodelle (mit erhöhtem inneren Rand und teilweise im Schatten liegenden Scheibenbereichen wie von Dullemond et al. 2001 vorgeschlagen, oder für ein Standardmodell einer sich mit zunehmendem Radius aufweitenden Scheibe) um eine Auswahl verschiedener Zentralsterne (Spektraltyp A5–B1) berechnet. Ein Vergleich mit den beobachteten Spektren legt für bereits von Schreyer et al. (2006) analysierten $C^{17}O(2-1)$ -Beobachtungen, in Übereinstimmung mit deren Ergebnissen, mittelschwere Zentralsterne ($6-13 M_\odot$) und Scheiben mit mittlerer Inklination ($30-50^\circ$) und flachem Oberflächendichteprofil (Exponent $p = -0.5 \dots -1.0$) nahe. Die $C^{34}S(2-1)$ -Beobachtungen deuten dagegen auf höhere Inklinationen ($i = 40-70^\circ$ bei $8-13 M_\odot$) und ein weniger flaches Oberflächendichteprofil ($p = -1.5 \dots -2.0$) hin. Die VLA(D)-Beobachtungen von $CS(1-0)$ hingegen weisen auf noch höhere Inklinationen bis zum betrachteten Maximalwert von $i = 80^\circ$ hin, allerdings wird hierfür keine akzeptable Übereinstimmung von beobachteten und synthetischen Spektren erreicht, was wahrscheinlich auf die optische Dicke dieses Überganges zurückzuführen ist. Für die radiale Ausdehnung der Scheibe legen die $C^{17}O(2-1)$ -Beobachtungen einen Wert von $1500-1700$ au nahe, während die $C^{34}S(2-1)$ und $CS(1-0)$ -Beobachtungen auf einen geringeren Radius von $700-1100$ au (für ein Oberflächendichteprofil mit Exponent $p = -1.5$) hinweisen. Dies könnte ein Hinweis auf eine stärkere Konzentration von CS zu den inneren Scheibenbereichen hin sein.

In der weiteren Umgebung von AFGL 490 zeichnen die CH_3OH -, C^{34}S - und CS -Beobachtungen mutmaßlich die dichtesten Bereiche der Schalen der molekularen Ausströmung von AFGL 490 nach, welche in den früheren C^{17}O -Beobachtungen von Schreyer et al. (2006) nicht sichtbar waren. Die Emission von CH_3OH und C^{34}S tritt in der Form von einzelnen Klumpen auf, deren Lage gut mit Parabeln mit einem weiten Öffnungswinkel angenähert werden kann. Der daraus resultierende Positionswinkel der Ausströmungsachse beträgt $\approx 38^\circ$, was nahe am Positionswinkel der Symmetrieachse der inneren Scheibe liegt.

Ein einfaches Modell einer aus zwei parabolischen Schalen bestehenden Ausströmung wurde verwendet um mögliche weitere Einschränkungen für die Inklination des AFGL 490-Systems abzuleiten. Jedoch erscheinen auch nach diesem Modell zwei Szenarien mit mittlerer (ca. 40°) und hoher (ca. 80°) Inklination möglich, wobei eine Tendenz zur höheren Inklination besteht.

Auffällige Linienprofile, die an inverse P-Cygni-Profile erinnern, sind in $\text{CH}_3\text{OH}(2_0-1_0 \text{A}^+)$ und $\text{CS}(1-0)$ sichtbar, und zwar sowohl in Richtung des zentralen Emissionsbereiches ($\approx 2''$ von AFGL 490 entfernt), als auch in Richtung zweier starker Emissionsbereiche ca. $8''$ südöstlich und nordwestlich von AFGL 490 welche in Zusammenhang mit den Randbereichen der molekularen Ausströmung stehen. Das Auftreten der Linienprofile in zwei verschiedenen Übergängen die mit verschiedenen Teleskopen beobachtet wurden, lässt sie als reale Detektionen erscheinen, die möglicherweise ein Hinweis auf aus der Hülle nach innen fallendes Gas sein könnten. Klare Anzeichen auf einen kollimierten Jet konnten in den betrachteten Beobachtungen nicht gefunden werden.

Zusammenfassend liefern die in dieser Arbeit betrachteten Beobachtungen kein schlüssiges Bild von der möglichen zirkumstellaren Scheibe um AFGL 490, und die von Schreyer et al. (2006) aus C^{17}O -Beobachtungen abgeleiteten Scheibenparameter konnten nicht näher eingegrenzt werden. Insbesondere die Frage des Inklinationswinkels, für welchen die C^{17}O -Beobachtungen von Schreyer et al. (2006) einen mittleren Wert ergaben während die Abwesenheit von direktem stellarem Licht von Hodapp (1984) als Zeichen für einen hohen Inklinationswinkel gewertet wurde, konnte weder mit dem Scheiben- noch dem Ausströmungsmodell endgültig geklärt werden. Diese Uneindeutigkeit der Inklination ist verbunden mit einer unsicheren Bestimmung der Masse des zentralen stellaren Objektes, für welche in dieser Arbeit Werte von $6-13 M_\odot$ abgeleitet wurden – d.h. an der oberen Grenze für mittelschwere Objekte bzw. darüber, ein Massebereich in dem bisher nur wenige Scheiben beobachtet wurden.

Änderungen und Verbesserungen des angewendeten vereinfachten Scheibenmodells sind ein Ziel für zukünftige Arbeit; noch wichtiger erscheinen aber räumlich hochaufgelöste

und empfindlichere Beobachtungen der Scheibenregion – sowohl für AFGL 490 als auch für andere massereiche Objekte mit potentieller Scheibe.

Für nicht zu weit entfernte Objekte (~ 1 kpc), welche typischerweise an der Grenze zwischen mittelschwer und massereich ($\sim B2-B3$, $\leq 10 M_{\odot}$) liegen, können nützliche Beobachtungen mit existierenden Interferometern wie PdBI and VLA erzielt werden. Die erwartete Leistungsfähigkeit von im Bau befindlichen Interferometern wie NOEMA und ALMA werden jedoch eine detaillierte Untersuchung von diesen Übergangsobjekten (für einen Herbig-Ae-Stern werden die Möglichkeiten von ALMA z.B. in de Gregorio-Monsalvo et al. 2013, aufgezeigt), und eine Untersuchung von Scheiben um massereichere Objekte in größerer Entfernung ermöglichen. Für AFGL 490 wurde gezeigt, daß räumlich aufgelöste Beobachtungen von Gas in zirkumstellaren Scheiben in optisch dünnen aber hinreichend starken Übergängen wie $C^{17}O(2-1)$ durchführbar sind. Weitere Beobachtungen bei höherer Auflösung in zusätzlichen Isotopen wie ^{13}CO and $C^{18}O$ sind wünschenswert für eine genauere Untersuchung der Details der Scheibenstruktur um dieses vorteilhaft isoliert liegende Objekt, bei dem es außerdem keine Hinweise auf einen nahen Begleiter gibt (obwohl für Sterne des Spektraltyps B eine hohe Multiplizität erwartet wird, [siehe z.B.] [Raghavan2010]). Die geplante höhere Empfindlichkeit und räumliche Auflösung von NOEMA sind nützlich um interessante potentielle Scheiben um ähnliche Objekte auf der nördlichen Hemisphäre zu untersuchen, z.B. S140-IRS1. NOEMA und ALMA mit der momentanen (Cycle 2) Kapazität könnten ähnliche räumliche Skalen von Scheiben vergleichbar mit der um AFGL 490 für Objekte bis zur Entfernung von 2 kpc auflösen; weiter entfernte Objekte könnten mit der vollen zukünftigen Leistungsfähigkeit von ALMA erreicht werden, was erstmals deutlich massereiche Objekte in Reichweite bringt. Zusätzlich könnte die höhere räumliche Auflösung genutzt werden, um Informationen über die Größe der Staubscheibe zu gewinnen; ein Aspekt der in dieser Arbeit nicht näher betrachtet wurde.

Bibliography

- Alonso-Costa, J. L. & Kwan, J. 1989, *ApJ*, 338, 403
- Alvarez, C., Hoare, M., Glindemann, A., & Richichi, A. 2004, *A&A*, 427, 505
- Andrae, R., Schulze-Hartung, T., & Melchior, P. 2010, *ArXiv e-prints*
- Bell, K. R. & Lin, D. N. C. 1994, *ApJ*, 427, 987
- Beuther, H., Hunter, T. R., Zhang, Q., et al. 2004, *ApJ*, 616, L23
- Bruderer, S., Benz, A. O., Doty, S. D., van Dishoeck, E. F., & Bourke, T. L. 2009, *ApJ*, 700, 872
- C. M. Koepferl, C., Ercolano, B., Dale, J., et al. 2012, *ArXiv e-prints*
- Cabrit, S., Raga, A., & Gueth, F. 1997, in *IAU Symposium*, Vol. 182, *Herbig-Haro Flows and the Birth of Stars*, ed. B. Reipurth & C. Bertout, 163–180
- Campbell, B., Persson, S. E., & McGregor, P. J. 1986, *ApJ*, 305, 336
- Cesaroni, R., Galli, D., Lodato, G., Walmsley, C. M., & Zhang, Q. 2007, *Protostars and Planets V*, 197
- Cesaroni, R., Neri, R., Olmi, L., et al. 2005, *A&A*, 434, 1039
- Chini, R., Henning, T., & Pfau, W. 1991, *A&A*, 247, 157
- Cohen, M. 1975, *AJ*, 80, 125
- Cohen, M. & Kuhl, L. V. 1977, *Publications of the Astronomical Society of the Pacific*, 89, 829
- D'Alessio, P., Canto, J., Calvet, N., & Lizano, S. 1998, *ApJ*, 500, 411
- Dartois, E., Dutrey, A., & Guilloteau, S. 2003, *A&A*, 399, 773
- Davis, C. J., Moriarty-Schieven, G., Eisloffel, J., Hoare, M. G., & Ray, T. P. 1998, *AJ*, 115, 1118
- de Gregorio-Monsalvo, I., Ménard, F., Dent, W., et al. 2013, *A&A*, 557, A133
- Dullemond, C. P., Dominik, C., & Natta, A. 2001, *ApJ*, 560, 957
- Dullemond, C. P., van Zadelhoff, G. J., & Natta, A. 2002, *A&A*, 389, 464
- Dutrey, A., Guilloteau, S., & Guelin, M. 1997, *A&A*, 317, L55
- Dutrey, A., Guilloteau, S., Piétu, V., et al. 2008, *A&A*, 490, L15
- Dutrey, A., Henning, T., Guilloteau, S., et al. 2007, *A&A*, 464, 615

- Ercolano, B., Bevan, A., & Robitaille, T. 2012, ArXiv e-prints
- Flower, D., Rabli, D., & Pineau des Forêts, G. 2012, in European Physical Journal Web of Conferences, Vol. 34, European Physical Journal Web of Conferences, 4001
- Gibb, E. L., Whittet, D. C. B., Boogert, A. C. A., & Tielens, A. G. G. M. 2004, ApJS, 151, 35
- Gómez, J. F. & D'Alessio, P. 2000, ApJ, 535, 943
- Guilloteau, S. & Dutrey, A. 1998, A&A, 339, 467
- Gutermuth, R. A., Megeath, S. T., Myers, P. C., et al. 2009, ApJS, 184, 18
- Haas, M., Leinert, C., & Lenzen, R. 1992, A&A, 261, 130
- Harsono, D., Jørgensen, J. K., van Dishoeck, E. F., et al. 2014, A&A, 562, A77
- Harvey, P. M., Campbell, M. F., Hoffmann, W. F., Thronson, Jr., H. A., & Gatley, I. 1979, ApJ, 229, 990
- Haschick, A. D., Menten, K. M., & Baan, W. A. 1990, ApJ, 354, 556
- Hasegawa, T. I. & Mitchell, G. F. 1995, ApJ, 441, 665
- Henkel, C., Guesten, R., & Haschick, A. D. 1986, A&A, 165, 197
- Henning, T., Pfau, W., & Altenhoff, W. J. 1990, A&A, 227, 542
- Henning, T., Schreyer, K., Launhardt, R., & Burkert, A. 2000, A&A, 353, 211
- Hoare, M. G., Glindemann, A., & Richichi, A. 1996, in The Role of Dust in the Formation of Stars, ed. H. U. Käufel & R. Siebenmorgen, 35
- Hodapp, K.-W. 1984, A&A, 141, 255
- Hodapp, K.-W. 1990, ApJ, 352, 184
- Hodapp, K.-W. 1994, ApJS, 94, 615
- Hollenbach, D. 1997, in IAU Symposium, Vol. 182, Herbig-Haro Flows and the Birth of Stars, ed. B. Reipurth & C. Bertout, 181–198
- Hollenbach, D. J., Yorke, H. W., & Johnstone, D. 2000, Protostars and Planets IV, 401
- Holloway, R. P., Chrysostomou, A., Aitken, D. K., Hough, J. H., & McCall, A. 2002, MNRAS, 336, 425
- Hosokawa, T. & Omukai, K. 2009, ApJ, 691, 823
- Howell, R. R., McCarthy, D. W., & Low, F. J. 1981, ApJ, 251, L21

- Inoue, A. K., Oka, A., & Nakamoto, T. 2009, MNRAS, 393, 1377
- Isella, A. & Natta, A. 2005, A&A, 438, 899
- Jones, T. J., Bryja, C. O., Gehrz, R. D., et al. 1990, ApJS, 74, 785
- Joyce, R. R., Capps, R. W., Gillett, F. C., et al. 1977, ApJ, 213, L125
- Kama, M., Min, M., & Dominik, C. 2009, A&A, 506, 1199
- Kawabe, R., Kaifu, N., Hayashi, S. S., & Hasegawa, T. 1987, in IAU Symposium, Vol. 115, Star Forming Regions, ed. M. Peimbert & J. Jugaku, 352
- Kawabe, R., Ogawa, H., Fukui, Y., et al. 1984, ApJ, 282, L73
- Kennedy, G. M. & Kenyon, S. J. 2009, ApJ, 695, 1210
- Kristensen, L. E., van Dishoeck, E. F., van Kempen, T. A., et al. 2010, A&A, 516, A57
- Krügel, E. 2008, An introduction to the physics of interstellar dust (CRC Press)
- Krumholz, M. R. 2006, in Astronomical Society of the Pacific Conference Series, Vol. 352, New Horizons in Astronomy: Frank N. Bash Symposium, ed. S. J. Kannappan, S. Redfield, J. E. Kessler-Silacci, M. Landriau, & N. Drory, 31
- Krumholz, M. R., Klein, R. I., McKee, C. F., Offner, S. S. R., & Cunningham, A. J. 2009, Science, 323, 754
- Kuiper, R. & Yorke, H. W. 2013a, ApJ, 763, 104
- Kuiper, R. & Yorke, H. W. 2013b, ApJ, 772, 61
- Lada, C. J. 1985, ARA&A, 23, 267
- Lada, C. J. & Harvey, P. M. 1981, ApJ, 245, 58
- Launhardt, R., Pavlyuchenkov, Y., Gueth, F., et al. 2009, A&A, 494, 147
- Leinert, C., Haas, M., Ábrahám, P., & Richichi, A. 2001, A&A, 375, 927
- Leinert, C., Richichi, A., & Haas, M. 1997, A&A, 318, 472
- Leurini, S., Schilke, P., Menten, K. M., et al. 2004, A&A, 422, 573
- Leurini, S., Schilke, P., Wyrowski, F., & Menten, K. M. 2007, A&A, 466, 215
- Low, F. J., Kurtz, R. F., Vrba, F. J., & Rieke, G. H. 1976, ApJ, 206, L153
- Madden, S. C., Irvine, W. M., Swade, D. A., Matthews, H. E., & Friberg, P. 1989, AJ, 97, 1403
- Magnani, L., Sandell, G., & Lada, E. A. 1992, A&AS, 93, 509

- McCall, B. J., Geballe, T. R., Hinkle, K. H., & Oka, T. 1999, *ApJ*, 522, 338
- McGregor, P. J., Persson, S. E., & Cohen, J. G. 1984, *ApJ*, 286, 609
- McKee, C. F. & Ostriker, E. C. 2007, *ARA&A*, 45, 565
- Merrill, K. M. & Stein, W. A. 1976, *PASP*, 88, 874
- Minchin, N. R., Hough, J. H., Burton, M. G., & Yamashita, T. 1991, *MNRAS*, 251, 522
- Mitchell, G. F., Hasegawa, T. I., & Schella, J. 1992, *ApJ*, 386, 604
- Mitchell, G. F., Lee, S. W., Maillard, J.-P., et al. 1995, *ApJ*, 438, 794
- Mitchell, G. F., Maillard, J.-P., & Hasegawa, T. I. 1991, *ApJ*, 371, 342
- Monnier, J. D., Tuthill, P. G., Ireland, M., et al. 2009, *ApJ*, 700, 491
- Morris, M., Palmer, P., Turner, B. E., & Zuckerman, B. 1974, *ApJ*, 191, 349
- Mugrauer, M. & Berthold, T. 2010, *Astronomische Nachrichten*, 331, 449
- Müller, H. S. P., Schlöder, F., Stutzki, J., & Winnewisser, G. 2005, *Journal of Molecular Structure*, 742, 215
- Müller, H. S. P., Thorwirth, S., Roth, D. A., & Winnewisser, G. 2001, *A&A*, 370, L49
- Muller, S., Guélin, M., Dumke, M., Lucas, R., & Combes, F. 2006, *A&A*, 458, 417
- Mundy, L. G. & Adelman, G. A. 1988, *ApJ*, 329, 907
- Nakamura, A., Kawabe, R., Ishiguro, M., et al. 1991, *ApJ*, 383, L81
- Ossenkopf, V. & Henning, T. 1994, *A&A*, 291, 943
- Oudmaijer, R. D., Drew, J. E., & Vink, J. S. 2005, *MNRAS*, 364, 725
- Panagia, N. 1973, *AJ*, 78, 929
- Paraiah, A. 2002, *An Introduction to Radiative Transfer: Methods and applications in astrophysics* (Cambridge University Press)
- Pavlyuchenkov, Y. 2009, private communication
- Pavlyuchenkov, Y., Semenov, D., Henning, T., et al. 2007, *ApJ*, 669, 1262
- Pavlyuchenkov, Y. N. & Shustov, B. M. 2004, *Astronomy Reports*, 48, 315
- Pety, J., Gueth, F., Guilloteau, S., & Dutrey, A. 2006, *A&A*, 458, 841
- Piétu, V., Dutrey, A., & Guilloteau, S. 2007, *A&A*, 467, 163

- Purton, C. R., Lyder, D. A., Gower, A. C., & Belton, D. S. 1995, in *Bulletin of the American Astronomical Society*, Vol. 27, American Astronomical Society Meeting Abstracts, 1318
- Rabli, D. & Flower, D. R. 2010a, *MNRAS*, 406, 95
- Rabli, D. & Flower, D. R. 2010b, *MNRAS*, 403, 2033
- Raghavan, D., McAlister, H. A., Henry, T. J., et al. 2010, *ApJS*, 190, 1
- Rice, W. K. M. & Armitage, P. J. 2009, *MNRAS*, 396, 2228
- Rodriguez, L. F. & Canto, J. 1983, *Rev. Mexicana Astron. Astrofis.*, 8, 163
- Rohlfs, K. & Wilson, T. 1996, *Tools of Radio Astronomy* (Springer-Verlag)
- Sandell, G. 1994, *MNRAS*, 271, 75
- Schmidt-Kaler, T. 1982, *Physical parameters of the stars*, Vol. 2 (Springer)
- Schöier, F. L., van der Tak, F. F. S., van Dishoeck, E. F., & Black, J. H. 2005, *A&A*, 432, 369
- Schreyer, K., Henning, T., van der Tak, F. F. S., Boonman, A. M. S., & van Dishoeck, E. F. 2002, *A&A*, 394, 561
- Schreyer, K., Semenov, D., Henning, T., & Forbrich, J. 2006, *ApJ*, 637, L129
- Semenov, D., Henning, T., Helling, C., Ilgner, M., & Sedlmayr, E. 2003, *A&A*, 410, 611
- Simon, M., Felli, M., Massi, M., Cassar, L., & Fischer, J. 1983, *ApJ*, 266, 623
- Simon, T., Simon, M., & Joyce, R. R. 1979, *ApJ*, 230, 127
- Snell, R. L., Scoville, N. Z., Sanders, D. B., & Erickson, N. R. 1984, *ApJ*, 284, 176
- Stahler, S. W. & Palla, F. 2005, *The Formation of Stars*
- Straizys, V. & Laugalys, V. 2007, *Baltic Astronomy*, 16, 327
- Straizys, V. & Laugalys, V. 2008, *Baltic Astronomy*, 17, 1
- Szymczak, M., Kus, A. J., & Hrynek, G. 2000, *MNRAS*, 312, 211
- Tafalla, M. & Bachiller, R. 2011, in *IAU Symposium*, Vol. 280, *IAU Symposium*, ed. J. Cernicharo & R. Bachiller, 88–102
- Takano, T. 1986, *ApJ*, 303, 349
- Tannirkulam, A., Harries, T. J., & Monnier, J. D. 2007, *ApJ*, 661, 374
- Testi, L. 2004, in *IAU Symposium*, Vol. 221, *Star Formation at High Angular Resolution*, ed. M. G. Burton, R. Jayawardhana, & T. L. Bourke, 161

- Thompson, R. I. & Tokunaga, A. T. 1979, *ApJ*, 231, 736
- van der Tak, F. F. S., van Dishoeck, E. F., & Caselli, P. 2000a, *A&A*, 361, 327
- van der Tak, F. F. S., van Dishoeck, E. F., Evans, II, N. J., & Blake, G. A. 2000b, *ApJ*, 537, 283
- Vinković, D., Ivezić, Ž., Jurkić, T., & Elitzur, M. 2006, *ApJ*, 636, 348
- Walker, R. & Price, S. 1975, *The AFCRL Infrared Sky Survey Vol. I: Catalog of Observations at 4, 11, and 20 Micrometers (AFCRL)*, AFCRL-TR-75-0373, AD A016397, Air Force Cambridge Research Laboratories
- Wang, K.-S., van der Tak, F. F. S., & Hogerheijde, M. R. 2012, *A&A*, 543, A22
- Williams, J. P. & Myers, P. C. 1999, *ApJ*, 511, 208
- Wouterloot, J. G. A., Brand, J., & Fiegle, K. 1993, *A&AS*, 98, 589
- Zapata, L. A., Menten, K., Reid, M., & Beuther, H. 2009, *ApJ*, 691, 332
- Zhang, Q., Hunter, T. R., & Sridharan, T. K. 1998, *ApJ*, 505, L151
- Zinchenko, I., Pirogov, L., & Toriseva, M. 1998, *A&AS*, 133, 337
- Zinnecker, H. & Yorke, H. W. 2007, *ARA&A*, 45, 481

A Appendix

A.1. Radial structure of the model disks

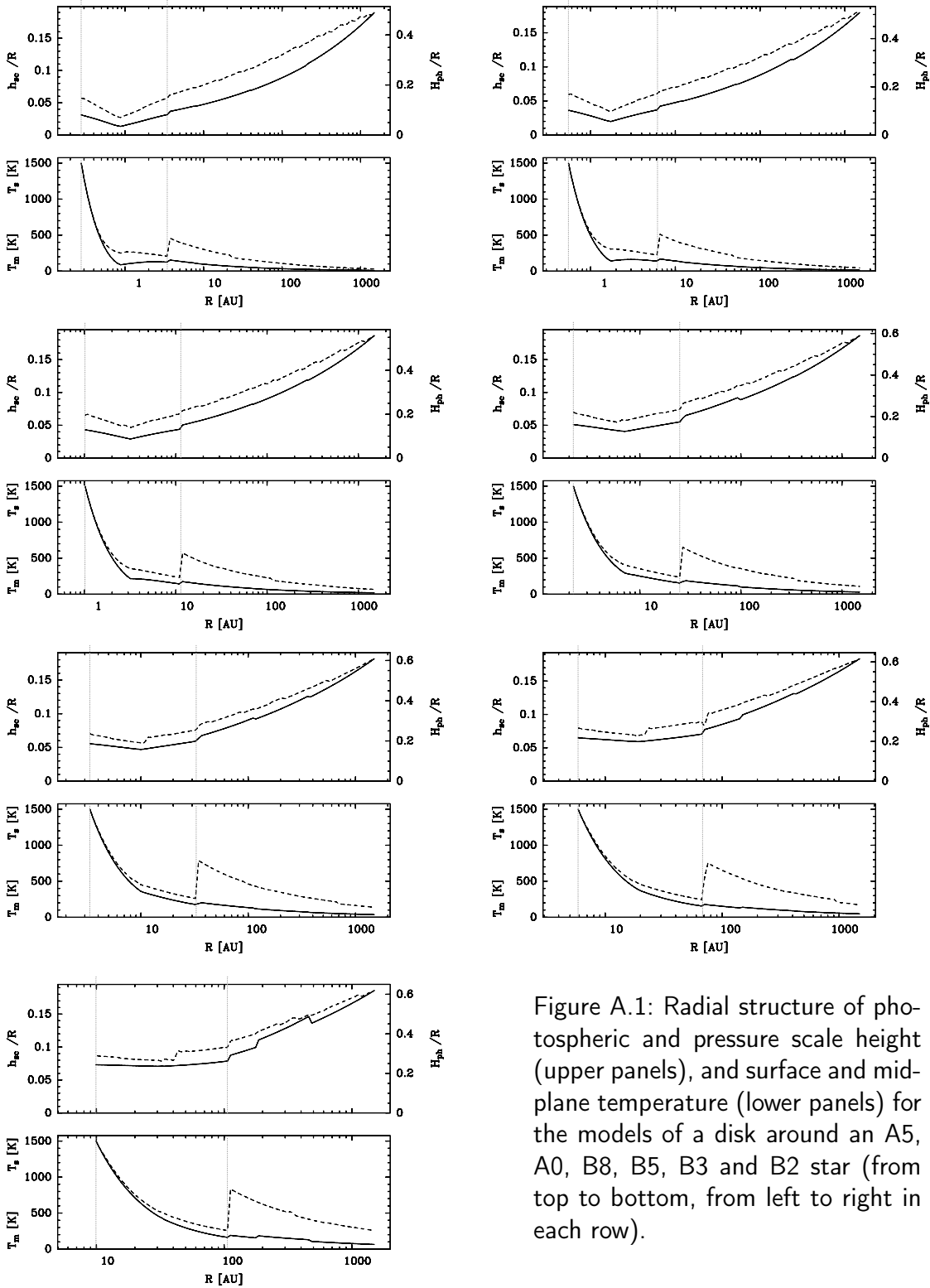
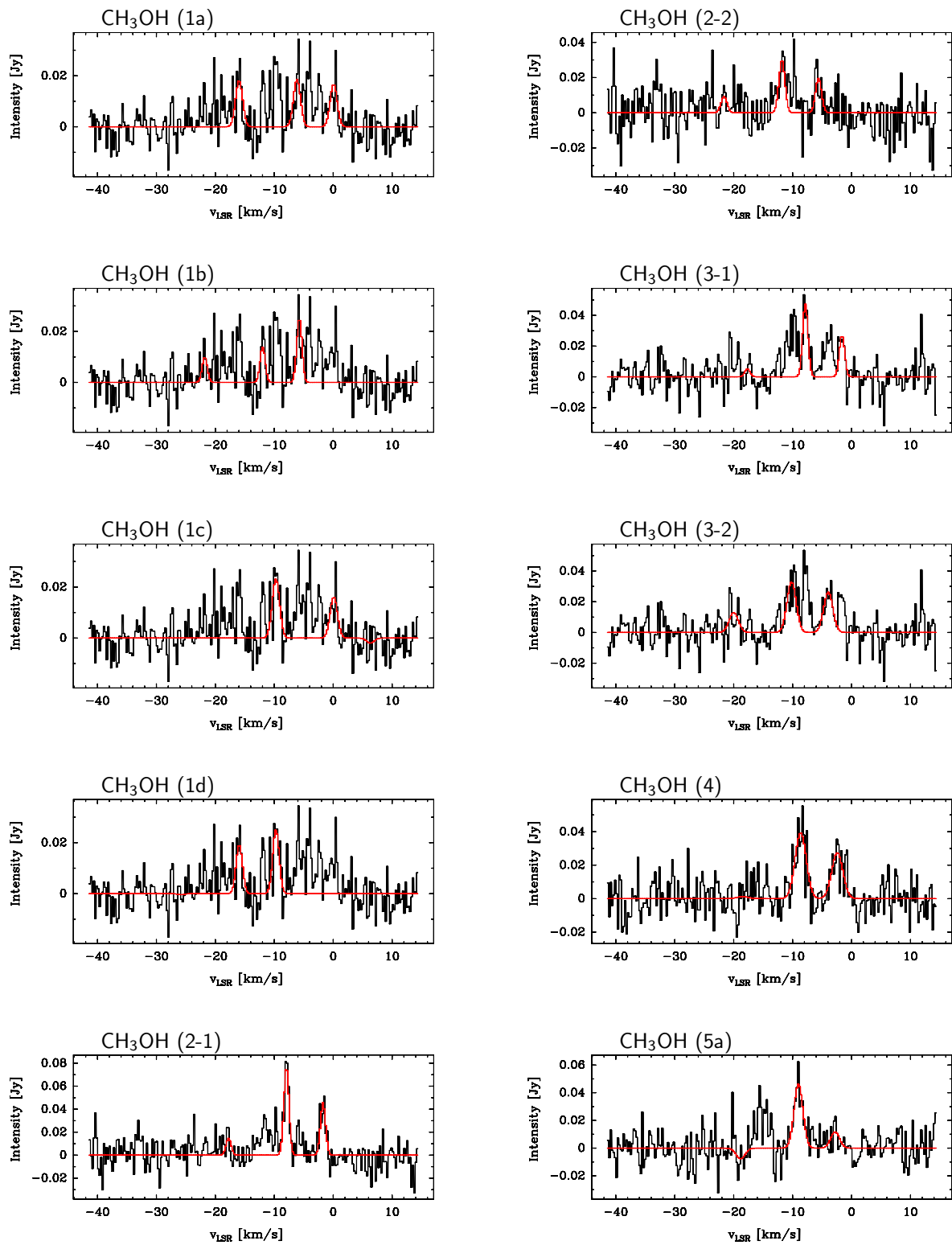


Figure A.1: Radial structure of photospheric and pressure scale height (upper panels), and surface and mid-plane temperature (lower panels) for the models of a disk around an A5, A0, B8, B5, B3 and B2 star (from top to bottom, from left to right in each row).

A.2. Fits of the lines in outflow clumps spectra



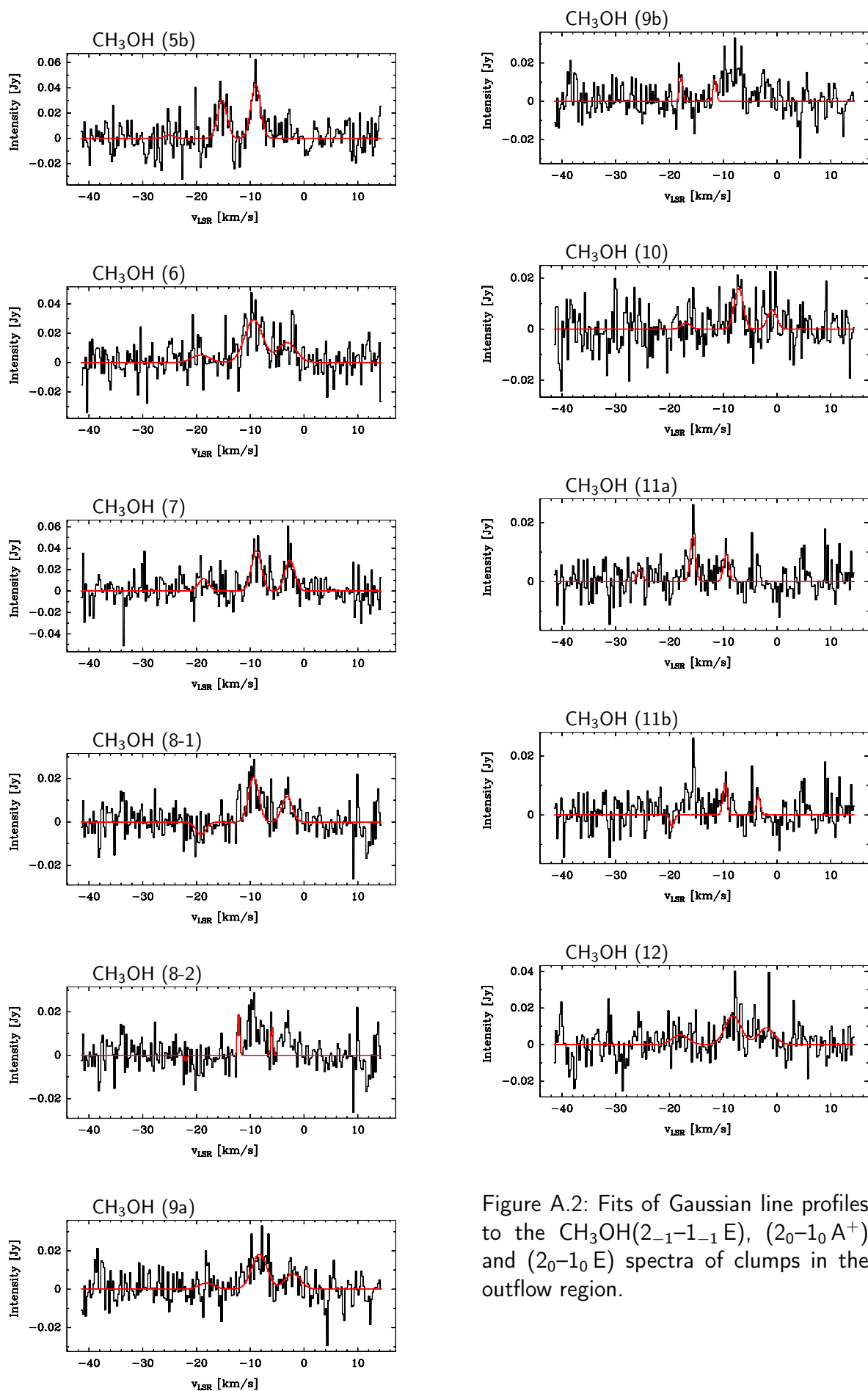
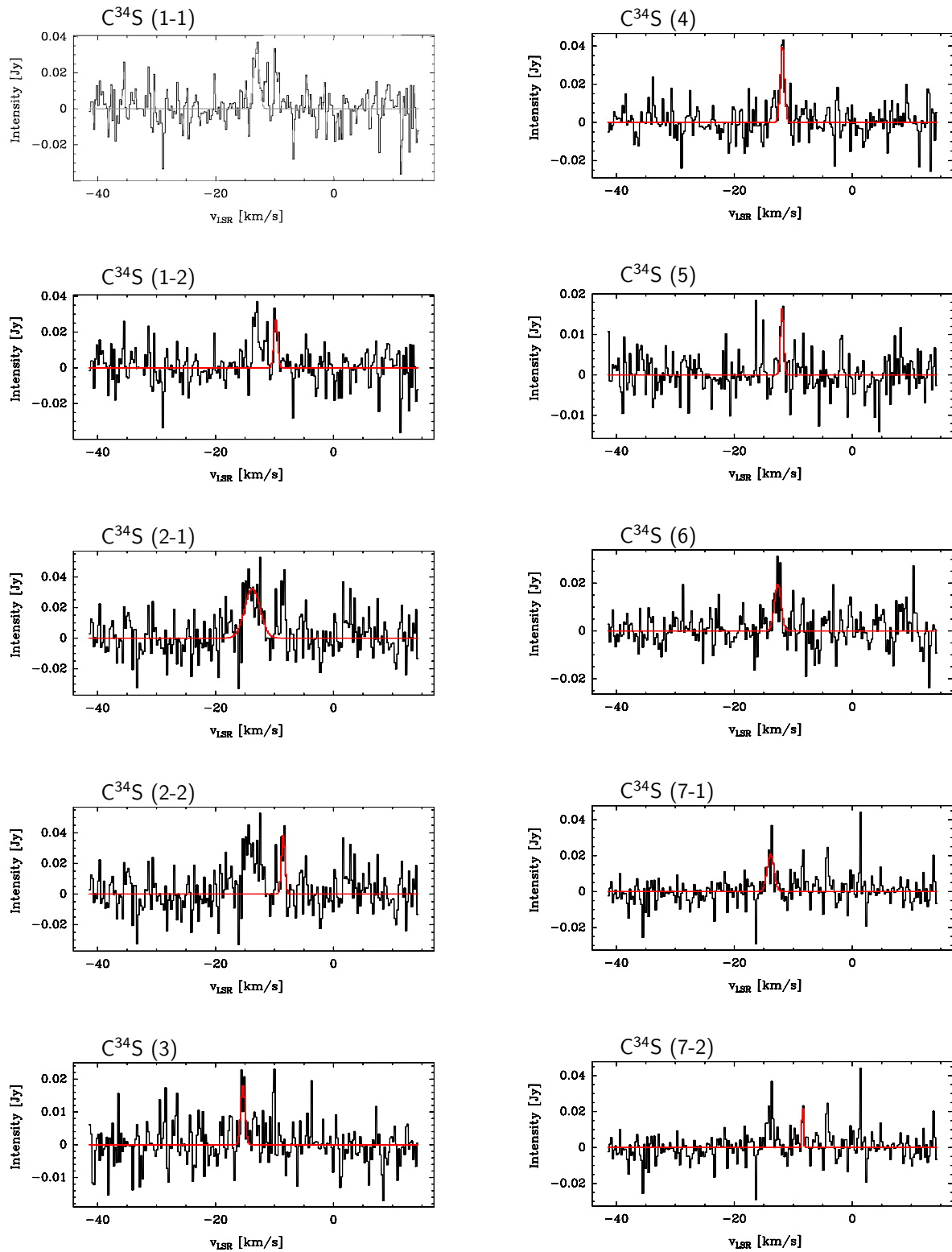


Figure A.2: Fits of Gaussian line profiles to the $\text{CH}_3\text{OH}(2_{-1}-1_{-1} E)$, $(2_0-1_0 A^+)$ and $(2_0-1_0 E)$ spectra of clumps in the outflow region.

Figure A.3: Fits of Gaussian line profiles to the $C^{34}S(2-1)$ spectra of clumps in the outflow (from top to bottom left side and afterward for right side).



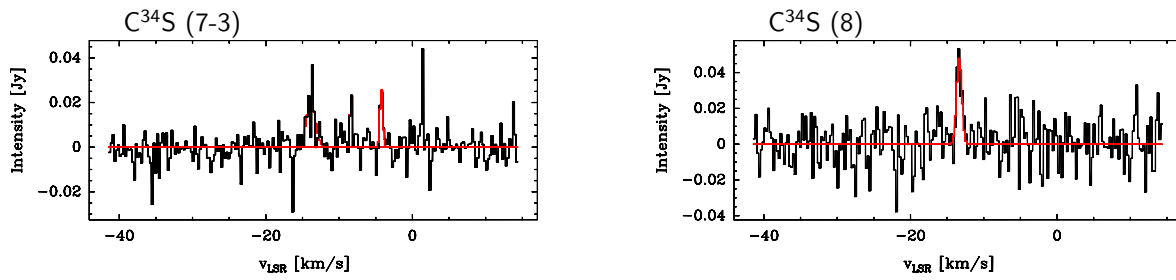
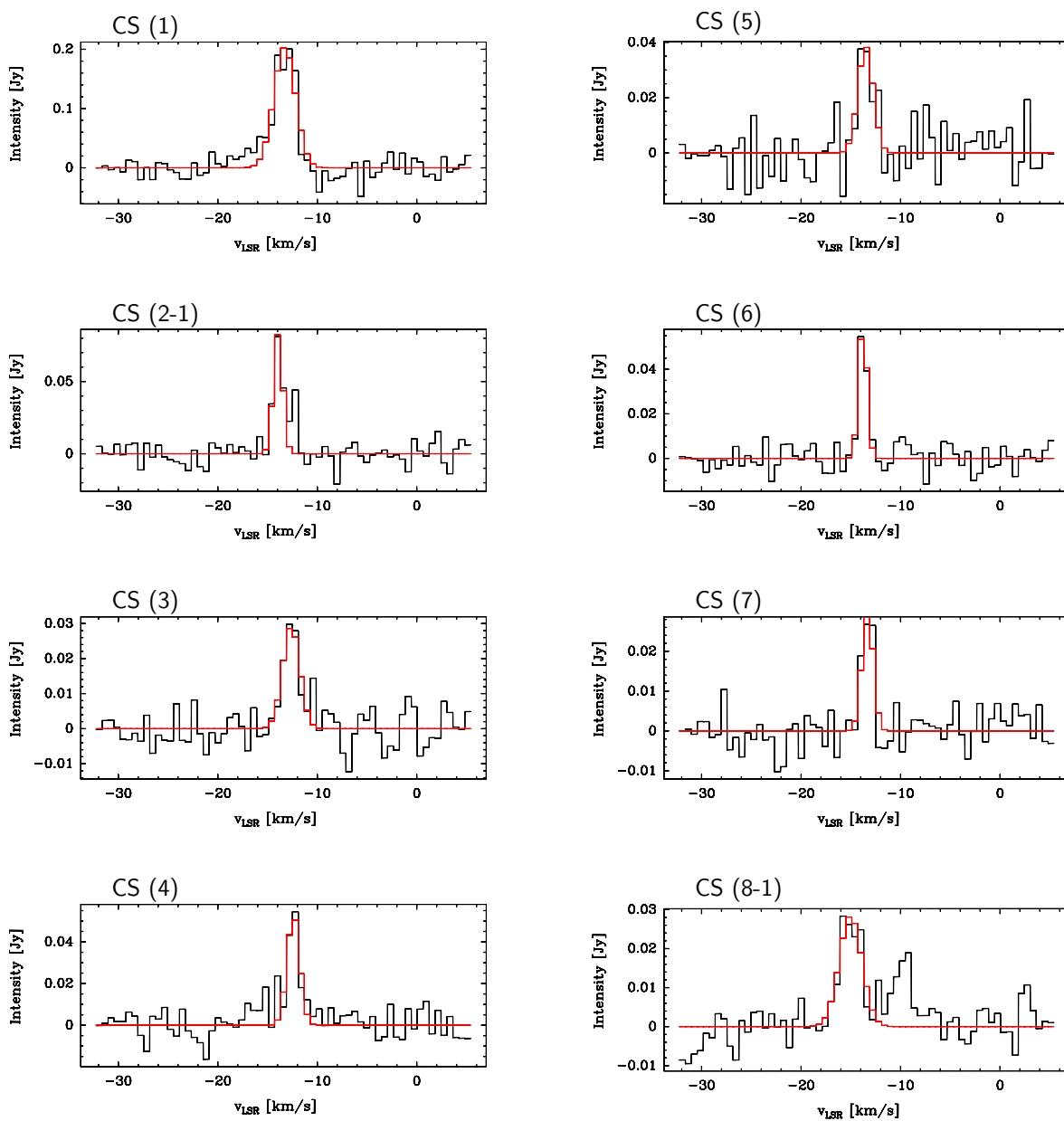
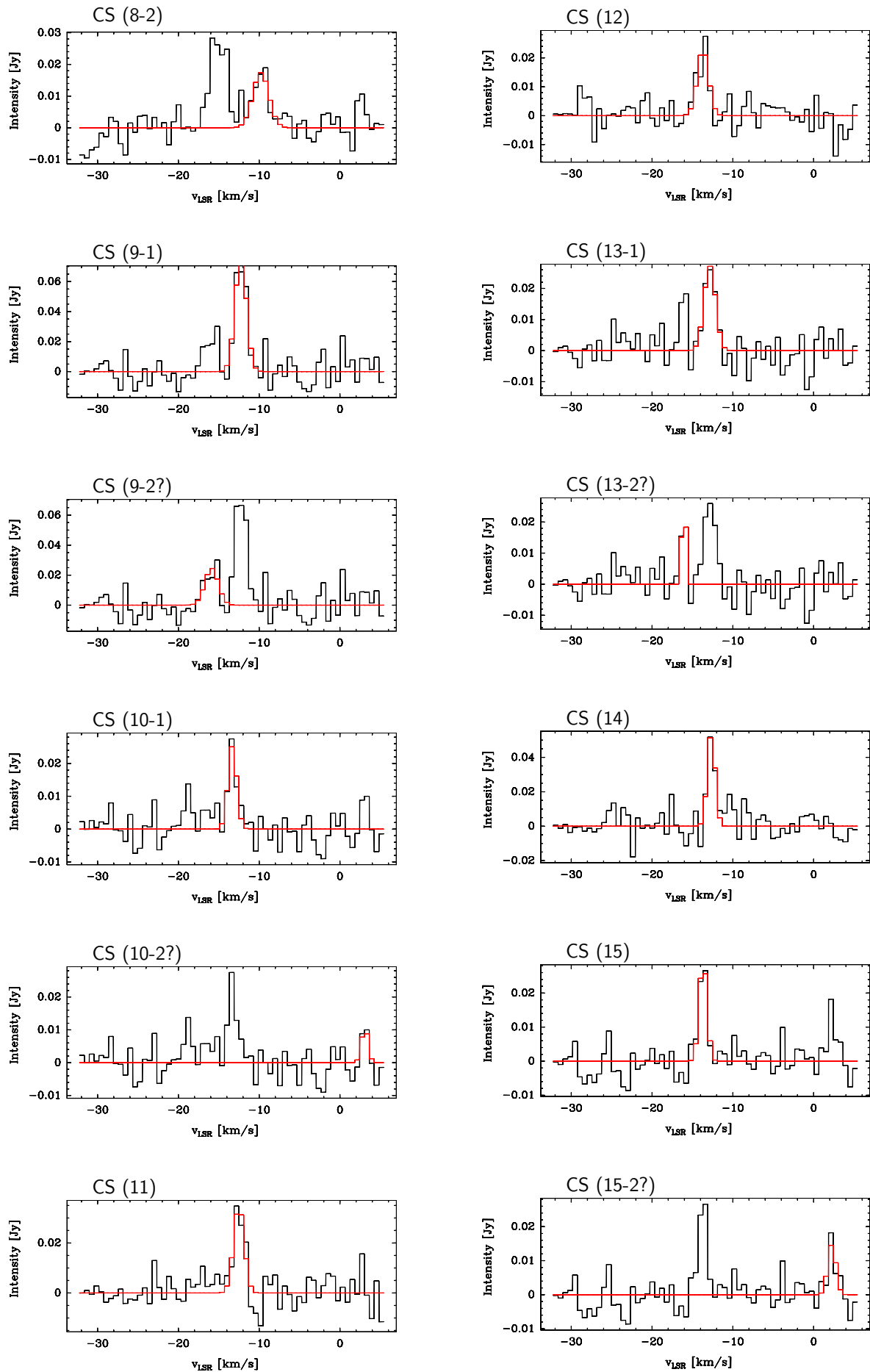
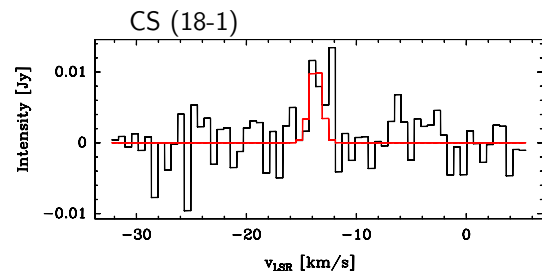
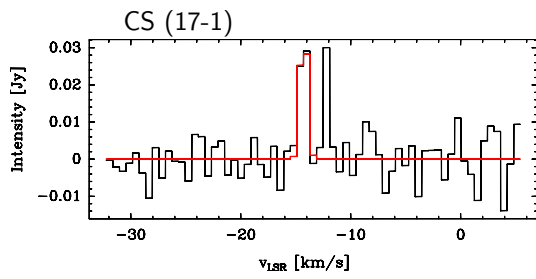
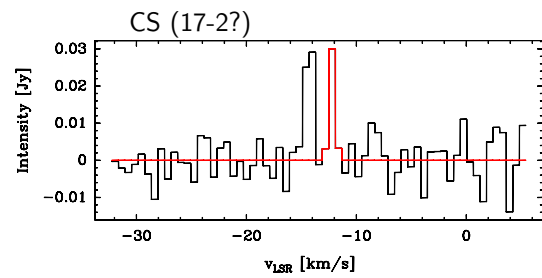
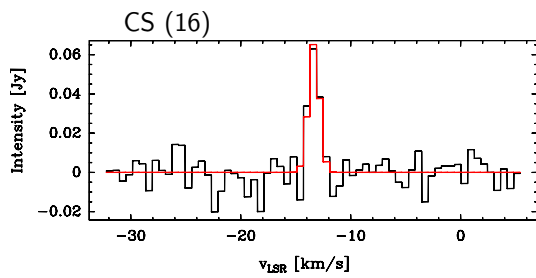


Figure A.4: Fits of Gaussian line profile to the observed CS(1–0) spectra in outflow clumps (from top to bottom left side and afterward for right side).







A.3. Results of the radiative transfer modelling

In the following tables, the results of the comparison between observations and radiative transfer modelling (cf. chapter 3.2) are given: for each central star, the first row lists the difference of χ_w^2 to the minimum value of the table, and the second row the scaling factor f for all considered disc inclinations i . The disc parameters outer radius R_{out} , inner radius R_{in} (if no value is given, then the dust destruction radius is used), disc mass M_{disc} , disc surface density profile exponent p , the considered molecular transition and the minimum χ_w^2 are indicated for each table.

C ¹⁷ O(2-1), $R_{\text{out}} = 1500 \text{ au}$, $M_{\text{disc}} = 1 M_{\odot}$, $p = -0.5$.								
minimum $\chi_w^2 = 2.24936557$								
Star	$i = 10^\circ$	$i = 20^\circ$	$i = 30^\circ$	$i = 40^\circ$	$i = 50^\circ$	$i = 60^\circ$	$i = 70^\circ$	$i = 80^\circ$
A5	2.45E-04	2.40E-04	2.36E-04	2.14E-04	1.98E-04	1.92E-04	1.88E-04	1.92E-04
	0.234	0.703	1.074	1.913	2.578	2.734	3.123	2.969
A0	2.44E-04	2.37E-04	2.16E-04	1.83E-04	1.58E-04	1.54E-04	1.55E-04	1.59E-04
	0.098	0.273	0.546	0.859	1.025	0.996	1.015	1.074
B8	2.44E-04	2.34E-04	1.93E-04	1.31E-04	8.13E-05	5.65E-05	6.37E-05	7.94E-05
	0.059	0.127	0.293	0.459	0.544	0.566	0.527	0.537
B5	2.42E-04	2.17E-04	1.41E-04	6.22E-05	9.30E-06	1.07E-05	4.22E-05	7.68E-05
	0.065	0.166	0.371	0.518	0.571	0.576	0.498	0.468
B3	2.41E-04	2.00E-04	1.02E-04	1.96E-05	0.00E+00	2.57E-05	6.77E-05	1.01E-04
	0.068	0.225	0.430	0.574	0.620	0.571	0.503	0.450
B2	2.38E-04	1.74E-04	5.91E-05	4.77E-07	2.36E-05	6.82E-05	1.03E-04	1.29E-04
	0.093	0.317	0.557	0.684	0.646	0.566	0.518	0.439
B1	2.34E-04	1.34E-04	1.53E-05	1.96E-05	7.49E-05	1.01E-04	1.23E-04	1.42E-04
	0.137	0.479	0.752	0.790	0.713	0.645	0.586	0.498
C ¹⁷ O(2-1), $R_{\text{out}} = 1500 \text{ au}$, $M_{\text{disc}} = 1 M_{\odot}$, $p = -1.0$.								
minimum $\chi_w^2 = 2.24936318$								
A5	2.47E-04	2.42E-04	2.38E-04	2.16E-04	1.99E-04	1.94E-04	1.90E-04	1.98E-04
	0.229	0.623	0.957	1.758	2.362	2.461	2.651	2.646
A0	2.46E-04	2.40E-04	2.19E-04	1.85E-04	1.64E-04	1.59E-04	1.60E-04	1.65E-04
	0.088	0.273	0.566	0.879	1.018	1.014	0.977	1.074
B8	2.45E-04	2.36E-04	1.90E-04	1.29E-04	8.42E-05	5.84E-05	6.56E-05	8.27E-05
	0.068	0.149	0.322	0.507	0.586	0.606	0.580	0.566
B5	2.43E-04	2.16E-04	1.36E-04	6.06E-05	1.29E-05	1.98E-05	5.17E-05	8.13E-05
	0.061	0.200	0.410	0.565	0.632	0.605	0.547	0.508
B3	2.42E-04	1.95E-04	9.56E-05	1.93E-05	1.10E-05	3.72E-05	7.46E-05	1.04E-04
	0.073	0.264	0.474	0.645	0.664	0.603	0.537	0.486
B2	2.39E-04	1.66E-04	5.25E-05	0.00E+00	2.74E-05	7.20E-05	1.08E-04	1.29E-04
	0.107	0.380	0.635	0.751	0.724	0.635	0.581	0.476
B1	2.34E-04	1.24E-04	1.10E-05	1.79E-05	7.18E-05	1.04E-04	1.30E-04	1.44E-04
	0.166	0.547	0.859	0.908	0.782	0.781	0.645	0.586

$C^{17}O(2-1)$, $R_{\text{out}} = 1500 \text{ au}$, $M_{\text{disc}} = 1 M_{\odot}$, $p = -1.5$.								
minimum χ_w^2 2.24938560								
A5	2.24E-04	2.20E-04	2.16E-04	1.94E-04	1.76E-04	1.74E-04	1.68E-04	1.77E-04
	0.234	0.684	0.940	1.880	2.383	2.539	2.695	2.639
A0	2.24E-04	2.17E-04	1.97E-04	1.66E-04	1.49E-04	1.46E-04	1.46E-04	1.51E-04
	0.117	0.293	0.643	0.986	1.172	1.133	1.171	1.177
B8	2.22E-04	2.13E-04	1.65E-04	1.07E-04	6.53E-05	4.82E-05	5.41E-05	7.10E-05
	0.066	0.195	0.415	0.610	0.704	0.742	0.704	0.693
B5	2.20E-04	1.91E-04	1.08E-04	4.43E-05	4.53E-06	1.62E-05	3.70E-05	6.84E-05
	0.087	0.237	0.508	0.667	0.762	0.723	0.668	0.615
B3	2.18E-04	1.67E-04	7.32E-05	8.34E-06	9.06E-06	3.55E-05	6.46E-05	8.80E-05
	0.088	0.342	0.596	0.776	0.782	0.745	0.665	0.587
B2	2.16E-04	1.39E-04	3.93E-05	4.49E-14	2.62E-05	6.68E-05	9.70E-05	1.10E-04
	0.132	0.450	0.752	0.898	0.875	0.746	0.684	0.615
B1	2.10E-04	1.01E-04	4.05E-06	1.96E-05	6.01E-05	9.61E-05	1.22E-04	1.28E-04
	0.205	0.703	1.025	1.094	0.999	0.860	0.743	0.740
$C^{17}O(2-1)$, $R_{\text{out}} = 1500 \text{ au}$, $M_{\text{disc}} = 1 M_{\odot}$, $p = -2.0$.								
minimum χ_w^2 2.24940968								
A5	2.01E-04	1.96E-04	1.90E-04	1.69E-04	1.46E-04	1.35E-04	1.30E-04	1.37E-04
	0.117	0.356	0.664	1.230	1.560	1.755	1.812	1.816
A0	1.99E-04	1.93E-04	1.75E-04	1.45E-04	1.30E-04	1.31E-04	1.29E-04	1.39E-04
	0.156	0.410	0.859	1.328	1.582	1.641	1.583	1.563
B8	1.96E-04	1.82E-04	1.34E-04	6.94E-05	2.15E-05	0.00E+00	5.48E-06	8.58E-06
	0.049	0.107	0.225	0.314	0.356	0.361	0.342	0.390
B5	1.96E-04	1.65E-04	9.16E-05	5.05E-05	2.03E-05	3.67E-05	4.63E-05	7.03E-05
	0.156	0.439	0.850	1.074	1.240	1.216	1.152	1.016
B3	1.93E-04	1.41E-04	7.03E-05	2.62E-05	3.84E-05	6.06E-05	7.27E-05	8.63E-05
	0.171	0.552	0.977	1.206	1.249	1.113	1.074	0.977
B2	1.90E-04	1.21E-04	5.67E-05	3.62E-05	5.63E-05	8.63E-05	1.04E-04	1.06E-04
	0.195	0.742	1.113	1.284	1.201	1.133	1.017	0.997
B1	1.87E-04	9.54E-05	4.22E-05	5.29E-05	7.77E-05	1.11E-04	1.34E-04	1.22E-04
	0.239	0.879	1.307	1.348	1.304	1.152	1.021	1.084
$C^{17}O(2-1)$, $R_{\text{out}} = 1500 \text{ au}$, $M_{\text{disc}} = 0.1 M_{\odot}$, $p = -1.0$.								
minimum χ_w^2 2.24936819								
A5	2.42E-04	2.35E-04	2.30E-04	2.02E-04	1.92E-04	1.78E-04	1.77E-04	1.74E-04
	0.547	2.031	2.813	5.625	6.875	7.827	8.047	8.125
A0	2.41E-04	2.34E-04	2.16E-04	1.83E-04	1.65E-04	1.65E-04	1.63E-04	1.65E-04
	0.391	1.016	1.876	3.555	4.355	4.551	4.844	4.844
B8	2.40E-04	2.33E-04	1.90E-04	1.26E-04	8.70E-05	7.46E-05	8.27E-05	9.97E-05
	0.311	0.703	1.681	2.676	3.186	3.203	3.049	2.947
B5	2.39E-04	2.13E-04	1.34E-04	6.10E-05	1.84E-05	2.96E-05	5.82E-05	9.32E-05
	0.430	1.309	2.783	3.667	4.141	4.141	3.748	3.154
B3	2.38E-04	1.92E-04	9.47E-05	1.93E-05	1.62E-05	4.55E-05	8.42E-05	1.13E-04
	0.547	1.797	3.477	4.683	4.844	4.492	3.896	3.398
B2	2.35E-04	1.64E-04	5.03E-05	1.91E-14	2.93E-05	7.68E-05	1.12E-04	1.32E-04
	0.820	2.891	5.215	5.981	5.957	5.313	4.453	3.823
B1	2.29E-04	1.20E-04	3.58E-06	1.53E-05	7.15E-05	1.06E-04	1.30E-04	1.44E-04
	1.251	4.922	7.578	7.651	7.031	6.099	5.317	4.688

$C^{17}O(2-1)$, $R_{\text{out}} = 700$ au, $M_{\text{disc}} = 1 M_{\odot}$, $p = -1.0$.								
minimum χ_w^2 2.24950933								
B8	9.89E-05	8.94E-05	5.56E-05	2.69E-05	1.84E-05	1.76E-05	1.67E-05	1.98E-05
	0.078	0.196	0.449	0.605	0.645	0.645	0.635	0.662
B5	9.73E-05	7.49E-05	2.62E-05	1.41E-05	8.82E-06	1.43E-05	1.41E-05	2.19E-05
	0.068	0.244	0.449	0.527	0.547	0.547	0.513	0.527
B3	9.54E-05	5.98E-05	1.45E-05	9.30E-06	1.10E-05	1.48E-05	1.93E-05	2.36E-05
	0.079	0.293	0.503	0.547	0.547	0.551	0.510	0.532
B2	9.30E-05	4.08E-05	8.34E-06	0.00E+00	8.58E-06	2.03E-05	3.43E-05	4.15E-05
	0.112	0.366	0.527	0.624	0.605	0.569	0.518	0.527
B1	8.94E-05	2.15E-05	2.15E-06	2.86E-06	1.69E-05	4.67E-05	6.32E-05	6.25E-05
	0.176	0.527	0.684	0.743	0.740	0.621	0.527	0.527
$C^{17}O(2-1)$, $R_{\text{out}} = 900$ au, $M_{\text{disc}} = 1 M_{\odot}$, $p = -1.0$.								
minimum χ_w^2 2.24946618								
B8	1.42E-04	1.32E-04	9.18E-05	4.67E-05	2.98E-05	2.93E-05	3.48E-05	4.32E-05
	0.076	0.166	0.410	0.585	0.635	0.620	0.583	0.605
B5	1.40E-04	1.16E-04	4.74E-05	1.74E-05	1.55E-05	2.38E-05	3.55E-05	4.46E-05
	0.068	0.215	0.460	0.549	0.566	0.537	0.508	0.483
B3	1.39E-04	9.63E-05	2.46E-05	8.58E-06	1.62E-05	2.98E-05	4.10E-05	5.01E-05
	0.081	0.288	0.503	0.576	0.566	0.527	0.518	0.507
B2	1.36E-04	7.22E-05	8.11E-06	2.38E-06	1.91E-05	3.81E-05	4.79E-05	5.87E-05
	0.103	0.381	0.576	0.635	0.645	0.586	0.556	0.547
B1	1.31E-04	3.98E-05	8.44E-15	8.58E-06	2.65E-05	5.39E-05	7.87E-05	8.44E-05
	0.165	0.556	0.747	0.786	0.777	0.664	0.566	0.556
$C^{17}O(2-1)$, $R_{\text{out}} = 1100$ au, $M_{\text{disc}} = 1 M_{\odot}$, $p = -1.0$.								
minimum χ_w^2 2.24941921								
B8	1.89E-04	1.79E-04	1.35E-04	8.18E-05	4.82E-05	4.20E-05	5.25E-05	6.44E-05
	0.078	0.164	0.376	0.547	0.615	0.605	0.585	0.586
B5	1.87E-04	1.61E-04	8.23E-05	3.08E-05	1.72E-05	3.62E-05	5.46E-05	7.37E-05
	0.063	0.205	0.449	0.576	0.583	0.551	0.516	0.488
B3	1.85E-04	1.40E-04	4.70E-05	1.29E-05	2.74E-05	4.96E-05	6.82E-05	8.01E-05
	0.087	0.269	0.508	0.601	0.605	0.551	0.498	0.489
B2	1.83E-04	1.13E-04	1.93E-05	6.91E-06	3.62E-05	6.10E-05	8.15E-05	9.35E-05
	0.093	0.366	0.615	0.665	0.659	0.586	0.522	0.508
B1	1.79E-04	7.13E-05	0.00E+00	2.15E-05	4.82E-05	7.56E-05	1.02E-04	1.10E-04
	0.154	0.562	0.798	0.800	0.781	0.701	0.605	0.547
$C^{17}O(2-1)$, $R_{\text{out}} = 1300$ au, $M_{\text{disc}} = 1 M_{\odot}$, $p = -1.0$.								
minimum χ_w^2 2.24938679								
B8	2.21E-04	2.11E-04	1.66E-04	1.06E-04	6.15E-05	4.70E-05	5.72E-05	7.25E-05
	0.068	0.146	0.342	0.527	0.624	0.601	0.581	0.586
B5	2.19E-04	1.94E-04	1.11E-04	3.98E-05	1.17E-05	2.67E-05	5.48E-05	8.15E-05
	0.073	0.195	0.420	0.566	0.605	0.579	0.527	0.469
B3	2.18E-04	1.71E-04	6.94E-05	1.12E-05	1.38E-05	4.84E-05	8.03E-05	1.01E-04
	0.088	0.266	0.493	0.635	0.627	0.586	0.503	0.468
B2	2.15E-04	1.43E-04	2.96E-05	4.93E-14	3.72E-05	7.25E-05	9.82E-05	1.15E-04
	0.103	0.371	0.647	0.723	0.684	0.605	0.549	0.498
B1	2.11E-04	9.78E-05	4.93E-14	2.22E-05	6.39E-05	9.27E-05	1.18E-04	1.30E-04
	0.151	0.565	0.820	0.821	0.781	0.703	0.587	0.547

$C^{17}O(2-1)$, $R_{\text{out}} = 1700 \text{ au}$, $M_{\text{disc}} = 1 M_{\odot}$, $p = -1.0$.								
minimum χ_w^2 2.24936199								
B8	2.47E-04	2.37E-04	1.91E-04	1.30E-04	8.27E-05	6.15E-05	6.68E-05	8.20E-05
	0.068	0.146	0.349	0.518	0.615	0.635	0.606	0.615
B5	2.46E-04	2.21E-04	1.43E-04	7.15E-05	1.72E-05	6.68E-06	3.39E-05	6.75E-05
	0.068	0.190	0.372	0.542	0.621	0.600	0.552	0.507
B3	2.44E-04	2.01E-04	1.07E-04	3.10E-05	0.00E+00	1.38E-05	5.10E-05	8.56E-05
	0.076	0.254	0.474	0.606	0.684	0.644	0.562	0.499
B2	2.42E-04	1.75E-04	6.99E-05	2.62E-06	1.26E-05	5.05E-05	8.65E-05	1.18E-04
	0.107	0.352	0.620	0.771	0.780	0.684	0.595	0.503
B1	2.37E-04	1.34E-04	2.41E-05	1.22E-05	5.70E-05	9.49E-05	1.23E-04	1.43E-04
	0.166	0.547	0.830	0.905	0.835	0.742	0.645	0.579
$C^{17}O(2-1)$, $R_{\text{out}} = 1900 \text{ au}$, $M_{\text{disc}} = 1 M_{\odot}$, $p = -1.0$.								
minimum χ_w^2 2.24937344								
B8	2.35E-04	2.26E-04	1.81E-04	1.19E-04	7.30E-05	4.98E-05	5.53E-05	7.25E-05
	0.078	0.137	0.361	0.566	0.660	0.684	0.654	0.635
B5	2.34E-04	2.13E-04	1.42E-04	7.80E-05	2.29E-05	4.77E-06	2.03E-05	5.46E-05
	0.063	0.166	0.380	0.503	0.605	0.615	0.564	0.498
B3	2.33E-04	1.94E-04	1.08E-04	4.15E-05	0.00E+00	1.91E-06	2.65E-05	6.13E-05
	0.068	0.244	0.453	0.597	0.684	0.659	0.576	0.508
B2	2.31E-04	1.70E-04	7.72E-05	1.12E-05	4.77E-06	2.17E-05	5.79E-05	8.99E-05
	0.107	0.361	0.591	0.728	0.777	0.740	0.663	0.519
B1	2.26E-04	1.30E-04	3.43E-05	1.24E-05	3.62E-05	6.94E-05	9.78E-05	1.22E-04
	0.186	0.549	0.879	0.938	0.933	0.840	0.713	0.605
$C^{17}O(2-1)$, $R_{\text{out}} = 2100 \text{ au}$, $M_{\text{disc}} = 1 M_{\odot}$, $p = -1.0$.								
minimum χ_w^2 2.24938440								
B8	2.24E-04	2.15E-04	1.70E-04	1.08E-04	6.32E-05	4.01E-05	4.70E-05	6.06E-05
	0.076	0.166	0.386	0.581	0.703	0.734	0.684	0.674
B5	2.24E-04	2.05E-04	1.38E-04	7.77E-05	3.03E-05	4.77E-06	2.10E-05	5.36E-05
	0.063	0.176	0.378	0.493	0.586	0.596	0.547	0.488
B3	2.23E-04	1.88E-04	1.06E-04	5.10E-05	8.34E-06	4.04E-14	1.81E-05	5.13E-05
	0.073	0.249	0.468	0.586	0.655	0.656	0.605	0.518
B2	2.21E-04	1.66E-04	8.06E-05	2.57E-05	1.24E-05	1.17E-05	3.50E-05	6.68E-05
	0.115	0.352	0.586	0.747	0.762	0.741	0.663	0.555
B1	2.17E-04	1.28E-04	4.58E-05	2.26E-05	2.81E-05	4.32E-05	7.10E-05	9.89E-05
	0.190	0.547	0.783	0.874	0.860	0.855	0.762	0.615
$C^{17}O(2-1)$, $R_{\text{out}} = 700 \text{ au}$, $M_{\text{disc}} = 1 M_{\odot}$, $p = -2.0$.								
minimum χ_w^2 2.24952173								
B8	8.58E-05	7.51E-05	4.15E-05	1.31E-05	3.34E-06	0.00E+00	2.38E-06	9.54E-07
	0.063	0.159	0.332	0.459	0.450	0.449	0.431	0.517
B5	8.46E-05	6.32E-05	2.50E-05	2.41E-05	2.86E-05	2.53E-05	2.34E-05	3.62E-05
	0.122	0.429	0.820	0.869	0.938	0.977	0.977	0.938
B3	8.27E-05	4.77E-05	2.31E-05	2.46E-05	3.43E-05	3.96E-05	3.62E-05	3.36E-05
	0.175	0.532	0.791	0.879	0.842	0.858	0.845	0.860
B2	8.11E-05	3.58E-05	2.53E-05	2.55E-05	3.84E-05	4.77E-05	5.10E-05	4.98E-05
	0.195	0.663	0.820	0.935	0.859	0.820	0.786	0.937
B1	7.82E-05	3.39E-05	3.39E-05	3.86E-05	4.29E-05	6.32E-05	7.49E-05	6.70E-05
	0.254	0.742	0.782	0.898	0.869	0.704	0.547	0.777

C ¹⁷ O(2-1), $R_{\text{out}} = 1100 \text{ au}$, $M_{\text{disc}} = 1 M_{\odot}$, $p = -2.0$.								
minimum χ_w^2 2.24948359								
B8	1.24E-04	1.16E-04	7.06E-05	2.60E-05	5.25E-06	4.77E-07	3.58E-06	1.34E-05
	0.098	0.254	0.694	1.006	1.142	1.142	1.155	1.084
B5	1.22E-04	9.51E-05	3.17E-05	9.30E-06	3.42E-14	1.55E-05	2.00E-05	3.24E-05
	0.132	0.410	0.790	0.958	1.074	0.962	0.938	0.946
B3	1.20E-04	7.41E-05	1.62E-05	4.05E-06	2.10E-05	3.53E-05	4.08E-05	4.01E-05
	0.156	0.547	0.889	1.055	0.977	0.947	0.949	0.917
B2	1.17E-04	5.46E-05	1.14E-05	9.54E-06	3.12E-05	4.74E-05	5.60E-05	6.70E-05
	0.200	0.721	1.016	1.167	1.055	1.055	1.013	0.938
B1	1.15E-04	4.03E-05	2.19E-05	3.24E-05	4.32E-05	6.48E-05	8.58E-05	7.65E-05
	0.273	0.859	1.104	1.094	1.060	0.977	0.859	0.864
C ¹⁷ O(2-1), $R_{\text{out}} = 1500 \text{ au}$, $M_{\text{disc}} = 1 M_{\odot}$, $p = -2.0$.								
minimum χ_w^2 2.24940968								
B8	1.96E-04	1.82E-04	1.34E-04	6.94E-05	2.15E-05	0.00E+00	5.48E-06	8.58E-06
	0.049	0.107	0.225	0.314	0.356	0.361	0.342	0.390
B5	1.96E-04	1.65E-04	9.16E-05	5.05E-05	2.03E-05	3.67E-05	4.63E-05	7.03E-05
	0.156	0.439	0.850	1.074	1.240	1.216	1.152	1.016
B3	1.93E-04	1.41E-04	7.03E-05	2.62E-05	3.84E-05	6.06E-05	7.27E-05	8.63E-05
	0.171	0.552	0.977	1.206	1.249	1.113	1.074	0.977
B2	1.90E-04	1.21E-04	5.67E-05	3.62E-05	5.63E-05	8.63E-05	1.04E-04	1.06E-04
	0.195	0.742	1.113	1.284	1.201	1.133	1.017	0.997
B1	1.87E-04	9.54E-05	4.22E-05	5.29E-05	7.77E-05	1.11E-04	1.34E-04	1.22E-04
	0.239	0.879	1.307	1.348	1.304	1.152	1.021	1.084
C ¹⁷ O(2-1), $R_{\text{in}} = 100 \text{ au}$, $R_{\text{out}} = 1500 \text{ au}$, $M_{\text{disc}} = 1 M_{\odot}$, $p = -1.0$.								
minimum χ_w^2 2.24935746								
B8	2.51E-04	2.42E-04	2.01E-04	1.41E-04	9.87E-05	8.68E-05	9.75E-05	1.13E-04
	0.063	0.166	0.381	0.588	0.684	0.699	0.657	0.645
B5	2.50E-04	2.24E-04	1.43E-04	6.51E-05	1.86E-05	1.79E-05	4.91E-05	8.20E-05
	0.059	0.193	0.381	0.526	0.591	0.567	0.527	0.486
B3	2.48E-04	2.04E-04	1.02E-04	2.38E-05	4.05E-06	3.19E-05	7.39E-05	1.07E-04
	0.063	0.244	0.450	0.596	0.634	0.581	0.490	0.435
B2	2.46E-04	1.75E-04	5.65E-05	0.00E+00	2.65E-05	7.39E-05	1.10E-04	1.34E-04
	0.088	0.327	0.566	0.698	0.662	0.586	0.498	0.439
B1	2.41E-04	1.31E-04	1.07E-05	1.96E-05	7.80E-05	1.08E-04	1.33E-04	1.50E-04
	0.137	0.471	0.762	0.791	0.703	0.626	0.527	0.489
C ¹⁷ O(2-1), $R_{\text{in}} = 300 \text{ au}$, $R_{\text{out}} = 1500 \text{ au}$, $M_{\text{disc}} = 1 M_{\odot}$, $p = -1.0$.								
minimum χ_w^2 2.24936152								
B8	2.47E-04	2.38E-04	2.03E-04	1.40E-04	9.92E-05	9.23E-05	1.07E-04	1.18E-04
	0.073	0.176	0.361	0.605	0.701	0.665	0.643	0.654
B5	2.46E-04	2.24E-04	1.45E-04	6.65E-05	1.74E-05	1.38E-05	4.46E-05	7.75E-05
	0.054	0.173	0.353	0.489	0.569	0.557	0.500	0.464
B3	2.46E-04	2.06E-04	1.05E-04	2.62E-05	3.42E-14	2.26E-05	6.56E-05	1.01E-04
	0.059	0.200	0.410	0.537	0.588	0.544	0.474	0.429
B2	2.43E-04	1.78E-04	6.25E-05	2.38E-06	2.07E-05	6.41E-05	1.00E-04	1.27E-04
	0.083	0.293	0.518	0.645	0.620	0.542	0.474	0.410
B1	2.40E-04	1.35E-04	1.91E-05	1.60E-05	7.06E-05	9.63E-05	1.19E-04	1.41E-04
	0.117	0.420	0.654	0.701	0.635	0.584	0.510	0.468

$C^{17}O(2-1)$, $R_{in} = 500$ au, $R_{out} = 1500$ au, $M_{disc} = 1 M_{\odot}$, $p = -1.0$.
minimum χ_w^2 2.24937868

B8	2.30E-04	2.23E-04	1.92E-04	1.34E-04	8.58E-05	7.06E-05	8.42E-05	9.75E-05
	0.069	0.173	0.361	0.586	0.703	0.703	0.635	0.654
B5	2.30E-04	2.11E-04	1.44E-04	6.20E-05	1.17E-05	8.82E-06	3.93E-05	7.27E-05
	0.049	0.151	0.322	0.470	0.528	0.537	0.454	0.439
B3	2.29E-04	1.96E-04	1.04E-04	2.34E-05	3.86E-14	2.00E-05	5.60E-05	9.68E-05
	0.056	0.176	0.372	0.503	0.544	0.508	0.430	0.391
B2	2.27E-04	1.73E-04	6.15E-05	5.96E-06	2.19E-05	5.51E-05	8.80E-05	1.15E-04
	0.068	0.239	0.444	0.544	0.527	0.479	0.425	0.367
B1	2.24E-04	1.37E-04	2.31E-05	2.48E-05	6.60E-05	8.77E-05	1.07E-04	1.27E-04
	0.097	0.332	0.556	0.596	0.557	0.503	0.435	0.388

$C^{34}S(2-1)$, $R_{out} = 1500$ au, $M_{disc} = 1 M_{\odot}$, $p = -0.5$.
minimum χ_w^2 6.60866547

A5	8.25E-05	7.87E-05	8.25E-05	7.77E-05	7.06E-05	6.34E-05	5.77E-05	5.20E-05
	0.190	0.254	0.273	0.293	0.381	0.356	0.410	0.537
A0	8.11E-05	8.11E-05	7.96E-05	6.91E-05	5.77E-05	4.86E-05	4.29E-05	3.86E-05
	0.146	0.195	0.220	0.283	0.332	0.351	0.356	0.464
B8	8.01E-05	8.25E-05	7.82E-05	6.10E-05	4.53E-05	3.77E-05	3.39E-05	3.15E-05
	0.122	0.142	0.176	0.254	0.293	0.313	0.315	0.361
B5	7.96E-05	8.39E-05	6.39E-05	4.05E-05	3.05E-05	2.34E-05	1.67E-05	1.38E-05
	0.112	0.137	0.215	0.293	0.321	0.322	0.356	0.391
B3	8.01E-05	8.15E-05	5.15E-05	3.24E-05	2.24E-05	1.05E-05	6.68E-06	4.29E-06
	0.122	0.137	0.271	0.342	0.352	0.413	0.410	0.439
B2	8.15E-05	7.63E-05	4.10E-05	2.57E-05	7.15E-06	3.34E-06	3.34E-06	2.86E-06
	0.120	0.195	0.332	0.426	0.470	0.513	0.508	0.532
B1	8.30E-05	6.29E-05	3.19E-05	1.19E-05	1.43E-06	6.22E-15	6.22E-15	4.29E-06
	0.155	0.293	0.444	0.566	0.610	0.663	0.659	0.686

$C^{34}S(2-1)$, $R_{\text{out}} = 1500 \text{ au}$, $M_{\text{disc}} = 1 M_{\odot}$, $p = -1.0$.								
minimum χ_w^2 6.60866213								
A5	8.54E-05	8.15E-05	8.44E-05	7.96E-05	7.34E-05	6.72E-05	5.87E-05	5.39E-05
	0.190	0.236	0.254	0.331	0.371	0.391	0.466	0.508
A0	8.34E-05	8.30E-05	8.49E-05	7.10E-05	5.82E-05	4.82E-05	4.34E-05	3.72E-05
	0.161	0.198	0.234	0.298	0.352	0.389	0.410	0.474
B8	8.30E-05	8.49E-05	7.96E-05	5.96E-05	4.48E-05	3.67E-05	3.34E-05	3.00E-05
	0.137	0.142	0.195	0.274	0.322	0.352	0.361	0.420
B5	8.11E-05	8.34E-05	6.10E-05	3.72E-05	2.67E-05	2.10E-05	1.53E-05	1.29E-05
	0.137	0.146	0.244	0.320	0.389	0.391	0.430	0.430
B3	8.15E-05	7.87E-05	4.86E-05	2.77E-05	1.86E-05	1.86E-05	3.81E-06	4.77E-06
	0.127	0.175	0.312	0.392	0.448	0.469	0.474	0.504
B2	8.30E-05	7.25E-05	3.53E-05	2.00E-05	4.77E-06	3.34E-06	2.86E-06	1.91E-06
	0.138	0.244	0.410	0.503	0.554	0.552	0.605	0.585
B1	8.34E-05	5.87E-05	2.62E-05	6.68E-06	3.34E-06	1.33E-14	5.25E-06	9.54E-06
	0.176	0.389	0.581	0.698	0.703	0.723	0.703	0.742
$C^{34}S(2-1)$, $R_{\text{out}} = 1500 \text{ au}$, $M_{\text{disc}} = 1 M_{\odot}$, $p = -1.5$.								
minimum χ_w^2 6.60865974								
A5	8.82E-05	8.39E-05	1.06E-04	8.20E-05	7.25E-05	6.53E-05	5.77E-05	5.29E-05
	0.205	0.293	0.313	0.381	0.429	0.479	0.469	0.664
A0	8.58E-05	8.39E-05	8.34E-05	7.15E-05	5.63E-05	4.72E-05	4.10E-05	3.43E-05
	0.176	0.229	0.254	0.371	0.449	0.508	0.508	0.596
B8	8.34E-05	8.63E-05	7.72E-05	5.72E-05	4.29E-05	3.48E-05	2.91E-05	2.57E-05
	0.146	0.176	0.264	0.352	0.449	0.430	0.483	0.527
B5	1.06E-04	8.15E-05	5.63E-05	3.19E-05	2.19E-05	1.53E-05	1.10E-05	1.10E-05
	0.156	0.210	0.342	0.449	0.508	0.537	0.566	0.586
B3	8.20E-05	7.63E-05	4.29E-05	2.15E-05	1.34E-05	5.25E-06	4.44E-15	3.81E-06
	0.157	0.235	0.410	0.528	0.586	0.615	0.645	0.703
B2	8.15E-05	6.68E-05	2.81E-05	1.34E-05	9.54E-07	2.86E-06	3.81E-06	9.54E-06
	0.198	0.317	0.535	0.634	0.781	0.742	0.779	0.781
B1	8.15E-05	5.29E-05	1.76E-05	2.38E-06	2.86E-06	6.68E-06	1.05E-05	1.72E-05
	0.259	0.508	0.742	0.821	0.879	0.898	0.977	0.937
$C^{34}S(2-1)$, $R_{\text{out}} = 1500 \text{ au}$, $M_{\text{disc}} = 1 M_{\odot}$, $p = -2.0$.								
minimum χ_w^2 6.60865736								
A5	9.01E-05	8.58E-05	8.73E-05	8.01E-05	6.96E-05	5.87E-05	5.01E-05	4.63E-05
	0.244	0.371	0.405	0.522	0.615	0.664	0.704	0.859
A0	8.73E-05	8.58E-05	8.15E-05	6.58E-05	4.96E-05	3.91E-05	4.05E-05	2.81E-05
	0.283	0.332	0.469	0.642	0.830	0.840	0.938	1.011
B8	8.58E-05	8.49E-05	7.30E-05	5.15E-05	3.39E-05	2.53E-05	2.24E-05	1.86E-05
	0.273	0.347	0.547	0.703	0.933	0.898	0.977	1.025
B5	8.25E-05	7.68E-05	4.86E-05	2.57E-05	1.57E-05	1.19E-05	9.54E-06	9.06E-06
	0.249	0.410	0.645	0.850	0.996	1.001	1.130	1.167
B3	8.15E-05	7.01E-05	3.72E-05	1.57E-05	1.14E-05	3.81E-06	1.43E-06	1.00E-05
	0.310	0.488	0.840	1.093	1.035	1.113	1.249	1.230
B2	7.96E-05	6.10E-05	2.29E-05	9.54E-06	0.00E+00	7.63E-06	1.10E-05	1.72E-05
	0.352	0.605	0.977	1.132	1.284	1.299	1.387	1.289
B1	7.72E-05	4.43E-05	1.34E-05	3.34E-06	9.54E-06	1.81E-05	2.77E-05	3.77E-05
	0.428	0.819	1.167	1.503	1.329	1.328	1.494	1.326

$C^{34}S(2-1)$, $R_{\text{out}} = 1500$ au, $M_{\text{disc}} = 0.1 M_{\odot}$, $p = -1.0$.								
minimum χ_w^2 6.60866451								
A5	8.49E-05	7.96E-05	8.34E-05	7.96E-05	6.96E-05	5.87E-05	5.25E-05	4.82E-05
	0.430	0.586	0.626	0.703	0.957	1.099	1.318	1.367
A0	8.25E-05	8.30E-05	8.11E-05	6.77E-05	5.48E-05	4.34E-05	3.67E-05	3.39E-05
	0.508	0.586	0.781	0.942	1.133	1.367	1.543	1.621
B8	8.15E-05	8.39E-05	7.77E-05	5.72E-05	4.05E-05	3.05E-05	2.77E-05	2.72E-05
	0.547	0.645	0.859	1.260	1.494	1.797	1.758	1.724
B5	7.96E-05	8.25E-05	5.91E-05	3.58E-05	2.62E-05	2.10E-05	1.19E-05	9.54E-06
	0.664	0.918	1.450	1.953	2.256	2.305	2.539	2.510
B3	7.92E-05	7.96E-05	4.77E-05	2.81E-05	1.86E-05	6.20E-06	9.54E-07	3.81E-06
	0.840	1.016	1.873	2.498	2.578	3.030	3.193	2.974
B2	8.39E-05	7.20E-05	3.62E-05	2.19E-05	4.77E-06	1.43E-06	1.91E-06	3.81E-06
	0.938	1.504	2.480	2.891	3.652	3.672	3.809	3.594
B1	8.20E-05	5.87E-05	2.86E-05	8.58E-06	9.54E-07	2.31E-14	9.54E-07	5.72E-06
	1.172	1.953	3.281	3.828	4.395	4.412	4.453	4.414
$C^{34}S(2-1)$, $R_{\text{out}} = 700$ au, $M_{\text{disc}} = 1 M_{\odot}$, $p = -1.0$.								
minimum χ_w^2 6.60865974								
B8	8.54E-05	7.87E-05	5.44E-05	3.67E-05	2.43E-05	1.00E-05	7.63E-06	5.72E-06
	0.273	0.410	0.630	0.801	0.859	0.936	0.957	1.055
B5	8.73E-05	6.53E-05	3.81E-05	1.48E-05	4.77E-06	1.91E-06	7.15E-06	8.11E-06
	0.234	0.396	0.615	0.766	0.850	0.784	0.825	0.919
B3	8.39E-05	5.63E-05	2.48E-05	3.81E-06	2.86E-06	2.86E-06	1.19E-05	1.48E-05
	0.205	0.468	0.665	0.840	0.859	0.898	0.859	0.861
B2	8.25E-05	4.77E-05	1.43E-05	4.44E-15	2.86E-06	9.06E-06	3.00E-05	3.58E-05
	0.244	0.537	0.779	0.933	1.015	0.967	0.864	0.862
B1	7.77E-05	3.39E-05	4.77E-07	6.20E-06	1.48E-05	3.24E-05	4.77E-05	5.15E-05
	0.332	0.723	1.074	1.133	1.134	1.245	1.133	1.055
$C^{34}S(2-1)$, $R_{\text{out}} = 900$ au, $M_{\text{disc}} = 1 M_{\odot}$, $p = -1.0$.								
minimum χ_w^2 6.60865784								
B8	8.68E-05	8.49E-05	6.48E-05	4.39E-05	3.34E-05	2.15E-05	1.43E-05	1.05E-05
	0.215	0.303	0.430	0.547	0.623	0.698	0.703	0.801
B5	8.73E-05	7.63E-05	4.67E-05	2.72E-05	1.05E-05	2.86E-06	2.86E-06	4.77E-06
	0.176	0.293	0.449	0.566	0.640	0.626	0.703	0.728
B3	8.68E-05	6.58E-05	3.43E-05	1.00E-05	1.43E-06	1.91E-06	4.77E-06	6.68E-06
	0.186	0.342	0.513	0.664	0.669	0.728	0.723	0.740
B2	8.73E-05	5.67E-05	2.53E-05	9.54E-07	3.73E-14	2.38E-06	1.24E-05	2.48E-05
	0.195	0.400	0.620	0.753	0.789	0.801	0.859	0.781
B1	8.44E-05	4.39E-05	5.25E-06	2.38E-06	3.81E-06	1.62E-05	3.05E-05	4.01E-05
	0.236	0.566	0.859	1.006	1.054	1.016	0.956	0.938

$C^{34}S(2-1)$, $R_{\text{out}} = 1100$ au, $M_{\text{disc}} = 1 M_{\odot}$, $p = -1.0$.								
minimum χ_w^2 6.60865736								
B8	8.73E-05	8.82E-05	7.30E-05	5.20E-05	4.01E-05	3.00E-05	2.38E-05	1.91E-05
	0.166	0.215	0.352	0.449	0.527	0.508	0.510	0.620
B5	8.68E-05	8.15E-05	5.25E-05	3.29E-05	1.86E-05	8.11E-06	4.77E-06	5.72E-06
	0.151	0.200	0.334	0.439	0.523	0.537	0.568	0.605
B3	8.73E-05	7.39E-05	4.05E-05	2.19E-05	4.29E-06	2.38E-06	3.34E-06	5.25E-06
	0.151	0.239	0.392	0.488	0.605	0.586	0.703	0.663
B2	8.73E-05	6.44E-05	3.10E-05	5.25E-06	9.54E-07	4.77E-07	8.11E-06	9.54E-06
	0.186	0.323	0.517	0.645	0.742	0.743	0.753	0.752
B1	8.73E-05	4.96E-05	1.72E-05	0.00E+00	2.38E-06	7.63E-06	1.76E-05	2.48E-05
	0.215	0.488	0.703	0.820	0.820	0.928	0.854	0.820
$C^{34}S(2-1)$, $R_{\text{out}} = 1100$ au, $M_{\text{disc}} = 1 M_{\odot}$, $p = -1.0$.								
minimum χ_w^2 6.60866547								
B8	7.92E-05	8.20E-05	7.77E-05	6.20E-05	4.63E-05	3.77E-05	3.19E-05	3.10E-05
	0.135	0.137	0.176	0.244	0.274	0.311	0.321	0.354
B5	7.87E-05	8.20E-05	6.44E-05	4.10E-05	2.77E-05	2.38E-05	1.91E-05	1.62E-05
	0.122	0.117	0.225	0.293	0.334	0.344	0.344	0.381
B3	7.87E-05	7.96E-05	5.25E-05	2.86E-05	2.19E-05	1.19E-05	9.54E-06	1.00E-05
	0.127	0.151	0.273	0.371	0.393	0.402	0.420	0.430
B2	7.96E-05	7.44E-05	4.01E-05	2.48E-05	1.19E-05	6.20E-06	4.77E-06	5.72E-06
	0.147	0.205	0.371	0.449	0.488	0.508	0.527	0.517
B1	8.11E-05	6.25E-05	2.67E-05	1.29E-05	9.54E-07	6.22E-15	2.38E-06	4.29E-06
	0.186	0.303	0.470	0.576	0.667	0.663	0.664	0.703
$C^{34}S(2-1)$, $R_{\text{out}} = 700$ au, $M_{\text{disc}} = 1 M_{\odot}$, $p = -2.0$.								
minimum χ_w^2 6.60866594								
B8	7.82E-05	6.96E-05	4.53E-05	2.77E-05	1.57E-05	3.81E-06	1.43E-06	1.43E-06
	0.186	0.322	0.469	0.623	0.620	0.626	0.664	0.781
B5	7.58E-05	5.34E-05	2.77E-05	1.05E-05	3.34E-06	3.34E-06	1.57E-05	2.24E-05
	0.459	0.820	1.172	1.484	1.718	1.727	1.641	1.719
B3	7.39E-05	4.10E-05	1.72E-05	5.72E-06	4.29E-06	1.19E-05	2.81E-05	3.00E-05
	0.464	0.947	1.289	1.563	1.641	1.720	1.641	1.602
B2	6.91E-05	3.48E-05	9.06E-06	1.43E-06	9.06E-06	2.81E-05	4.34E-05	5.34E-05
	0.547	1.089	1.559	1.680	1.724	1.875	1.543	1.396
B1	6.29E-05	2.57E-05	4.80E-14	1.57E-05	2.43E-05	4.67E-05	7.30E-05	7.49E-05
	0.703	1.367	1.733	1.841	1.914	1.836	1.406	1.111

$C^{34}S(2-1)$, $R_{\text{out}} = 1100 \text{ au}$, $M_{\text{disc}} = 1 M_{\odot}$, $p = -2.0$.
minimum χ_w^2 6.60865831

B8	8.49E-05	8.30E-05	6.15E-05	4.01E-05	2.81E-05	1.72E-05	1.19E-05	8.11E-06
	0.312	0.464	0.732	0.869	1.074	1.113	1.248	1.251
B5	8.30E-05	7.01E-05	4.01E-05	2.15E-05	1.14E-05	3.34E-06	5.72E-06	9.54E-06
	0.332	0.537	0.861	0.938	1.162	1.288	1.377	1.289
B3	8.11E-05	5.87E-05	2.91E-05	9.54E-06	2.38E-06	2.86E-06	1.19E-05	1.19E-05
	0.333	0.627	0.939	1.248	1.251	1.367	1.329	1.440
B2	7.87E-05	5.25E-05	2.05E-05	0.00E+00	2.38E-06	7.63E-06	2.43E-05	2.72E-05
	0.410	0.850	1.172	1.484	1.407	1.641	1.483	1.483
B1	7.49E-05	3.62E-05	1.14E-05	4.29E-06	1.34E-05	2.62E-05	5.25E-05	5.96E-05
	0.488	1.006	1.377	1.578	1.567	1.757	1.406	1.389

$CS(1-0)$, $R_{\text{out}} = 1500 \text{ au}$, $M_{\text{disc}} = 1 M_{\odot}$, $p = -0.5$.
minimum χ_w^2 12.86234665

A5	4.10E-05	4.10E-05	4.10E-05	4.10E-05	4.10E-05	4.10E-05	4.01E-05	4.10E-05
	0.000	0.000	0.000	0.000	0.001	0.020	0.034	0.156
A0	4.10E-05	4.10E-05	4.10E-05	4.10E-05	3.91E-05	4.10E-05	4.10E-05	4.10E-05
	0.000	0.000	0.000	0.010	0.018	0.078	0.078	0.156
B8	4.10E-05	4.10E-05	4.10E-05	4.01E-05	4.10E-05	3.62E-05	4.10E-05	3.15E-05
	0.000	0.000	0.000	0.015	0.078	0.151	0.156	0.310
B5	4.10E-05	4.10E-05	4.10E-05	4.10E-05	3.53E-05	3.05E-05	2.19E-05	2.38E-05
	0.000	0.001	0.010	0.078	0.122	0.234	0.306	0.236
B3	4.10E-05	4.10E-05	4.10E-05	3.72E-05	3.43E-05	2.19E-05	1.53E-05	3.81E-06
	0.000	0.000	0.010	0.073	0.273	0.198	0.164	0.396
B2	4.10E-05	4.10E-05	3.81E-05	3.43E-05	2.57E-05	1.14E-05	8.58E-06	1.91E-06
	0.000	0.000	0.074	0.107	0.234	0.216	0.195	0.310
B1	4.10E-05	4.01E-05	3.81E-05	2.77E-05	4.10E-05	7.82E-14	1.91E-06	1.91E-06
	0.000	0.005	0.059	0.231	0.313	0.239	0.390	0.388

$CS(1-0)$, $R_{\text{out}} = 1500 \text{ au}$, $M_{\text{disc}} = 1 M_{\odot}$, $p = -1.0$.
minimum χ_w^2 12.86234283

A5	4.48E-05	4.48E-05	4.48E-05	4.48E-05	4.48E-05	4.48E-05	4.48E-05	4.48E-05
	0.000	0.000	0.002	0.000	0.001	0.010	0.020	0.156
A0	4.48E-05	4.48E-05	4.48E-05	4.48E-05	4.48E-05	4.48E-05	4.01E-05	3.81E-05
	0.001	0.000	0.001	0.020	0.020	0.005	0.311	0.266
B8	4.48E-05	4.48E-05	4.48E-05	4.39E-05	4.10E-05	3.72E-05	3.62E-05	3.24E-05
	0.000	0.000	0.000	0.017	0.306	0.230	0.232	0.317
B5	4.48E-05	4.48E-05	4.48E-05	4.29E-05	3.72E-05	2.86E-05	2.67E-05	2.48E-05
	0.000	0.001	0.010	0.122	0.176	0.157	0.157	0.430
B3	4.48E-05	4.48E-05	4.39E-05	3.81E-05	2.67E-05	2.57E-05	1.72E-05	1.91E-06
	0.000	0.000	0.010	0.118	0.272	0.176	0.312	0.438
B2	4.48E-05	4.48E-05	4.01E-05	3.43E-05	2.48E-05	4.48E-05	5.72E-06	1.91E-06
	0.001	0.005	0.076	0.233	0.234	0.313	0.352	0.313
B1	4.48E-05	4.39E-05	4.39E-05	2.48E-05	3.45E-13	5.72E-06	2.86E-06	3.45E-13
	0.000	0.009	0.059	0.164	0.313	0.344	0.390	0.313

CS(1-0), $R_{\text{out}} = 1500 \text{ au}$, $M_{\text{disc}} = 1 M_{\odot}$, $p = -1.5$.								
minimum χ_w^2 12.86233425								
A5	5.34E-05	5.34E-05	5.34E-05	5.34E-05	5.34E-05	5.34E-05	5.34E-05	5.34E-05
	0.000	0.000	0.002	0.010	0.001	0.020	0.010	0.000
A0	5.34E-05	5.34E-05	5.34E-05	5.34E-05	5.34E-05	5.34E-05	4.77E-05	4.86E-05
	0.000	0.000	0.001	0.010	0.020	0.020	0.254	0.391
B8	5.34E-05	5.34E-05	5.34E-05	5.05E-05	5.34E-05	4.77E-05	4.48E-05	4.20E-05
	0.000	0.000	0.000	0.020	0.156	0.195	0.254	0.386
B5	5.34E-05	5.34E-05	5.25E-05	5.05E-05	4.39E-05	4.01E-05	4.20E-05	2.57E-05
	0.000	0.000	0.009	0.127	0.225	0.195	0.430	0.542
B3	5.34E-05	5.34E-05	5.34E-05	4.29E-05	3.72E-05	2.96E-05	1.62E-05	6.68E-06
	0.000	0.005	0.010	0.214	0.303	0.264	0.392	0.471
B2	5.34E-05	5.15E-05	5.05E-05	3.72E-05	2.77E-05	9.54E-06	9.54E-06	2.86E-06
	0.000	0.009	0.117	0.161	0.322	0.468	0.430	0.313
B1	5.34E-05	5.15E-05	4.39E-05	3.15E-05	1.91E-06	7.63E-06	1.43E-05	1.92E-13
	0.000	0.009	0.156	0.464	0.417	0.459	0.391	0.381
CS(1-0), $R_{\text{out}} = 1500 \text{ au}$, $M_{\text{disc}} = 1 M_{\odot}$, $p = -2.0$.								
minimum χ_w^2 12.86233902								
A5	4.86E-05	4.86E-05	4.86E-05	4.86E-05	4.86E-05	4.86E-05	4.86E-05	4.67E-05
	0.000	0.000	0.005	0.001	0.001	0.039	0.039	0.312
A0	4.86E-05	4.86E-05	4.86E-05	4.77E-05	4.58E-05	4.58E-05	4.86E-05	4.10E-05
	0.000	0.000	0.001	0.037	0.035	0.293	0.313	0.620
B8	4.86E-05	4.86E-05	4.86E-05	4.77E-05	4.48E-05	3.81E-05	3.72E-05	3.34E-05
	0.000	0.000	0.010	0.029	0.273	0.371	0.332	0.386
B5	4.86E-05	4.86E-05	4.77E-05	4.01E-05	3.72E-05	2.96E-05	2.38E-05	8.58E-06
	0.000	0.000	0.017	0.303	0.273	0.332	0.315	0.781
B3	4.86E-05	4.86E-05	4.67E-05	3.72E-05	2.96E-05	2.29E-05	1.24E-05	2.86E-06
	0.000	0.010	0.156	0.293	0.315	0.605	0.703	0.703
B2	4.86E-05	4.86E-05	3.81E-05	3.34E-05	1.43E-05	6.68E-06	2.86E-06	0.00E+00
	0.000	0.010	0.283	0.352	0.737	0.674	0.703	0.859
B1	4.86E-05	4.86E-05	3.05E-05	1.72E-05	9.54E-07	6.68E-06	2.86E-06	2.86E-06
	0.000	0.020	0.317	0.703	0.629	0.669	0.629	0.663

Acknowledgements

First and foremost I would like to express my thanks to Dr. Katharina Schreyer, who as advisor of my PhD thesis suggested the topic and provided support and helpful scientific discussions anytime; last but not least I am indebted to her for her patience and encouragement. Furthermore I thank Dr. Yaroslav Pavlyuchenkov for making available to me the radiative transfer code URANI(A) and a code for creating the physical model of the disc. Prof. Dr. Peter Hofner I thank for an extensive introduction to the interferometry data reduction software AIPS.

I am also thankful to Prof. Dr. Ralph Neuhäuser and all colleagues at the Astrophysical Institute and University Observatory Jena for the interesting discussions, the insights into scientific areas apart from the focus of this PhD thesis, for the the opportunity to gain extensive experience in optical observations, and for providing a pleasant working atmosphere.

Finally, I thank my family and close friends for their encouragement and general support, and for sharing the fascination about nature also beyond astronomy.

Ehrenwörtliche Erklärung

Ich erkläre hiermit ehrenwörtlich, dass ich die vorliegende Arbeit selbständig, ohne unzulässige Hilfe Dritter und ohne Benutzung anderer als der angegebenen Hilfsmittel und Literatur angefertigt habe. Die aus anderen Quellen direkt oder indirekt übernommenen Daten und Konzepte sind unter Angabe der Quelle gekennzeichnet.

Weitere Personen waren an der inhaltlich-materiellen Erstellung der vorliegenden Arbeit nicht beteiligt. Insbesondere habe ich hierfür nicht die entgeltliche Hilfe von Vermittlungs- bzw. Beratungsdiensten (Promotionsberater oder andere Personen) in Anspruch genommen. Niemand hat von mir unmittelbar oder mittelbar geldwerte Leistungen für Arbeiten erhalten, die im Zusammenhang mit dem Inhalt der vorgelegten Dissertation stehen.

Die Arbeit wurde bisher weder im In- noch Ausland in gleicher oder ähnlicher Form einer anderen Prüfungsbehörde vorgelegt.

Die geltende Promotionsordnung der Physikalisch-Astronomischen Fakultät ist mir bekannt.

Ich versichere ehrenwörtlich, dass ich nach bestem Wissen die reine Wahrheit gesagt und nichts verschwiegen habe.

Jena, den 19.9.2014

Lebenslauf

Claudia Marka

geboren am 17.10.1984 in Karl-Marx-Stadt (jetzt Chemnitz)

1991–1995 Besuch der Grundschule Hirschfelde

1995–2003 Richard-von-Schlieben-Gymnasium Zittau

Juni 2003 Abitur

2003–2008 Physikstudium an der Friedrich-Schiller-Universität Jena

2007–2008 Diplomarbeit am Astrophysikalischen Institut Jena

Thema der Arbeit: *"Molekülhäufigkeiten als Entwicklungsindikatoren von Bok-Globulen und optische Beobachtungen von CB 230"*

Dezember 2008 Diplom Physik, Friedrich-Schiller-Universität Jena

seit Januar 2009 Doktorandin am Astrophysikalischen Institut Jena

Jan. 2009 – Aug. 2012 Wissenschaftlicher Mitarbeiter, Astrophysikalisches Institut Jena

Sep. 2012 – Dez. 2012 Wissenschaftlicher Mitarbeiter, Astrophysikalisches Institut Jena

Juni 2013 – Juli 2013 Wissenschaftlicher Mitarbeiter, Astrophysikalisches Institut Jena

seit September 2014 Wissenschaftlicher Mitarbeiter, Instituto de Radio Astronomía
Milimétrica Granada

Jena, September 2014